



NAVAL POSTGRADUATE SCHOOL

MONTEREY, CALIFORNIA

THESIS

**NEAR FIELD IMAGING OF CHARGE TRANSPORT IN
GALLIUM NITRIDE AND ZINC OXIDE
NANOSTRUCTURES**

by

Richard Adam Cole

December 2010

Thesis Advisor:
Second Reader:

Nancy M. Haegel
Peter P. Crooker

Approved for public release; distribution is unlimited

THIS PAGE INTENTIONALLY LEFT BLANK

REPORT DOCUMENTATION PAGE			<i>Form Approved OMB No. 0704-0188</i>	
Public reporting burden for this collection of information is estimated to average 1 hour per response, including the time for reviewing instruction, searching existing data sources, gathering and maintaining the data needed, and completing and reviewing the collection of information. Send comments regarding this burden estimate or any other aspect of this collection of information, including suggestions for reducing this burden, to Washington headquarters Services, Directorate for Information Operations and Reports, 1215 Jefferson Davis Highway, Suite 1204, Arlington, VA 22202-4302, and to the Office of Management and Budget, Paperwork Reduction Project (0704-0188) Washington DC 20503.				
1. AGENCY USE ONLY (Leave blank)		2. REPORT DATE December 2010	3. REPORT TYPE AND DATES COVERED Master's Thesis	
4. TITLE AND SUBTITLE Near Field Imaging of Charge Transport in Gallium Nitride and Zinc Oxide Nanostructures			5. FUNDING NUMBERS	
6. AUTHOR(S) Richard Adam Cole				
7. PERFORMING ORGANIZATION NAME(S) AND ADDRESS(ES) Naval Postgraduate School Monterey, CA 93943-5000			8. PERFORMING ORGANIZATION REPORT NUMBER	
9. SPONSORING /MONITORING AGENCY NAME(S) AND ADDRESS(ES) N/A			10. SPONSORING/MONITORING AGENCY REPORT NUMBER	
11. SUPPLEMENTARY NOTES The views expressed in this thesis are those of the author and do not reflect the official policy or position of the Department of Defense or the U.S. Government.				
12a. DISTRIBUTION / AVAILABILITY STATEMENT Approved for public release; distribution is unlimited			12b. DISTRIBUTION CODE	
13. ABSTRACT (maximum 200 words) <p>A novel technique for imaging minority carrier diffusion in semiconductor nanostructures has been applied to the characterization of GaN and ZnO nanowires and nanobelts. Near field scanning optical microscopy (NSOM) is performed within a scanning electron microscope (SEM) to image carrier recombination with a spatial resolution exceeding the diffraction limit. The electron beam provides a high resolution, highly controlled source of carrier generation at a point. Diffusion lengths can be extracted directly from the resulting distribution of the recombination luminescence.</p> <p>A Nanonics Multi View 2000 provides a unique open architecture to allow the electron beam to be incident on a fixed point on the nanowire with independent motion of a collecting fiber to map the luminescence distribution. Probe tips are cantilevered optical fiber tips with diameters from 100 to 500 nm. Simultaneous NSOM, AFM and SEM imaging provides topographic, optical emission, and carrier transport information.</p> <p>This characterization technique has been used to measure minority carrier diffusion lengths in GaN nanowires, ZnO nanowires, and ZnO nanobelts, with diffusion lengths extracted from carrier recombination profiles. Evidence of waveguiding in some nanowires and nanobelts was also observed. The first measure of ZnO nanowires using this technique resulted in a measured diffusion length of approximately 150 nm for nanowires grown by the hydrothermal method and approximately 640 nm for those grown by physical vapor deposition. Additional results comparing diffusion lengths in n-type, p-type and unintentionally doped GaN nanowires, ZnO nanowires, and ZnO nanobelts are presented. While measuring the diffusion lengths of these structures, it was also observed that diffusion length measurements were sometimes impacted by combined effects associated with surface topography and optical waveguiding and interference.</p>				
14. SUBJECT TERMS Transport Imaging, Minority Carrier Diffusion Length, GaN Nanowires, ZnO Nanobelts, ZnO Nanowires, Near Field Scanning Optical Microscopy, NSOM			15. NUMBER OF PAGES 111	
			16. PRICE CODE	
17. SECURITY CLASSIFICATION OF REPORT Unclassified	18. SECURITY CLASSIFICATION OF THIS PAGE Unclassified	19. SECURITY CLASSIFICATION OF ABSTRACT Unclassified	20. LIMITATION OF ABSTRACT UU	

THIS PAGE INTENTIONALLY LEFT BLANK

Approved for public release; distribution unlimited

**NEAR FIELD IMAGING OF CHARGE TRANSPORT IN GALLIUM NITRIDE
AND ZINC OXIDE NANOSTRUCTURES**

Richard Adam Cole
Lieutenant, United States Navy
B.S., University of Kansas, 2004

Submitted in partial fulfillment of the
requirements for the degree of

MASTER OF SCIENCE IN APPLIED PHYSICS

from the

**NAVAL POSTGRADUATE SCHOOL
December 2010**

Author: Richard A. Cole

Approved by: Nancy M. Haegel
Thesis Advisor

Peter P. Crooker
Second Reader

Andres Larraza
Chairman, Department of Physics

THIS PAGE INTENTIONALLY LEFT BLANK

ABSTRACT

A novel technique for imaging minority carrier diffusion in semiconductor nanostructures has been applied to the characterization of GaN and ZnO nanowires and nanobelts. Near field scanning optical microscopy (NSOM) is performed within a scanning electron microscope (SEM) to image carrier recombination with a spatial resolution exceeding the diffraction limit. The electron beam provides a high resolution, highly controlled source of carrier generation at a point. Diffusion lengths can be extracted directly from the resulting distribution of the recombination luminescence.

A Nanonics Multi View 2000 provides a unique open architecture to allow the electron beam to be incident on a fixed point on the nanowire with independent motion of a collecting fiber to map the luminescence distribution. Probe tips are cantilevered optical fiber tips with diameters from 100 to 500 nm. Simultaneous NSOM, AFM and SEM imaging provides topographic, optical emission, and carrier transport information.

This characterization technique has been used to measure minority carrier diffusion lengths in GaN nanowires, ZnO nanowires, and ZnO nanobelts, with diffusion lengths extracted from carrier recombination profiles. Evidence of waveguiding in some nanowires and nanobelts was also observed. The first measure of ZnO nanowires using this technique resulted in a measured diffusion length of approximately 150 nm for nanowires grown by the hydrothermal method and approximately 640 nm for those grown by physical vapor deposition. Additional results comparing diffusion lengths in n-type, p-type and unintentionally doped GaN nanowires, ZnO nanowires, and ZnO nanobelts are presented. While measuring the diffusion lengths of these structures, it was also observed that diffusion length measurements were sometimes impacted by combined effects associated with surface topography and optical waveguiding and interference.

THIS PAGE INTENTIONALLY LEFT BLANK

TABLE OF CONTENTS

I.	INTRODUCTION.....	1
A.	SCOPE OF THE THESIS.....	1
B.	BACKGROUND – THE IMPORTANCE OF SMALL SEMICONDUCTOR DEVICES	1
C.	DEFENSE RELEVANCE.....	3
D.	IMPORTANCE OF THE MINORITY CARRIER DIFFUSION LENGTH	4
E.	GALLIUM NITRIDE NANOWIRES AND ZINC OXIDE NANOSTRUCTURES.....	5
II.	MINORITY CARRIER DIFFUSION LENGTH	7
A.	SEMICONDUCTOR BASICS.....	7
B.	MINORITY CARRIER DIFFUSION.....	8
III.	IMAGING CHARGE TRANSPORT	11
A.	IMAGING CHARGE TRANSPORT VERSUS EBIC.....	11
B.	CATHODOLUMINESCENCE	12
C.	DIFFRACTION	17
D.	FAR FIELD IMAGING	17
E.	NEAR FIELD IMAGING WITH NEAR FIELD SCANNING OPTICAL MICROSCOPY.....	18
IV.	EXPERIMENTAL SETUP	23
A.	EQUIPMENT.....	23
1.	SEM.....	23
2.	NSOM/AFM	24
3.	Photon Detectors	29
B.	EXPERIMENTAL APPROACH	30
V.	NANOSTRUCTURE GROWTH PROCESSES.....	35
A.	HYDROTHERMAL	35
B.	MOLECULAR BEAM EPITAXY	37
C.	PHYSICAL VAPOR DEPOSITION.....	38
VI.	EXPERIMENTAL RESULTS.....	41
A.	CATHODOLUMINESCENCE	44
1.	GaN Nanowires	44
2.	ZnO Nanostructures	47
B.	NSOM IMAGING OF NANOWIRES.....	49
1.	GaN Nanowires	50
a.	<i>N-Type GaN Nanowires.....</i>	<i>50</i>
b.	<i>Unintentionally Doped N-Type GaN Nanowires</i>	<i>51</i>
c.	<i>P-Type GaN Nanowires</i>	<i>53</i>
2.	ZnO Nanowires	55

a.	<i>Hydrothermal ZnO Nanowires</i>	55
b.	<i>Physical Vapor Deposition ZnO Nanowires</i>	56
C.	NANOBELTS	58
D.	OTHER NANOSTRUCTURES	61
E.	SUMMARY OF RESULTS	65
VII.	CONCLUSIONS AND SUGGESTIONS FOR FURTHER RESEARCH.....	67
A.	CONCLUSIONS	67
B.	SUGGESTIONS FOR FURTHER RESEARCH.....	68
APPENDIX A.	NANONICS MULTIVIEW 2000 [30]	71
APPENDIX B.	SPCM-AQR-14 PHOTON DETECTOR [31]	75
APPENDIX C.	MP-983 PHOTON DETECTOR [32].....	85
	LIST OF REFERENCES.....	87
	INITIAL DISTRIBUTION LIST	91

LIST OF FIGURES

Figure 1.	Schematic of Effect of Physical Size on the Properties of Any Material (from [6])	2
Figure 2.	Energy Band Diagram of a Generic Semiconductor (from [18])	7
Figure 3.	EBIC Configuration for Measuring Minority Carrier Diffusion Length	12
Figure 4.	Normalized 300 K CL Spectrum of a ZnO Nanowire	13
Figure 5.	2D Image of intensity distribution due to diffusion in a GaAs heterostructure. Variations in intensity are indicated by false color imaging. The beam generates charge at a single spot in the center of the image. Size of image is 193 μm width by 87 μm height (from [21]).	14
Figure 6.	(a) Line scans through 2D intensity images showing effects of diffusion and drift (from [21]). (b) Semi-logarithmic plots of the tail region of (a) with linear regression (from [21]).	16
Figure 7.	Schematic Illustration of Airy Patterns and Resolution (from [24])	18
Figure 8.	Light collected with NSOM from an unintentionally doped n-type GaN nanowire. The blue line represents the axis of the wire. The electron beam is incident at a point immediately before the blue line at the bottom of the figure.	19
Figure 9.	Intensity of light as a function of distance along the axis, the blue line, of the nanowire shown in Figure 8.	20
Figure 10.	Semi-logarithmic plot of the data in Figure 9	20
Figure 11.	Forces on an AFM Tip (from [25])	21
Figure 12.	Overview of Experimental Equipment	23
Figure 13.	Nanonics MultiView 2000	25
Figure 14.	SEM Chamber and Tower	25
Figure 15.	Nanonics MultiView 2000 Inside the SEM Chamber	26
Figure 16.	Optical Fiber Exiting SEM Chamber	26
Figure 17.	NSOM/AFM Probe Schematic (from [29])	27
Figure 18.	SEM Picture of NSOM/AFM Tip (from [28])	27
Figure 19.	Clockwise from Top Left Corner: Upper Stage HV Piezo Driver, Counter and Power Supply for the Photon Detector, Lower Stage HV Piezo Driver, and the SPM Controller	29
Figure 20.	SPCM-AQR-14 Photon Detector	30
Figure 21.	MP-983 Photon Detector	30
Figure 22.	Typical Tip, Beam, and Nanostructure (ZnO Nanobelt) Arrangement	31
Figure 23.	Hydrothermal Growth Process (from [33])	35
Figure 24.	HT Grown Nanowires (20,186X)	36
Figure 25.	Simplified MBE Process	37
Figure 26.	MBE Grown Nanowires (2,651X)	38
Figure 27.	Simplified PVD Process (from [38])	39
Figure 28.	PVD ZnO Nanowires (17,254X)	39
Figure 29.	PVD ZnO Nanobelt (17,254X)	40
Figure 30.	SEM Image (25,661X) of a Typical ZnO PVD Nanowire	42

Figure 31.	SEM image (1860X) of a typical PVD ZnO nanobelt. The long structure that spans from the lower left corner to the upper right corner is the nanobelt. Photo courtesy of Dr. Zhong Lin Wang of the Georgia Institute of Technology.	42
Figure 32.	SEM Image (15,817X) of a Nanostructure with Variable Surface Topography	43
Figure 33.	SEM Image (20,176X) of a Nanostructure with Variable Surface Topography	43
Figure 34.	CL Spectra of GaN Nanowires at 300 K	45
Figure 35.	Semi Logarithmic Plot (Y-Axis Scale is the Natural Logarithm of Intensity) of the Normalized CL Spectra of GaN Nanowires at 300 K	46
Figure 36.	CL Spectra of ZnO Nanostructures at 300 K.....	48
Figure 37.	Semi Logarithmic Plot (Y-Axis Scale is the Natural Logarithm of Intensity) of the Normalized CL Spectra of ZnO Nanostructures at 300 K	49
Figure 38.	NSOM Image of a 0.6 μm Diameter N-Type GaN Nanowire	50
Figure 39.	Combined AFM and NSOM of the GaN nanowire in Figure 38. Image has been rotated from Figure 38 for better viewing.....	50
Figure 40.	Semi Logarithmic Plot (Y-Axis Scale is the Natural Logarithm of Intensity) With Linear Best Fit of NSOM Intensity as a Function of Distance of a N-Type GaN Nanowire.....	51
Figure 41.	NSOM Image of a 0.5 μm Diameter GaN Unintentionally Doped N-Type Nanowire.....	51
Figure 42.	Combined AFM and NSOM of the GaN nanowire in Figure 41. Image has been rotated from Figure 41 for better viewing.....	52
Figure 43.	Semi Logarithmic Plot With Linear Best Fit of NSOM Intensity as a Function of Distance of an Unintentionally Doped N-Type GaN Nanowire ..	52
Figure 44.	NSOM Image of a 0.5 μm Diameter GaN P-Type Nanowire.....	53
Figure 45.	Combined AFM and NSOM of the GaN nanowire in Figure 44. Image has been rotated from Figure 44 for better viewing.....	54
Figure 46.	Semi Logarithmic Plot With Linear Best Fit of NSOM Intensity as a Function of Distance of a P-Type GaN Nanowire.....	54
Figure 47.	NSOM Image of a 0.6 μm Diameter ZnO HT Nanowire	55
Figure 48.	Combined AFM and NSOM of the HT ZnO nanowire in Figure 47. Image has been rotated from Figure 47 for better viewing.....	55
Figure 49.	Semi Logarithmic Plot With Linear Best Fit of NSOM Intensity as a Function of Distance of a HT ZnO Nanowire	56
Figure 50.	NSOM Image of a 0.8 μm Diameter ZnO PVD Nanowire.....	56
Figure 51.	Combined AFM and NSOM of the nanowire in Figure 50. Image has been rotated from Figure 50 for better viewing.....	57
Figure 52.	Semi Logarithmic Plot With Linear Best Fit of NSOM Intensity as a Function of Distance of a PVD ZnO Nanowire.....	57
Figure 53.	80 μm Diameter ZnO PVD Nanobelt and NSOM Tip	58
Figure 54.	NSOM of a 60 μm Wide ZnO PVD Nanobelt.....	59
Figure 55.	Combined AFM and NSOM of the Nanobelt in Figure 54	59

Figure 56.	Combined AFM and NSOM of a 60 μm Wide ZnO PVD nanobelt. The excitation point is at the center of the scan, so diffusion is seen in all directions.....	60
Figure 57.	Semi Logarithmic Plot With Linear Best Fit of NSOM Intensity as a Function of Distance of a PVD ZnO Nanobelt. This was used to establish the lower limit of the actual minority carrier diffusion length.....	60
Figure 58.	Example of “Leaking” and “Banding.” Clockwise from top left corner: NSOM Image of a nanostructure similar to the one shown in Figure 33 with an excitation current of 10^{-10} A, NSOM of the same structure at 3×10^{-10} A, plot of NSOM intensity as a function of distance at both 10^{-10} A and 3×10^{-10} A, and the combined NSOM and AFM of the nanostructure at 3×10^{-10} A.	62
Figure 59.	NSOM of a Structure that Exhibits Banding	63
Figure 60.	Standard CL Map of Light Bands in Other Nanostructure Samples	63
Figure 61.	Combined NSOM and AFM of a nanostructure “leaking,” transmitting light out of its side.	64
Figure 62.	2D and 3D plot of waveguided light. The 3D plot is CL intensity only, no topography data is present. Notice the distinct bands of light and the doughnut hole-like shape in the center.	64
Figure 63.	Transverse Electromagnetic Modes of Lasers (from [41])	69

THIS PAGE INTENTIONALLY LEFT BLANK

LIST OF TABLES

Table 1.	Beam Diameter as a Function of Probe Current at 30 keV (from [27])	24
Table 2.	Summary of measured NSOM minority carrier diffusion lengths. *Note that, as shown in this chapter, the measured diffusion lengths of ZnO Other Nanostructures are not the actual diffusion lengths.....	65
Table 3.	Summary of NSOM Minority Carrier Diffusion Lengths in MOVCD GaN Nanowires (from [28])	68

THIS PAGE INTENTIONALLY LEFT BLANK

LIST OF ACRONYMS AND ABBREVIATIONS

AFM	Atomic Force Microscopy
CCD	Charge-Coupled Device
CL	Cathodoluminescence
EBIC	Electron Beam Induced Current
GaN	Gallium Nitride
HT	Hydrothermal
LED	Light Emitting Diode
MBE	Molecular Beam Epitaxy
MOCVD	Metal-Organic Chemical Vapor Deposition
NSOM	Near Field Scanning Optical Microscopy
PVD	Physical Vapor Deposition
SEM	Scanning Electron Microscope
ZnO	Zinc Oxide

THIS PAGE INTENTIONALLY LEFT BLANK

ACKNOWLEDGMENTS

Most of all, I would like to thank my wife. Without her love and support I would not be where I am today. I would also like to thank Dr. Nancy Haegel. Without her mentorship, guidance, and patience I could not have completed this thesis. Dr. Peter Crooker also played a large role in this work: his constructive criticism made it more informative and easier to understand. I also need to thank Abby Hoffman, our MySem master, for the many SEM images she produced.

Dr. Zhong Lin Wang and Dr. Yaguang Wei of the Georgia Institute of Technology provided the ZnO nanostructures, and Dr. Kris Bertness of the National Institute of Standards and Technology (NIST) provided the GaN nanowires. Funding was provided by the Defense Advanced Research Projects Agency (DARPA) and the National Science Foundation DMR 0804527.

THIS PAGE INTENTIONALLY LEFT BLANK

I. INTRODUCTION

A. SCOPE OF THE THESIS

The primary objective of this thesis is to present the results of novel measurements of the minority carrier diffusion length in three types of semiconductor nanostructures: gallium nitride nanowires, zinc oxide nanowires, and zinc oxide nanobelts. This is accomplished via near field optical scanning to map the spatial distribution of recombination luminescence. While researching the diffusion lengths of these structures, the author also observed that many of these devices exhibited waveguiding, and that diffusion length measurements were sometimes impacted by the topographic features of the nanostructure. Thus, analysis of these behaviors are secondary objectives of this thesis.

B. BACKGROUND – THE IMPORTANCE OF SMALL SEMICONDUCTOR DEVICES

Semiconductor devices have enhanced the lives of people worldwide. Computers, televisions, telephones, the Internet, cellular phones, radios, solar cells, as well as many other applications and devices in their modern form would not exist without them. They form the foundation of the technology of modern society.

By decreasing the size of the components that comprise modern electronics, semiconductor materials have fueled the rapid advance of technology. In 1946, the first general-purpose computer in the United States was completed. Called ENIAC, Electronic Numerator Integrator Analyzer and Computer, it performed addition or subtraction calculations with 19000 large vacuum tubes, resulting in a computer that filled an entire room and weighed over 30 tons [1]. To reduce the size, power consumption, and heat of computers such as ENIAC, scientists began researching semiconductor materials in an effort to create a solid state device to replace vacuum tubes. The year following ENIAC's completion, researchers at Bell Labs created the first semiconductor transistor [2], and, since then, the size of the transistor has continually

decreased. Over the past forty years, transistor size has decreased at a rate that allows the number of transistors contained on any single computer chip to double every 24 months [3]. Today, the size of modern silicon based transistors is measured in the tens of nanometers with some modern processors containing billions of devices [4], allowing engineers to design computers that calculate trillions of floating point operations per second [5]. Intel estimates that its future processors will contain transistors with gate lengths of 10 nm or less [4].

Smaller, more powerful computers are not, however, the only benefit of continued research into semiconductor nanostructures. To understand why, consider Figure 1. As material dimensions approach the nanoscale, 100 nm or less, the characteristics of specific properties will differ with those of the bulk material [6]. For example, the thermal conductivity of bulk materials is higher than that of nanostructures [6]. The bandgap of a semiconductor also becomes size dependent below a certain threshold. The unique properties of nanoscale materials are of great interest to many scientists and engineers. A thorough understanding of these characteristics may allow them to develop technologies with enhanced performance and efficiency and allow use of nanostructures in completely new areas of application.

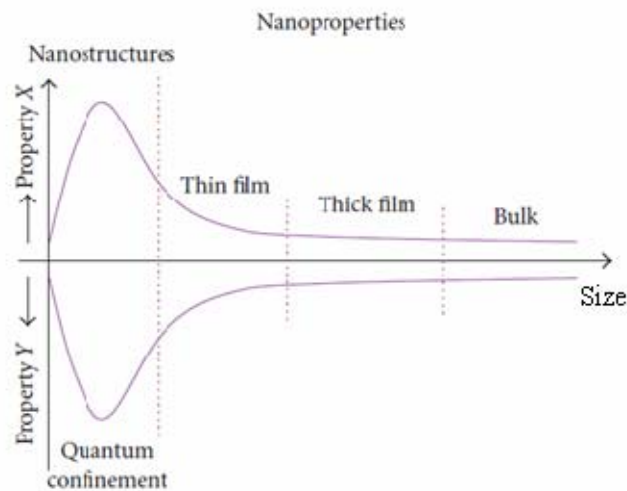


Figure 1. Schematic of Effect of Physical Size on the Properties of Any Material (from [6])

Solar power is one area where this enhanced performance and efficiency may be achieved. For example, researchers at Rensselaer Polytechnic Institute have developed an antireflective coating for solar panels from nanostructures. Using this coating in their experiments, they have reduced the amount of sunlight reflected off silicon solar cells from 32.6 percent to 3.79 percent at wavelengths from 400 nm to 1600 nm, thereby increasing the amount of sunlight collected and improving the overall efficiency of the system [7]. Although it is not yet clear if this technique can be translated into a commercial product, the implication of their work is clear: research into nanostructures may one day result in significantly more efficient solar cells capable of producing energy at the same cost as traditional methods.

Other applications of semiconductor nanostructures include more powerful and longer lasting lithium ion batteries [8], increased energy storage in capacitors [8], and nanoscale lasers [9]. Nanoscale lasers have the potential to produce highly localized and monochromatic, single wavelength light [10]. Since they can be easily coupled with other nanoscale structures, such as quantum dots or even small biological specimens, they will most likely become critical components of new nanophotonics [10]. Zinc oxide (ZnO) nanowires are particularly interesting, since they have been observed to transition to laser oscillation at room temperature [10]. As research into semiconductor nanostructures continues, the list of potential applications will continue to grow.

C. DEFENSE RELEVANCE

The defense organizations of the United States are continually striving for smaller, more efficient, and more capable defense technologies to enhance the effectiveness and survivability of American personnel and weapon systems. Consider, for instance, the modern soldier. Average soldiers carry over 140 pounds of equipment while on patrol or in combat [11]. Some of this weight consists of electronic systems and the batteries needed to power them [12]. Developing new technologies based on nanoscale structures that reduce this burden without sacrificing capability is critical to deploying more mobile, efficient, and effective soldiers.

Laser action in nanowires also has important defense applications that range from new battlefield medical technologies to information processing. Other potential defense applications of nanotechnology are seemingly endless. Smaller electronic and power systems not only benefit soldiers, but may also result in lighter, more capable warships, planes, and tanks that are cheaper to man, fuel, and maintain. Nanoscale sensors potentially offer improved response times, sensitivity, and, because of their small size, can be unobtrusively placed almost anywhere [12]. As research continues and knowledge of nanostructures increases, more useful defense applications of this new technology will undoubtedly arise.

Thus, systems based on nanostructures have the potential to reduce the size, weight, and cost of current military technologies while simultaneously increasing their performance, resulting in a more capable and mobile force. A fundamental understanding of nanostructures will also allow the development and deployment of a variety of new defense and homeland security applications that range from power generation to new weapon systems. Therefore, investment and continued research in this area is critical to America's current and future security.

D. IMPORTANCE OF THE MINORITY CARRIER DIFFUSION LENGTH

An understanding of a nanostructure's properties is required before scientists and engineers can begin developing new applications and technologies based upon it. For instance, the so called "minority carrier devices," such as light emitting diodes (LEDs) or bipolar transistors, depend upon the behavior of injected minority carriers, so an understanding of the minority carrier diffusion length is critical to their operation. As the dimensions of a material decrease, the surface plays an increasingly important role and other defects, such as dopants and dislocations, may behave differently than in bulk material.

A detailed discussion of the minority carrier diffusion length is provided in the next chapter, but its importance is initially emphasized here. The minority carrier diffusion length is the characteristic distance for the decay of an excess carrier population. There are two types of mobile charge carriers in semiconductors: negatively

charged electrons and positively charged holes. Depending on the properties of the semiconductor, there will be more holes than electrons (p-type) or more electrons than holes (n-type). The distance a minority carrier diffuses after its creation until it decays by recombining with a majority carrier, or via a defect site, is the minority carrier diffusion length. For distances less than the diffusion length, excess charge carriers are present and moving, creating useful current. That current can then, for instance, be used to store energy or process information. For distances greater than this length, those carriers are not present, so there is no current and, therefore, no way to store energy, process information, or do other useful work. The minority carrier diffusion length is often considered a fundamental measure of material quality.

E. GALLIUM NITRIDE NANOWIRES AND ZINC OXIDE NANOSTRUCTURES

The potential applications of gallium nitride (GaN) nanowires have generated much interest. Bulk wurtzite GaN is a semiconductor with a wide band-gap of 3.505 electron volts (eV) at room temperature, making it useful for many optoelectronic applications, such as LEDs capable of producing light in a range of wavelengths from yellow to ultraviolet [13]. Blue LEDs, in particular, are important components of high-density optical memory [13]. Furthermore, it has also been shown that it is possible to construct a continuous wave blue laser based on GaN [13]. Thus, the optical properties of GaN nanowires suggest wide potential applications that include LEDs, laser diodes, sensors, and other nanophotonic devices [14].

Like GaN, ZnO is also a wide band-gap material ($E_g = 3.37$ eV at room temperature) with potential optoelectronic applications [15]. Both ZnO nanobelts and nanowires have demonstrated lasing properties [15]. Also, ZnO nanowire arrays demonstrate field emission behavior, promising potential applications such as field emitters in flat panel displays [15]. Researchers at EMPA, the Swiss Federal Laboratories for Materials Science and Technology, have recently grown sea urchin shaped nanostructures whose spines consist of ZnO nanowires [16]. These ZnO

structures are important for they could increase the efficiency of photovoltaic devices, which may eventually bring down the cost of solar power.

Many of the applications just described are minority carrier devices. Thus, an understanding of the minority carrier diffusion length, and a means for direct measurement of this length in ZnO and GaN nanostructures, is critical to developing these applications. The remainder of this thesis is, therefore, devoted to developing a basic understanding of the minority carrier diffusion length, describing the near field optical scanning technique used to measure it in ZnO and GaN nanostructures, and summarizing and analyzing the results.

II. MINORITY CARRIER DIFFUSION LENGTH

A. SEMICONDUCTOR BASICS

The importance of minority carrier diffusion cannot be understood without an understanding of basic semiconductor theory. Semiconductors contain ranges of energy levels, called energy bands, of which two, the valence and conduction bands, are critical to semiconductor applications. At the lowest energy state of an intrinsic semiconductor (i.e. $T = 0$ K), all energy levels at or below the valence band contain electrons, but all energy levels at or above the conduction band are void of electrons [17]. When energy is then applied to the semiconductor, electrons from the valence band will gain enough energy to enter the conduction band if the applied energy is greater than the energy difference between the valence and conduction bands, the band gap [17]. When an electron leaves the valence band to enter the conduction band, the energy state it occupied in the valence band is now empty [17]. This empty energy state is called a hole, and, since an electron is negatively charged, a hole is positively charged.

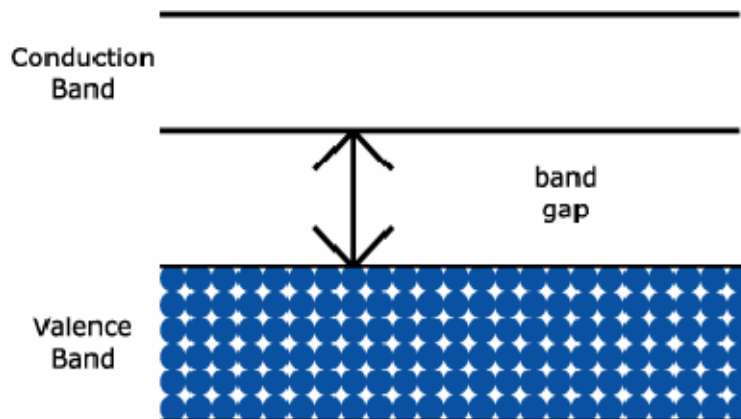


Figure 2. Energy Band Diagram of a Generic Semiconductor (from [18])

B. MINORITY CARRIER DIFFUSION

If no external forces are present, such as an electric field, diffusion is the mechanism responsible for both electron movement in the conduction band and hole movement in the valence band. Thermal motion will cause a non-equilibrium population of holes or electrons within a semiconductor to diffuse until they are uniformly distributed throughout the semiconductor's volume [17]. To illustrate, consider exciting only a small portion of semiconductor. If the excitation energy is greater than the material's band gap, electrons from the valence band will enter the conduction band, leaving holes in the valence band. The greatest concentration of electrons and holes is at the point of excitation. Therefore, diffusion, seeking a uniform distribution, will cause both the conduction band electrons and valence band holes to move away from the excitation source.

In equilibrium, most semiconductor devices do not have an equal number of electrons and holes. They are doped, meaning that they have an excess of electrons or an excess of holes. This excess could be unintentional, caused by defects or irregularities in their growth process, or, as is often the case, intentional due to the controlled addition of dopants. A material that contains an excess of holes is said to be doped p-type, and a material with more electrons is n-type. For example, consider a p-type material. In such a material, a concentration of holes is present in the valence band that is greater than the concentration of electrons in the conduction band. When excited, electrons in the valence band will enter the conduction band and diffuse. Likewise, in an n-type material, the conduction band contains a majority concentration of electrons. Thus, when excited, electrons in the valence band will enter the conduction band leaving holes behind. Those holes will then diffuse. Eventually the minority carriers, holes in an n-type material or electrons in p-type materials, will recombine with the majority carrier in the opposing energy band, releasing energy. For the materials analyzed in this thesis, some fraction of the released energy is in the form of light.

The minority carrier diffusion length, L_d , is the characteristic length a minority carrier will diffuse before it recombines with a majority carrier. It is described mathematically as

$$L_d = \sqrt{\frac{kT}{e}} \mu \tau$$

where k is Boltzmann's constant, T is the temperature, μ is the minority carrier mobility, and τ is the lifetime of the minority carrier. Thus, the length a minority carrier will diffuse depends upon temperature, how easily it moves through the material, μ , and the length of time between its creation and recombination with a majority carrier or a defect state, τ .

In this thesis, minority carrier diffusion lengths of ZnO and GaN nanostructures were measured using a novel technique: near field scanning microscopy combined with atomic force microscopy. This technique allowed the author to capture light generated from minority carrier recombination. The minority carrier diffusion length was then extracted from this optical distribution. The next chapter describes the technique in detail.

THIS PAGE INTENTIONALLY LEFT BLANK

III. IMAGING CHARGE TRANSPORT

A. IMAGING CHARGE TRANSPORT VERSUS EBIC

There are two types of characterization techniques that one can use to directly measure the minority carrier diffusion length in materials: electron beam induced current (EBIC) and imaging charge transport. EBIC measurements require a Schottky-Ohmic contact pair. The Schottky contact, which is needed because it creates an internal electric field, is usually created by depositing a thin film of metal on the semiconductor. The conduction and valence band energy levels of the semiconductor do not equal those of the metal, and as a result there is a band discontinuity at the metal-semiconductor interface. A space charge region and an electric field are formed at the Schottky contact. If, for instance, EBIC measurements were made inside a scanning electron microscope (SEM), as shown in Figure 3, the SEM's electron beam would be used to excite the semiconductor, generating electron-hole pairs. Minority carriers would then diffuse, with some eventually reaching the Schottky contact where they would be accelerated by the electric field at the metal-semiconductor junction, creating current in the external circuit. The minority carrier diffusion length could then be extracted from the measured current according to

$$I \sim I_0 e^{-x/L_d}$$

where I is current, I_0 is the maximum current, x is the distance of the generation by the electron beam from the metal-semiconductor interface of the electrical contact, and L_d is the minority carrier diffusion length [19].

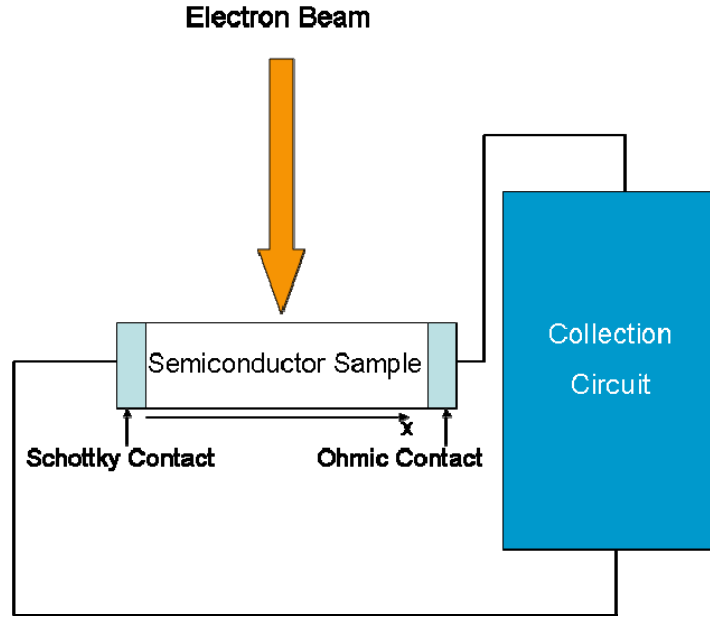


Figure 3. EBIC Configuration for Measuring Minority Carrier Diffusion Length

EBIC is capable of making precise and accurate minority carrier diffusion length measurements, but it is a difficult measurement to make on nanostructures because it requires making nanoscale electrical contacts, a difficult and time consuming process, and it is spatially restricted to providing information about the area immediately adjacent to the contact. In contrast, imaging charge transport techniques, which depend upon measuring the spatial variation of cathodoluminescence (CL), are not spatially restricted and do not require electrical contacts.

B. CATHODOLUMINESCENCE

Cathodoluminescence is the emission of light caused by the interaction of electrons generated from an electron gun, such as a cathode ray tube, with another substance, which, in this thesis, is a semiconductor [20]. When electrons impact the semiconductor, electron-hole pairs are created and diffuse. When a minority charge carrier eventually recombines with a majority carrier across the band gap, the wavelength of the emitted light, λ , is

$$\lambda = \frac{hc}{E_g}$$

where h is Planck's constant, c is the speed of light, and E_g is the band gap energy. Thus, with a spectrometer, it is possible to determine the intensity of emitted photons as a function of wavelength, as shown for CL from ZnO in Figure 4. The band edge luminescence, the shorter wavelength peak, is due to recombination across the band gap, while the longer wavelength broad peak (lower energy peak) is caused by recombination via midgap defects or surface states in the material.

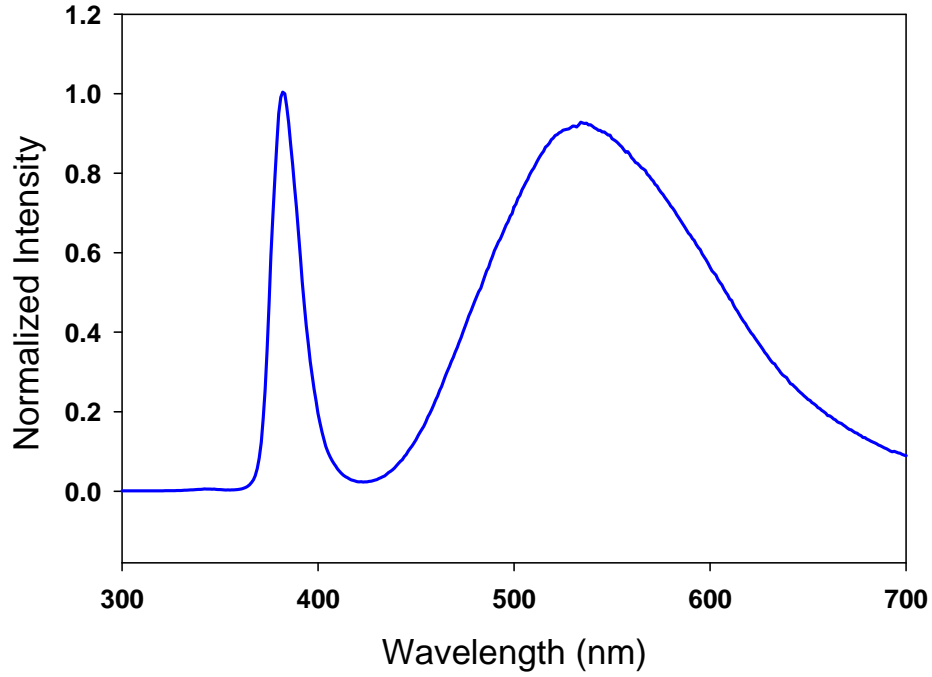


Figure 4. Normalized 300 K CL Spectrum of a ZnO Nanowire

If coupled with optical imaging, CL can also be used to image charge transport in bulk and thin film semiconductors. One approach is to place the semiconductor in a SEM with an optical microscope and a charge coupled device (CCD) camera. SEMs operate by generating an electron beam that scans the sample to form an image. That beam can, however, also be used to excite the semiconductor at one specific location, which is called spot mode, creating minority carriers that diffuse from only one point of the

sample. Thus, if the electron beam is kept in spot mode, the CCD camera will acquire a spatially resolved image of the resultant CL distribution, as shown in Figure 5.

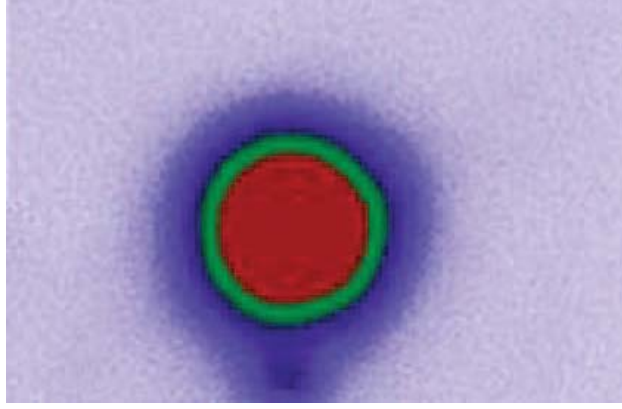


Figure 5. 2D Image of intensity distribution due to diffusion in a GaAs heterostructure. Variations in intensity are indicated by false color imaging. The beam generates charge at a single spot in the center of the image. Size of image is $193 \mu\text{m}$ width by $87 \mu\text{m}$ height (from [21]).

For minority carrier generation from a point source, the resultant minority carrier distribution, ϖ , is

$$\varpi(x, y) = \frac{g}{2L^2\pi} e^{(Sx/2L^2)} K_0 \left(\frac{\sqrt{S^2 + 4L^2}}{2L^2} r \right)$$

where S is the drift length, L is the diffusion length, g is proportional to the generation rate of minority carriers, and K_0 is the zeroth-order modified Bessel function of the second kind [21]. Luber *et al.*, showed that the resultant minority carrier distribution from a finite generation region can be modeled using a Gaussian form of the minority carrier generation distribution function:

$$\varpi(x, y) = \frac{gn}{2L^2\pi^2} \int_{-\infty}^{\infty} \int_{-\infty}^{\infty} e^{-[n(\eta^2 + \xi^2)]} e^{[S(x-\eta)/2L^2]} \times \\ K_0 \left(\frac{\sqrt{S^2 + 4L^2}}{2L^2} \sqrt{(x-\eta)^2 + (y-\xi)^2} \right) d\eta d\xi$$

where η and ξ are the integration variables in x and y [21]. If the distance x from the point of excitation is large, greater than or equal to $\sim 5L$, K_0 can be approximated as an independent decaying exponential [21]. Thus, the distribution is approximated as

$$I \sim e^{C^*x}$$

where C is

$$\frac{S}{2L^2} + \frac{-\sqrt{S^2 + 4L^2}}{2L^2} = \frac{S - \sqrt{S^2 + 4L^2}}{2L^2}$$

which can be simplified to

$$C = \left(\frac{e}{2kT}\right)E - \sqrt{\left(\frac{e}{2kT}\right)^2 E^2 + \frac{1}{L_d^2}}$$

where I is intensity, x is distance, k is Boltzmann's constant, T is temperature, and L_d is the diffusion length [21]. If no electric field is present ($E = 0$), so all motion is due to diffusion, then

$$I \sim e^{\frac{-x}{L_d}}$$

in this large x limit.

To illustrate, consider Figure 6, which is a plot of normalized intensity versus distance for different bias, and therefore electric field, values. The red +0 V line is the line scan through the two dimensional image shown in Figure 5. Figure 6 (b) is a semi-logarithmic plot with linear regression fits of the tail region of the data shown in Figure 6 (a). By calculating the slopes of the lines in Figure 6 (b), one can determine C for each bias value and, since E is known, then solve for L_d . This provides then a contact-free method for determination of L_d .

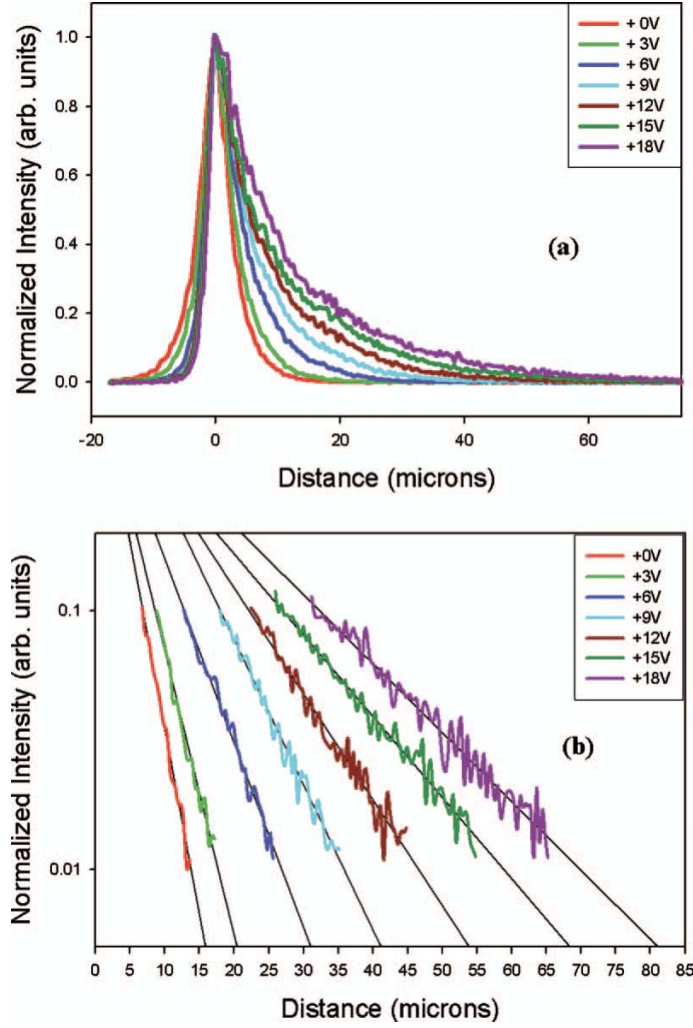


Figure 6. (a) Line scans through 2D intensity images showing effects of diffusion and drift (from [21]). (b) Semi-logarithmic plots of the tail region of (a) with linear regression (from [21]).

Due to diffraction limitations, each pixel of the silicon CCD camera used in this technique maps to a region of approximately 400 nm. Diffusion lengths for the nanostructures analyzed in this thesis are expected to be of this order of magnitude. Therefore, only one to two pixels would detect the CL generated from minority carrier recombination, so it is not possible to construct a spatially resolved image of minority carrier diffusion from which the minority carrier diffusion length can be extracted. Thus, one cannot use this camera approach, which is characterized as a far field technique, to obtain minority carrier diffusion length measurements in the nanostructures of interest.

C. DIFFRACTION

An understanding of diffraction is critical to an understanding of far and near field imaging. Diffraction can be described as any deviation of a wave front when that wave encounters an obstacle [22]. Thus, since light has wave properties, it will be affected by obstacles in its path. Of particular interest is what happens to light when it encounters small openings, such as the circular aperture of a camera or a microscope.

D. FAR FIELD IMAGING

In the far field, the lens of the optical device is many wavelengths away from the sample being imaged [23]. In this regime, after a beam of light passes through a circular aperture, it will spread. The light beam will form a circular diffraction pattern, called an Airy disk, whose radius increases with distance [22]:

$$r = \frac{L * 1.22\lambda}{D}$$

where r is the radius, λ is the wavelength of light, L is the distance between the object being imaged and the aperture, and D is the diameter of the lens. The angular separation of the Airy disk is defined as

$$\Delta\theta = \frac{1.22\lambda}{D}.$$

Rayleigh's criterion for just-resolvable images requires that the angular separation of the centers of image patterns not be less than the Airy disk's angular separation [22], as shown Figure 7. This translates to a minimum resolvable distance of two objects near the focal plane, x_{\min} , of

$$x_{\min} = f\Delta\theta$$

where f is the focal length of the optical system [22]. In an optical microscope, for instance, this results in an x_{\min} of approximately λ [22]. The most sophisticated far field optical systems can push the value of x_{\min} to a theoretical limit of $\lambda/2$, but no further [23].

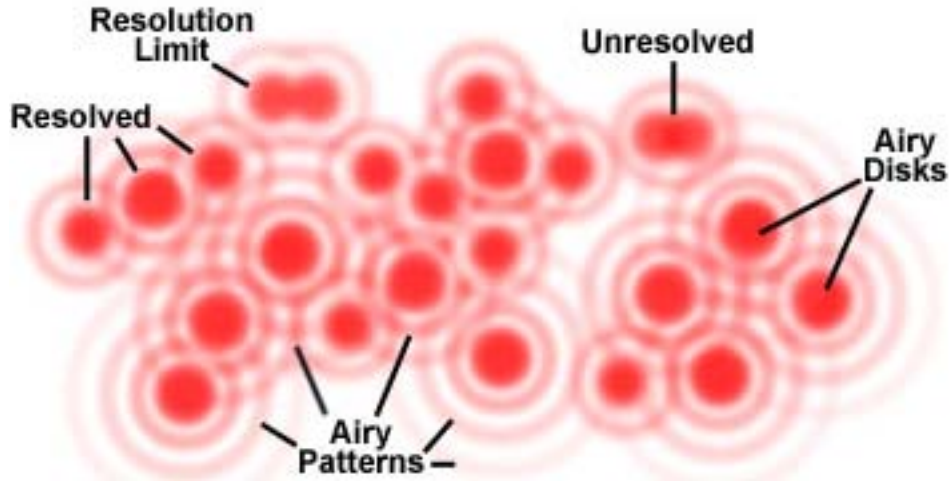


Figure 7. Schematic Illustration of Airy Patterns and Resolution (from [24])

For all the ZnO nanostructures analyzed in this thesis, the luminescence peaks at approximately 360 - 380 nm. The best far field optical systems would, therefore, only be capable of imaging objects that are approximately 190 nm apart. If the optical system were detecting the broad defect peak of Figure 4, which is highest at approximately 530 nm, it would only be capable of resolving distances greater than approximately 265 nm. As is detailed in the sixth chapter, Experimental Results, some of the measured diffusion lengths in this thesis are as low as 150 nm. Thus, it is not possible to use far field techniques to acquire a spatially resolved image from which the minority carrier diffusion length of these structures can be extracted.

E. NEAR FIELD IMAGING WITH NEAR FIELD SCANNING OPTICAL MICROSCOPY

Near field scanning optical microscopy (NSOM) overcomes the diffraction limit of far field techniques. By placing an NSOM probe close, a distance less than λ , to the surface of the sample, photons are not diffracted significantly. Furthermore, at such close distances, near field evanescent waves, which do not exist in the far field, are present and provide spatial information that increases resolution. In this thesis, the aperture of the NSOM probe ranges in diameter from 100 nm to 1000 nm. The NSOM probe (an optical

fiber) is used simultaneously as an AFM probe in feedback to keep the tip very close, much less than λ , to the nanostructure emitting the light.

The NSOM probe is a drawn fiber optic waveguide that transmits collected photons to a photon detector. The semiconductor nanostructure being imaged is excited using the electron beam of the SEM in spot mode. Next, the NSOM probe scans the sample. The photon detector then records the intensity of collected light as a function of position, as shown in Figure 8. Light intensity data as a function of distance along the axis of the wire, the blue line in Figure 8, can then be extracted and plotted, as shown in Figure 9. For a one dimensional structure, such as a nanowire, intensity is

$$I = \frac{g}{2L_d} e^{-x/L_d}$$

where g is the generation rate of electron-hole pairs. Thus, the minority carrier diffusion length can be extracted from a slope of the semi-logarithmic plot of the data contained in Figure 9, as shown in Figure 10. For this example, the minority carrier diffusion length is 200 nm.

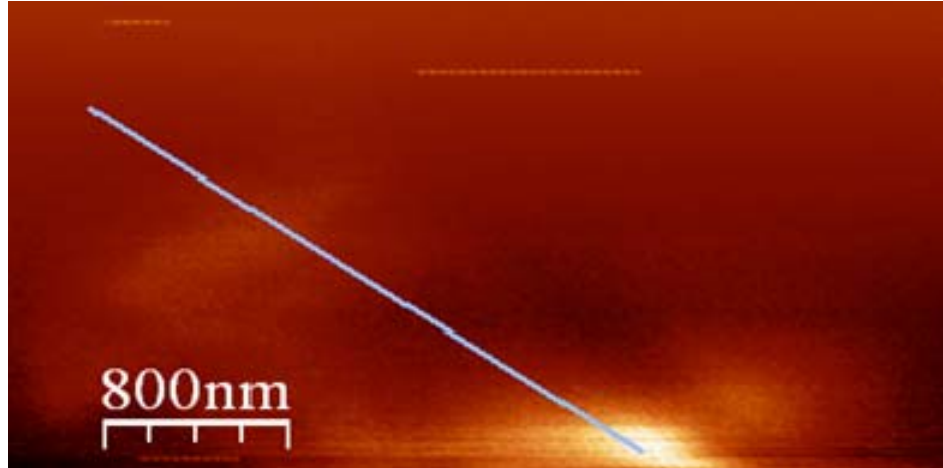


Figure 8. Light collected with NSOM from an unintentionally doped n-type GaN nanowire. The blue line represents the axis of the wire. The electron beam is incident at a point immediately before the blue line at the bottom of the figure.

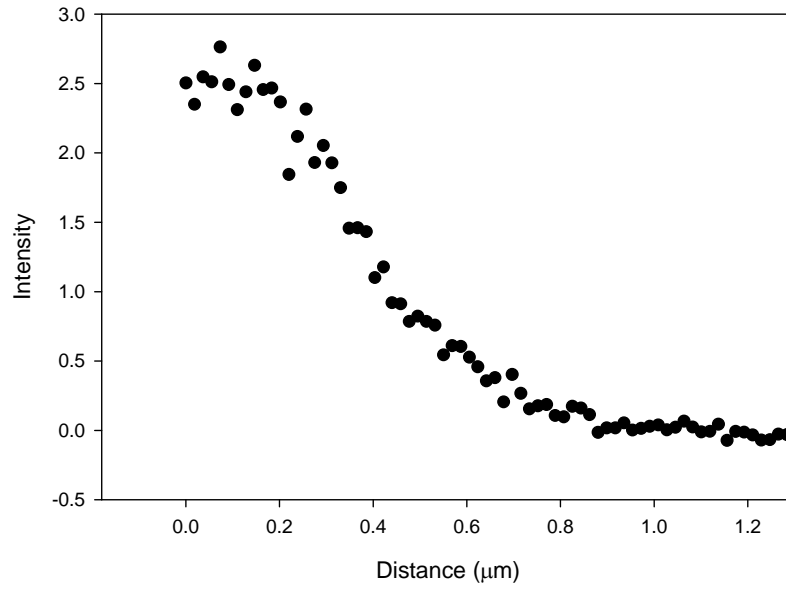


Figure 9. Intensity of light as a function of distance along the axis, the blue line, of the nanowire shown in Figure 8.

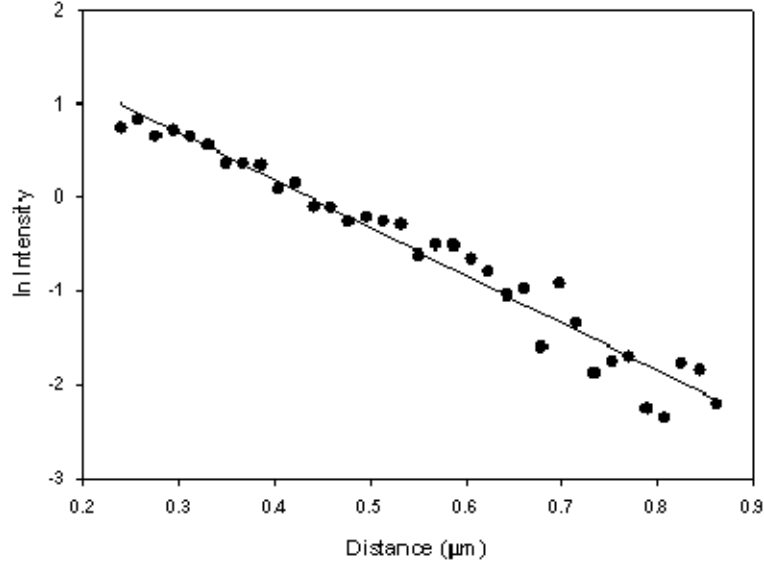


Figure 10. Semi-logarithmic plot of the data in Figure 9

AFM feedback maintains the probe just nanometers above the surface of the sample [25]. Forces acting on the tip are a combination of long range forces, such as van

der Waals forces, and short range forces, such as chemical bonding forces [26] (Figure 11). In this thesis, the AFM probe is a cantilever that is dynamically vibrating at its resonance frequency on a tuning fork. Any change in height, the z -axis of Figure 11, will change the forces acting on the AFM probe, and, therefore, also affect the phase and amplitude of the frequency at which the cantilever is oscillating. Using a feedback system that monitors the phase or amplitude of oscillations, the height of the AFM probe is adjusted to maintain a constant phase or amplitude. Thus, a constant height above the sample is also maintained. The next chapter describes the combined NSOM/AFM system used in this research in detail.

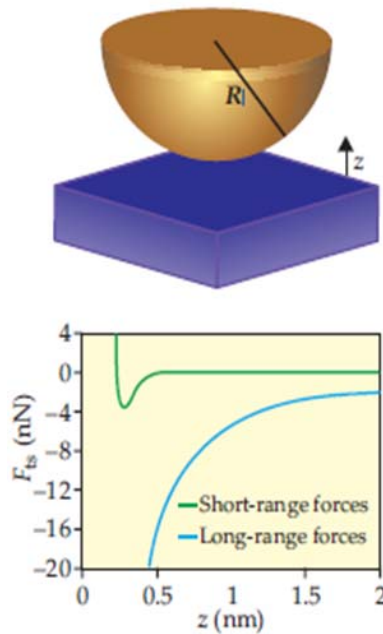


Figure 11. Forces on an AFM Tip (from [25])

THIS PAGE INTENTIONALLY LEFT BLANK

IV. EXPERIMENTAL SETUP

A. EQUIPMENT

Near field imaging of charge carrier transport was conducted with an integrated AFM and NSOM system inside a SEM. The SEM is a JEOL 840A and the NSOM/AFM system is the MultiView 2000 manufactured by Nanonics LTD. Additionally, two photon detectors were used: the Perkin-Elmer MP-983 and the Perkin-Elmer SPCM-AQR-14. Figure 12 shows the equipment used for experiments in this thesis.

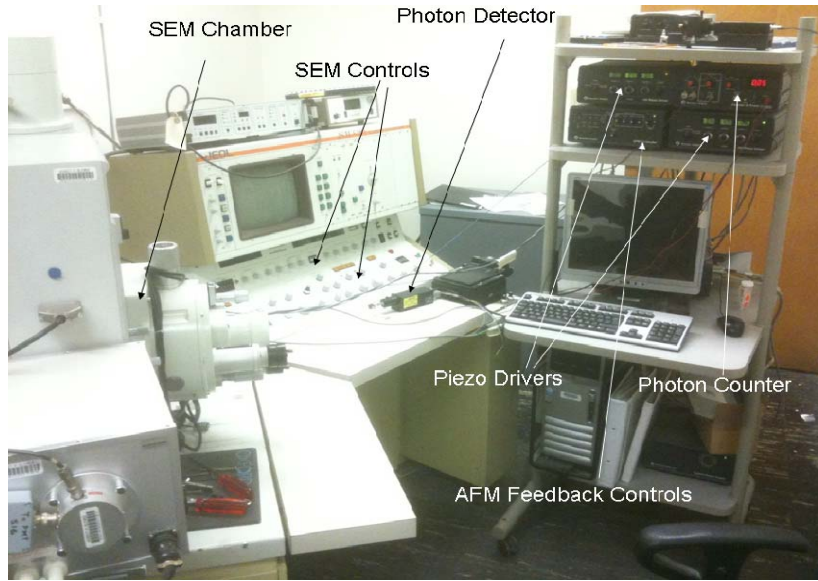


Figure 12. Overview of Experimental Equipment

1. SEM

The JEOL 840A scanning electron microscope generates electrons thermionically from a tungsten filament into an evacuated environment. The electrons are focused into a beam whose diameter is a function of current. Table 1 summarizes surface spot size of the beam at 30 keV in the SEM for currents of 3×10^{-11} A to 10^{-9} A. The electron beam is focused by passing it through scanning coils in the objective lens that horizontally and vertically deflects it. In this thesis, the SEM was operated in one of three modes: picture, line, and spot.

Probe Current (A)	16%-24% (2σ) (nm)	FWHM (nm)
3×10^{-11}	39	46
1×10^{-10}	48	56
3×10^{-10}	107	126
1×10^{-9}	139	163

Table 1. Beam Diameter as a Function of Probe Current at 30 keV (from [27])

When operating in picture mode, the electron beam performs a line-by-line scan of a rectangular area by deflecting the beam both horizontally and vertically. This is known as a raster scan, and the SEM performs this at a rate of 60 Hz [28]. When the beam is incident on the sample, secondary electrons, whose intensity varies with the topography of the sample, are emitted [27]. It is these variations that provide the SEM image [27].

In line mode, the beam is deflected horizontally, but not vertically [28]. The beam, therefore, scans along a single horizontal line, hence the name. In this mode, it is not possible to generate a picture, and there is no visual feedback to the operator.

In spot mode the beam is neither deflected horizontally nor vertically [28]. Thus, the beam hits only at a single point of the sample. The size of the area excited by the beam is, as shown in Table 1, a function of current and of the energy of the incident electrons. As in line mode, visual back is also not possible in this mode.

2. NSOM/AFM

The Nanonics MultiView 2000 is the NSOM/AFM system used in this thesis. The system consists of an integrated AFM and NSOM probe that provides unobstructed optical access to the sample. With both top and bottom scanning plates, the system is also capable of independent tip and sample scanning.

The integrated probe is connected to a photon detector via an optical fiber. The photon detector, either an avalanche photodiode or a photomultiplier tube, serves as a photon counter that sends light intensity data to a Nanonics software program that combines this data with position data. Figures 13 through 16 details the MultiView 2000 and how it was integrated into the JEOL 840A SEM.



Figure 13. Nanonics MultiView 2000

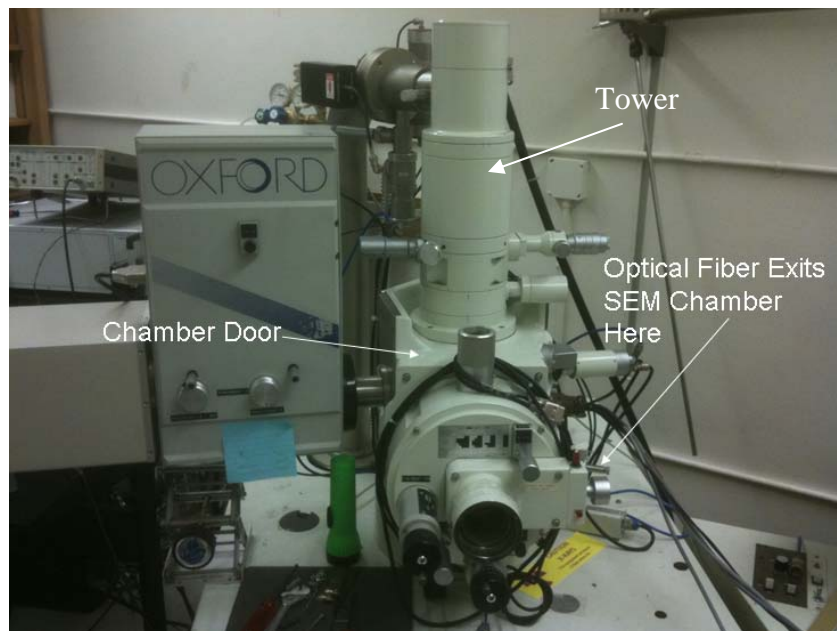


Figure 14. SEM Chamber and Tower

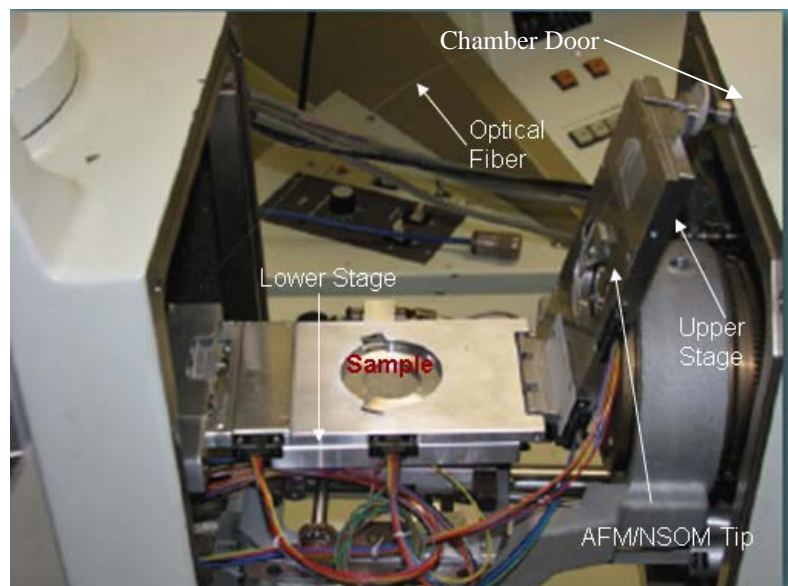


Figure 15. Nanonics MultiView 2000 Inside the SEM Chamber



Figure 16. Optical Fiber Exiting SEM Chamber

In the MultiView 2000 system, AFM is performed with tuning fork feedback. Figure 17 details the AFM/NSOM tuning fork apparatus. The cantilever probe, which in this system is also the tip of the NSOM fiber, is glued to the tuning fork. Figure 18 is a SEM picture of the probe tip. As explained in the previous chapter, the probe is

dynamically vibrating at the resonant frequency of the tuning fork, and any change in the height of the probe will cause the phase and amplitude of cantilever oscillations to deviate from the free space resonance. Thus, by employing a phase or amplitude feedback system to adjust probe height in order to maintain a constant phase or amplitude, the probe height above the sample is also held constant. Since phase feedback is ten times more sensitive than amplitude feedback [28], only phase feedback was used in this thesis.

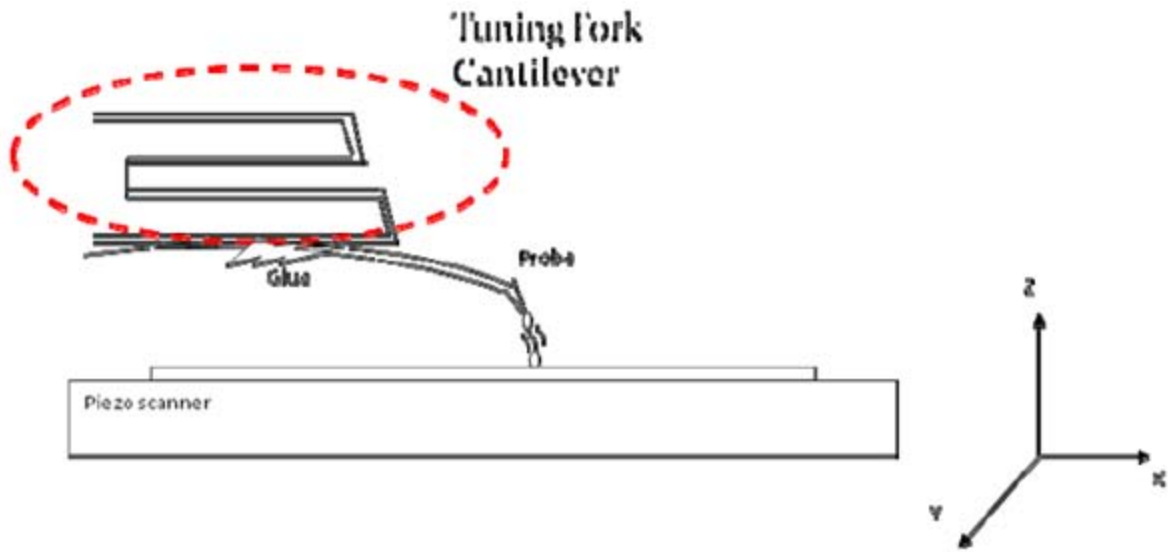


Figure 17. NSOM/AFM Probe Schematic (from [29])



Figure 18. SEM Picture of NSOM/AFM Tip (from [28])

As shown in Figure 13 and Figure 15, the MultiView 2000 provides an unobstructed view of the sample, so the SEM's electron beam has an unobstructed path to the nanostructure being imaged. This is critical to the transport imaging technique and unique to the MultiView 2000. Most AFM systems monitor probe motion with a laser-mirror combination that obstructs the view of the sample [28]. In such systems, the SEM's electron beam could not reach the sample, and, therefore, could not generate minority carriers that diffuse and generate light through recombination with majority carriers. Thus, NSOM is possible only in those systems, such as the MultiView 2000, that provide an unobstructed view of the sample.

NSOM diffusion measurements require that the electron beam remain fixed on a single location of the sample to provide a fixed source of carrier generation and ensure that minority carriers diffuse from only one location. This requires that the sample remain stationary while the NSOM collecting tip scans. Since the MultiView 2000 contains both top and bottom scanning plates that allow for tip and sample scanning respectively, this is possible with this system [30].

Figure 19 displays the high voltage (HV) piezo drivers for the upper and lower stages, the photon counter and power supply for the photon detector, and the scanning probe microscopy (SPM) controller. The SPM controller is used to adjust AFM feedback settings. Further information, and detailed specifications, of the MultiView 2000 are included as Appendix A.



Figure 19. Clockwise from Top Left Corner: Upper Stage HV Piezo Driver, Counter and Power Supply for the Photon Detector, Lower Stage HV Piezo Driver, and the SPM Controller

3. Photon Detectors

The Perkin-Elmer SPCM-AQR-14 photon detector is a silicon avalanche photodiode (APD) that can detect wavelengths of light from 400 nm to 1060 nm with a peak quantum efficiency of 65 percent at 650 nm [31]. Some GaN nanowire measurements were made using the SPCM-AQR-14 by utilizing the collection of the broad defect-related luminescence in the visible part of the spectrum. The Perkin-Elmer MP-983 is a channel photomultiplier detector optimized for ultraviolet (UV) detection that can detect wavelengths of light from 185 nm to 650 nm with a peak quantum efficiency of 20 percent from approximately 250 nm to 400 nm [32]. It is important to note that use of the MP-983 to detect UV light also requires the use of a UV optimized NSOM fiber. All ZnO nanostructure measurements and some GaN nanowire measurements were made using the MP-983 since this allows for the detection of UV band to band emission. Detector specifications are included as Appendix B (SPCM-AQR-14) and Appendix C (MP-983). Figure 20 and Figure 21 show the SPCM-AQR-14 and MP-983 respectively.



Figure 20. SPCM-AQR-14 Photon Detector



Figure 21. MP-983 Photon Detector

B. EXPERIMENTAL APPROACH

All diffusion length measurements were made with the SEM in spot mode. Line mode was used to map the standard CL emitted by some nanostructures the author has classified as “Other Nanostructures” (see Chapter VI), but no minority carrier diffusion

length measurements were made with this mode. Picture mode was used to locate nanostructures, position the tip on the nanostructure, and position the electron beam crosshairs for spot mode operation on the nanostructure. Picture mode was also used to determine the region for collection of the CL spectrum of nanostructures, such as the one shown in Figure 4.

Figure 22 shows a typical tip, beam, and nanostructure arrangement. Once positioned, the SEM will be set to spot mode and the picture will disappear, but the electron beam will remain stationary and centered just below the tip on the crosshairs. Finally, the tip, like the raster scan of the electron beam in picture mode, will scan horizontally across the screen, moving up vertically after each horizontal scan.

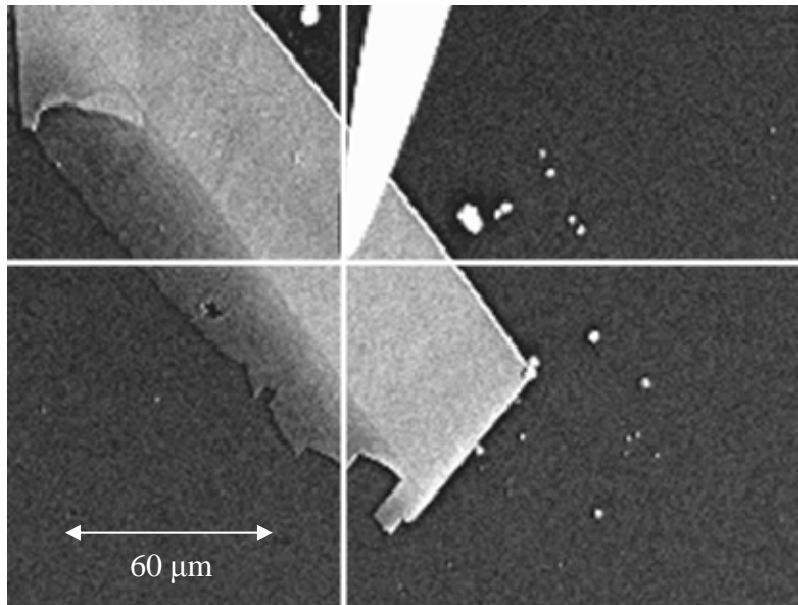


Figure 22. Typical Tip, Beam, and Nanostructure (ZnO Nanobelt) Arrangement

When taking NSOM measurements, there are several factors that must be addressed to obtain accurate results. Among the most important is limiting excess charge inside the SEM. Excess charge will, if the associated field is large enough, deflect the SEM's electron beam, causing picture distortion [28], thus making it difficult, perhaps impossible, to properly position the tip, beam, and nanostructure. To limit charge buildup, it is essential to ground the sample by placing a grounding strap from the sample

to the bottom stage. In this thesis, this was done by using copper tape and copper wire to connect the sample to the bottom stage. Also, as shown by Commander L. Baird, the glue that connects the NSOM fiber to the cantilever is a source of excess charge [28]. Recently, however, this has become less of an issue because the manufacturer, Nanonics, changed the type and reduced the amount of glue in response to Commander Baird's original results.

The most delicate, and challenging, portion of any NSOM measurement occurs at the intersection of the tip and sample. Both the tip and sample are fragile structures and are easily damaged or destroyed if they collide with too much force. Thus, to ensure proper and safe operation, the operator must first calibrate the AFM probe by performing the AFM lock-in procedure in NWS Ver 1760, the software program used to control AFM/NSOM scans. This sets the force level between tip and sample and creates the feedback loop to adjust the tip height during a scan. Those procedures are listed below.

1. In the LockIn window, select phase or amplitude feedback. In this thesis, only phase feedback was used.
2. Set the total gain. The default value recommended by the manufacturer is 60.
3. Conduct a magnitude sweep by selecting magnitude in the sweep signal box. Sweep over a range of frequencies that includes the manufacturer listed resonance frequency. This will result in a graph that peaks at the resonance frequency of the probe.
4. To increase the amplitude of the peak, increase the oscillation (OSC) out gain. To decrease the amplitude, decrease the OSC out gain. Repeat steps three and four until the amplitude of the peak is between the manufacturer recommend values of 8.0 and 8.5. When this is achieved, hit the set frequency button.
5. Depress the autophase button.

6. Conduct a squared sweep by selecting squared in the sweep signal box. Sweep over the same range of frequencies used in the third step.
7. In the graph produced by the previous step, move the red cursor to the position where the amplitude is zero.
8. Depress the set frequency button.
9. Click finish.

Even after the AFM lock-in procedure has been completed, the tip may still interact with nanostructures with enough force to cause damage. The danger of this can be limited, however, by limiting the set point. The set point controls the amount of force applied to the tip. To illustrate, imagine a level surface that suddenly increases in height, such as when a tip approaches a nanostructure from the substrate, and think of the set point as a spring that pushes down on the tip. A high set point, therefore, is similar to a strong spring pushing against the tip. This makes it difficult to increase the tip height when it encounters increases in elevation, but easy to decrease its height when it encounters decreases in elevation. Therefore, a high set point may not allow the tip to increase its height enough to avoid colliding with the nanostructure. A set point that is too low, though, will lose contact with sample, resulting in no topography data. Thus, when first beginning an NSOM scan, one should start with a low set point, which, in this thesis, was -0.5, and slowly increase it to the point that the AFM probe will respond to spatial changes in height without potentially deforming or moving the nanostructure of interest.

THIS PAGE INTENTIONALLY LEFT BLANK

V. NANOSTRUCTURE GROWTH PROCESSES

The nanostructures analyzed in this thesis were grown using one of three processes: hydrothermal (HT), molecular beam epitaxy (MBE), or physical vapor deposition (PVD). All GaN nanowires were grown by MBE. Some ZnO nanowires were synthesized by HT with the remainder manufactured by the PVD process. All ZnO nanobelts were grown by PVD. The ZnO nanostructures were grown by the students of Dr. Zhong L. Wang at the Georgia Institute of Technology. The GaN nanowires were grown by Kris Bertness *et al.*, at the National Institute of Standards and Technology. A brief overview of each growth technique is given below.

A. HYDROTHERMAL

In the hydrothermal method, crystals are grown in an aqueous solvent [33]. In its most general form, the hydrothermal process involves placing source material into a tube surrounded by heaters, suspending a seed crystal above the source, and then finally adding a water-based solution to the tube before it is sealed shut, as shown in Figure 23. If the source end of the tube is heated to a higher temperature than the seed crystals, dissolved source material will migrate toward the seed, crystallizing on its surface.

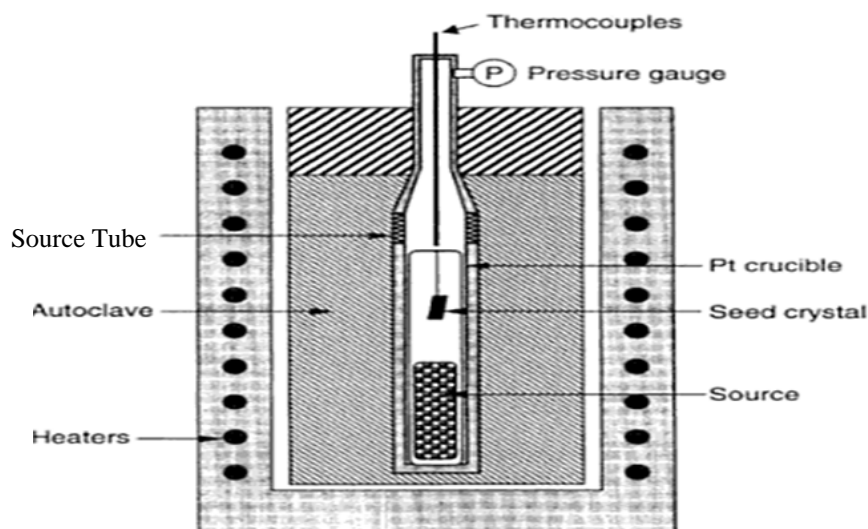


Figure 23. Hydrothermal Growth Process (from [33])

The specific growth process used by the researchers at Georgia Tech is a variant of this general process. Instead of using ZnO seeds, ZnO nanowires were grown directly onto a substrate. For example, a uniform crystalline thin layer of gold can be formed on a silicon substrate by depositing and annealing approximately 50 nm of gold onto that substrate [34]. When floated in a source solution, such as an aqueous solution that contains zinc nitrate and hexamethylenetetramine (HMTA), Zn^{2+} and O^{2-} ions will combine and then crystallize on the thin gold film, forming ZnO nanowires [34]. The growth process is controlled by adjusting reaction parameters, such as growth temperature or growth time [34]. For the transport studies in this thesis, all HT nanowires were transferred from the substrate on which they were grown to a silicon substrate that was not coated with thin films. The dimensions of the HT nanowires analyzed in this thesis are approximately 1 to 2 μm long by 200 to 500 nm wide. Figure 24 is a SEM image of nanowires grown by the HT process.

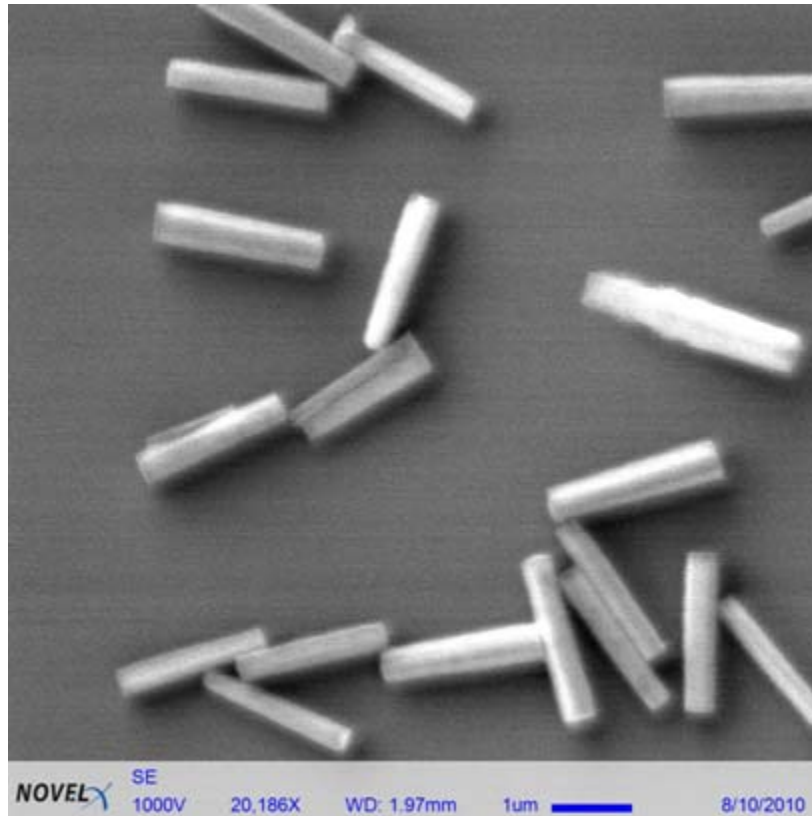


Figure 24. HT Grown Nanowires (20,186X)

B. MOLECULAR BEAM EPITAXY

In MBE, beams of atoms are produced by heating a solid source to a gas in an effusion cell. Those beams are then emitted from the effusion cell into a vacuum environment where they impact a hot substrate, forming a thin film [35]. The growth process is controlled by changing the evaporation conditions of the source material or by physically interrupting the beam using mechanical shutters placed between the effusion cells and the substrate [36]. The process is shown schematically in Figure 25.

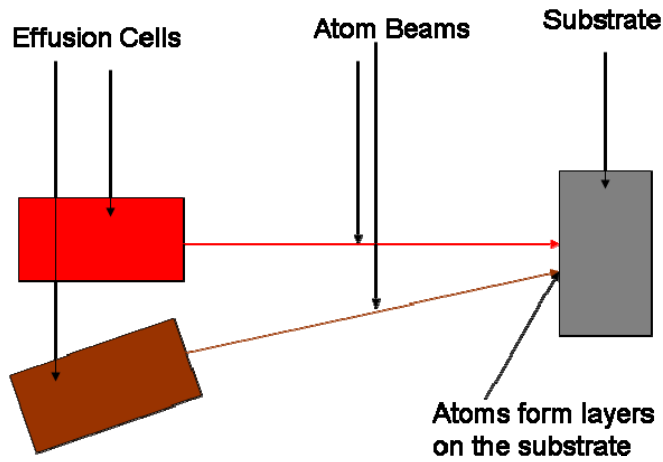


Figure 25. Simplified MBE Process

The GaN nanowires grown by NIST were synthesized in a conventional MBE system with Gallium (Ga) and Aluminum (Al) sources [37]. A radio frequency (RF) plasma nitrogen, N_2 , source was also used [37]. First, a thin 30 to 120 nm buffer layer of aluminum nitride (AlN) was grown on a silicon substrate [37]. Then, the nanowires are grown on the AlN substrate by imposing high temperatures (810 – 830 °C) with high N_2 overpressure to cause spontaneous nucleation of GaN nanowires [37]. The wurtzite structure wires grown with this method had hexagonal cross sections and widths of approximately 0.5 to 0.6 μm [37]. Again, all nanowires for NSOM transport imaging were transferred to a bare silicon substrate. Figure 26 shows a SEM image of GaN nanowires grown by the MBE process.

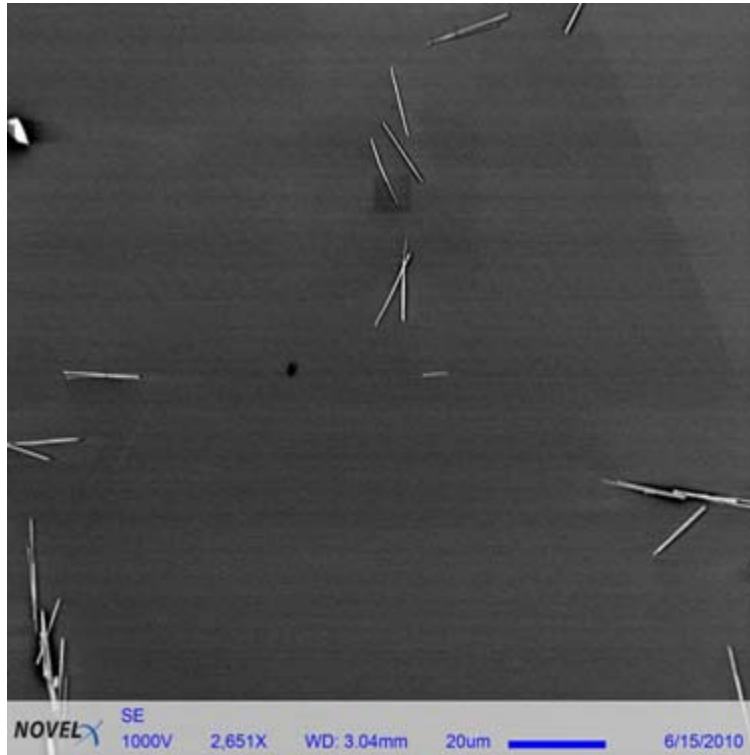


Figure 26. MBE Grown Nanowires (2,651X)

C. PHYSICAL VAPOR DEPOSITION

The basic PVD process consists of subjecting source materials in powder form to high temperatures to vaporize them in order to subsequently deposit the source material onto a substrate [38]. Typically, PVD synthesis is performed in an alumina or quartz tube located in a horizontal tube furnace [38]. Once vaporized, the source vapor is carried by inert gas to a lower temperature region where the vapor becomes supersaturated, thus allowing the excess solute in the vapor to crystallize [38]. Upon reaching the substrate, nucleation and growth of nanostructures begins [38]. The process is illustrated in Figure 27.

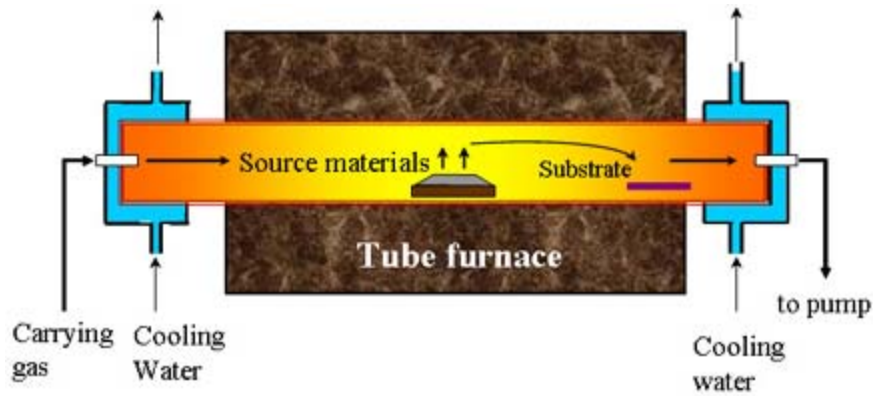


Figure 27. Simplified PVD Process (from [38])

Employing this process, Georgia Tech researchers grew ZnO nanobelts with rectangle like cross sections with widths that ranged from 30 nanometers to tens of micrometers, lengths up to millimeters, and thicknesses of a few nanometers to tens of nanometers [39]. With this method, they also grew nanowires that, for the studies in this thesis, had widths of up to 2 μm and lengths up to hundreds of micrometers. Figure 28 is a SEM image of PVD ZnO nanowires, and Figure 29 is a SEM image of a ZnO nanobelt.

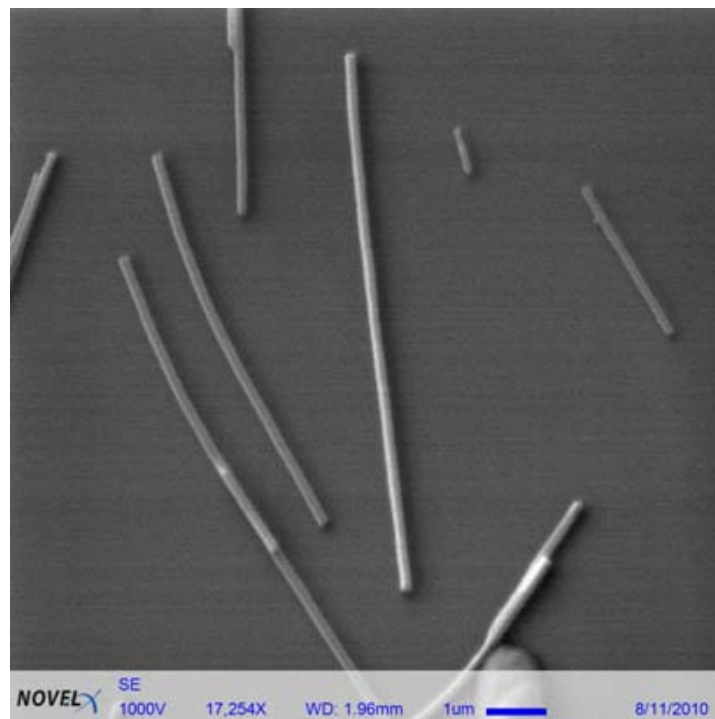


Figure 28. PVD ZnO Nanowires (17,254X)

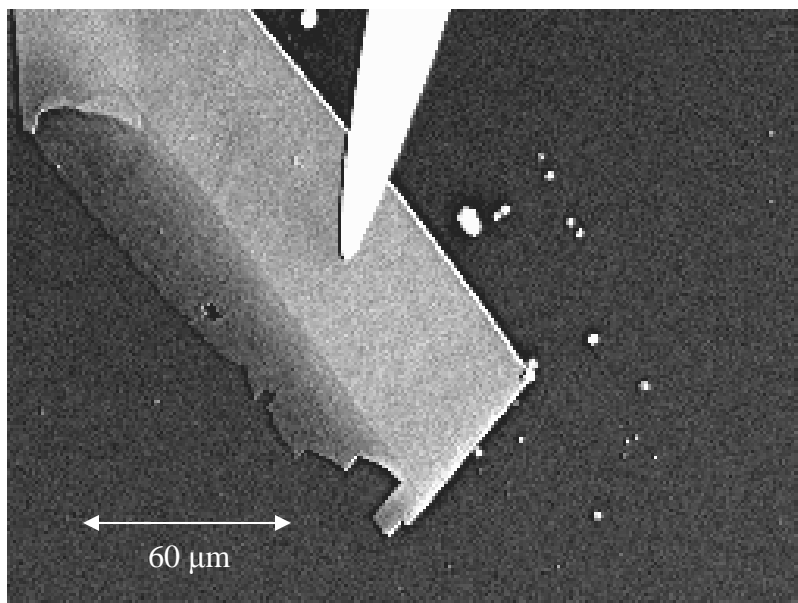


Figure 29. PVD ZnO Nanobelt (17,254X)

VI. EXPERIMENTAL RESULTS

In this chapter, results are presented for the following materials: p-type, n-type, and unintentionally doped n-type GaN nanowires; HT and PVD ZnO nanowires; PVD ZnO nanobelts; and ZnO other nanostructures, which are structures whose surface topographies are unique and not typical of nanowires or nanobelts. A summary of all measurements is presented at the end of this chapter in Table 2. The CL spectra of all nanostructures were measured before NSOM measurements were made to determine the intensity and wavelengths of emitted light, which in turn determined which photon detector to use and what diameter NSOM tip aperture would be needed (the less intense the light the larger the tip aperture required).

The “Other Nanostructures” category contains ZnO PVD nanostructures with unique topographic characteristics. A SEM image of a typical individual PVD ZnO nanowire is shown in Figure 30. The SEM image of a typical ZnO nanobelt is shown in Figure 31, and Figures 32 and 33 show examples of nanostructures with characteristics typical of those classified in the “Other Nanostructures” category. Note the variable topography of the structures in Figures 32 to 33 as compared to the uniform topographies of the nanowire in Figure 30 and the nanobelt in Figure 31. The structure in Figure 32, for instance, narrows at repeated points, like kinks in a water hose. Similarly, the structure in Figure 33 has an irregular ridge-like structure on its surface. These irregularities produce unique optical waveguiding and interference effects that impact minority carrier diffusion length measurements derived from transport imaging.

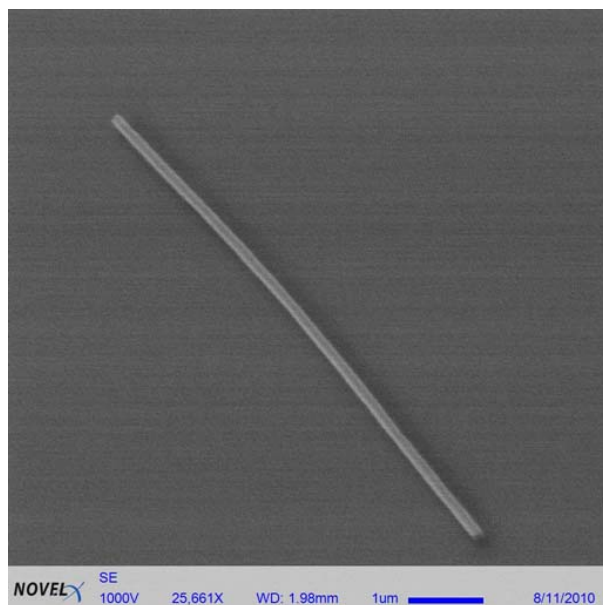


Figure 30. SEM Image (25,661X) of a Typical ZnO PVD Nanowire

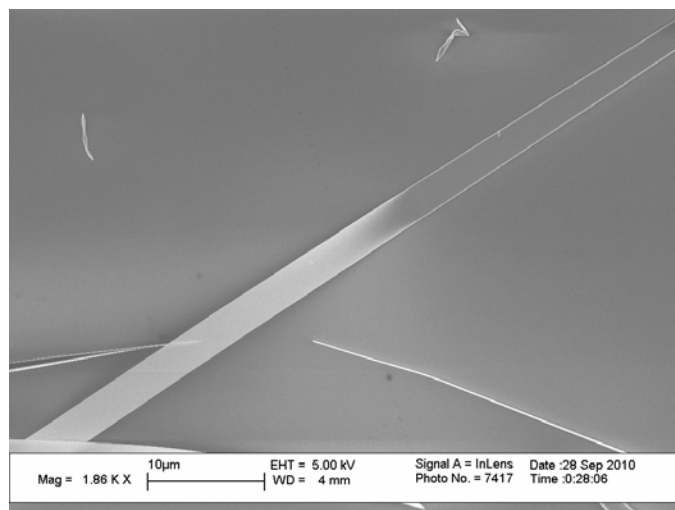


Figure 31. SEM image (1860X) of a typical PVD ZnO nanobelt. The long structure that spans from the lower left corner to the upper right corner is the nanobelt. Photo courtesy of Dr. Zhong Lin Wang of the Georgia Institute of Technology.

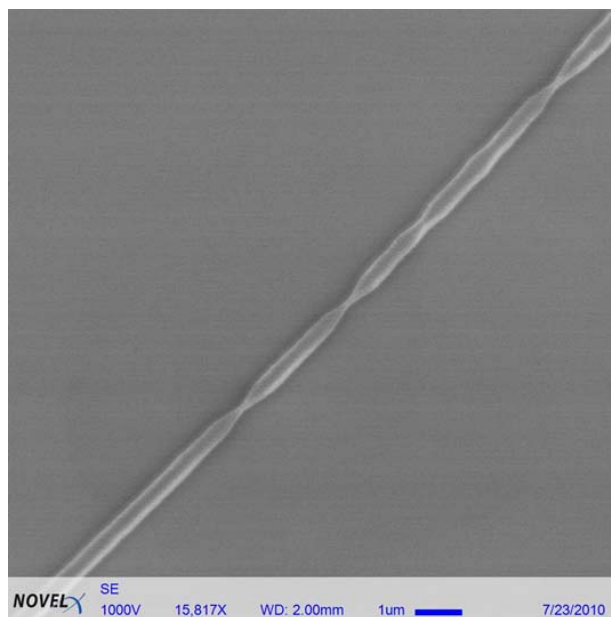


Figure 32. SEM Image (15,817X) of a Nanostructure with Variable Surface Topography

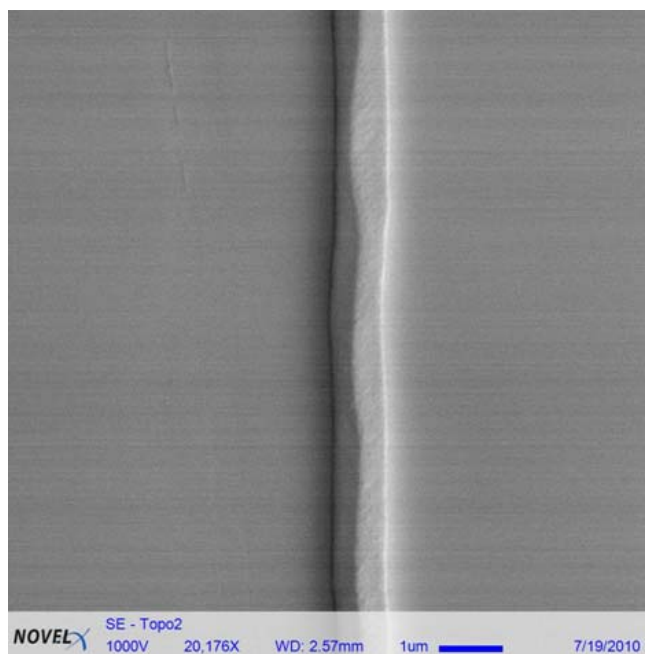


Figure 33. SEM Image (20,176X) of a Nanostructure with Variable Surface Topography

A. CATHODOLUMINESCENCE

As described earlier, cathodoluminescence (CL) measurements were made on all structures prior to transport imaging. CL was generated inside the JEOL 840A SEM with an acceleration voltage of 20 keV and a probe current of 6×10^{-10} A. CL was collected via a parabolic mirror, passed through a $\frac{1}{4}$ m grating monochromator, and detected by a GaAs photomultiplier tube.

1. GaN Nanowires

Figures 34 and 35 present the CL spectra of n-type, p-type, and unintentionally doped n-type GaN nanowires. The band-edge luminescence, as seen most clearly in Figure 35, is at 360 nm at room temperature. Also, note the luminescence at 450 nm for the p-type sample, and the broad defect peaks from 400 nm to approximately 700 nm for all the samples. At the time that the first measurements of these samples were made, the only available photon detector was the SPCM-AQR-14, which detects light from 400-1060 nm. Since all samples luminesce in this range, that was acceptable. However, for best results, a detector sensitive to the band-edge luminescence is needed. Therefore, the MP-983, sensitive to light of wavelengths from 185 nm to 650 nm, was procured and added to detection capability.

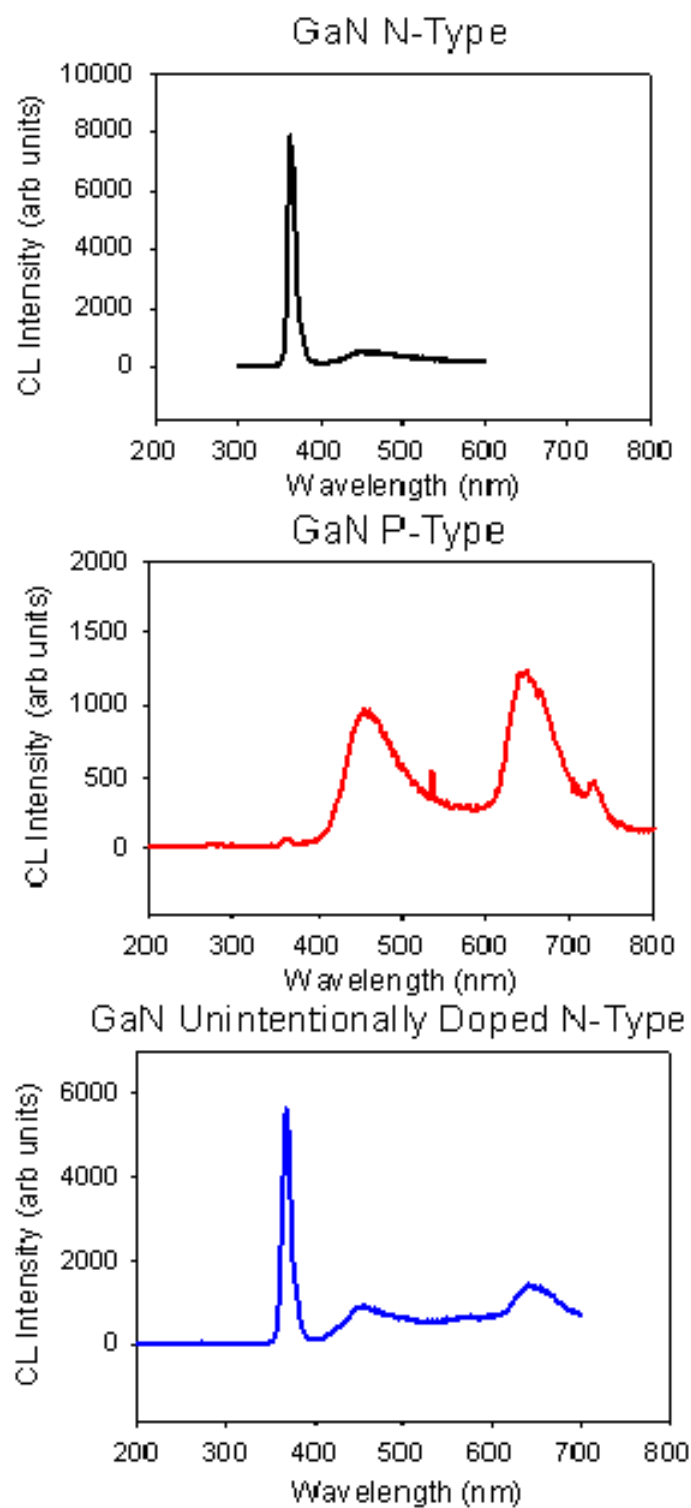


Figure 34. CL Spectra of GaN Nanowires at 300 K

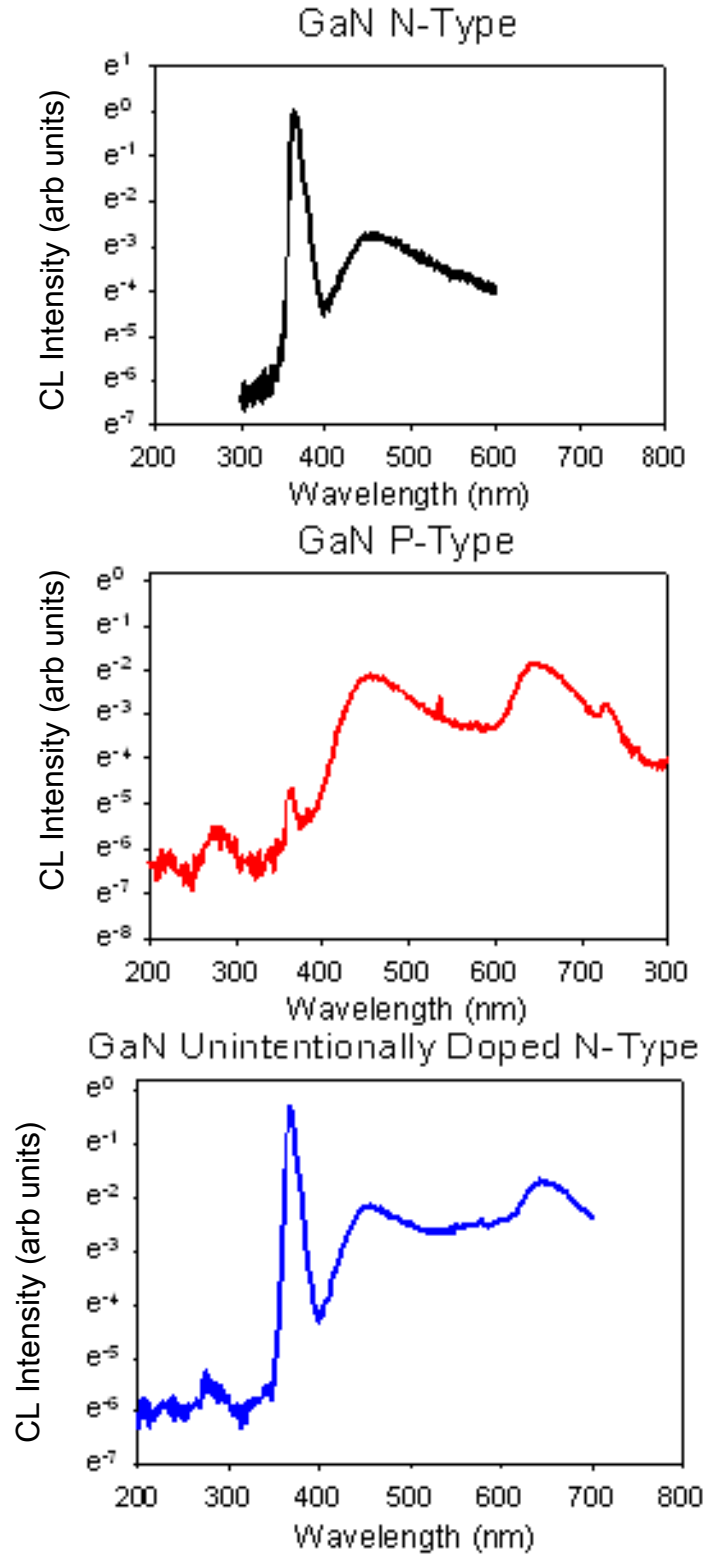


Figure 35. Semi Logarithmic Plot (Y-Axis Scale is the Natural Logarithm of Intensity) of the Normalized CL Spectra of GaN Nanowires at 300 K

2. ZnO Nanostructures

Room temperature CL of ZnO nanostructures was also performed. In Figure 36 and Figure 37 note that there are three spectra of PVD grown structures: the red, blue, and green lines. In this thesis, three samples composed of PVD nanostructures were tested, with the sample indicated by the red line in Figures 36 and 37 containing a mixture of PVD nanowires and nanobelts. The remaining sample, indicated by the black line, contained only HT nanowires. The overall intensity, as well as the ratio of band edge to defect luminescence, varies from sample to sample, even for a similar growth technique.

The band-edge luminescence, as seen most clearly in Figure 37, is at 380 nm. There is also a broad defect peak from 420 nm to 700 nm in all the samples, but this peak varies in intensity from sample to sample. In the HT sample it is actually greater in intensity than the band-edge luminescence. Thus, to ensure that as much light as possible was collected during NSOM measurements, the MP-983 photon detector, sensitive to both the band edge luminescence and defect luminescence, was used.

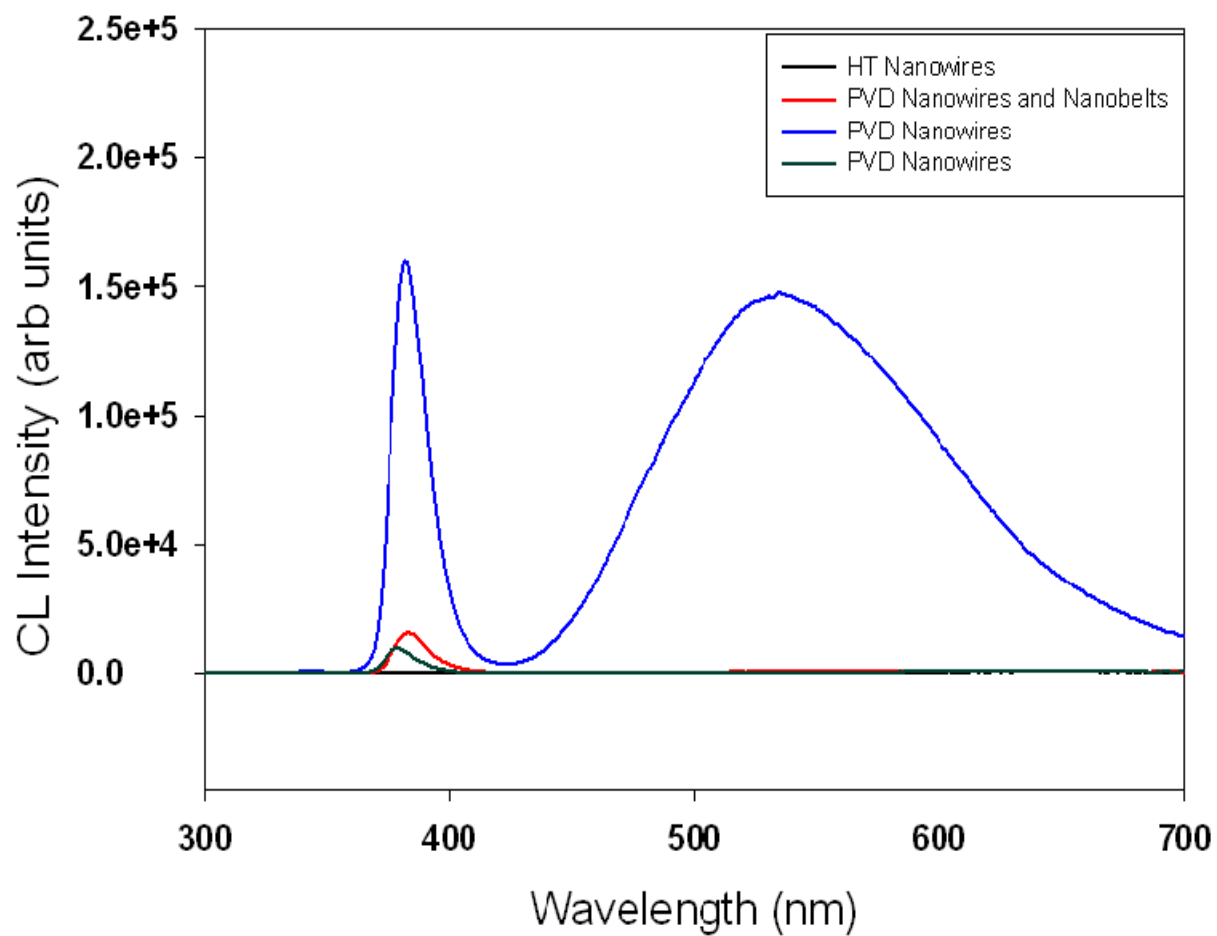


Figure 36. CL Spectra of ZnO Nanostructures at 300 K

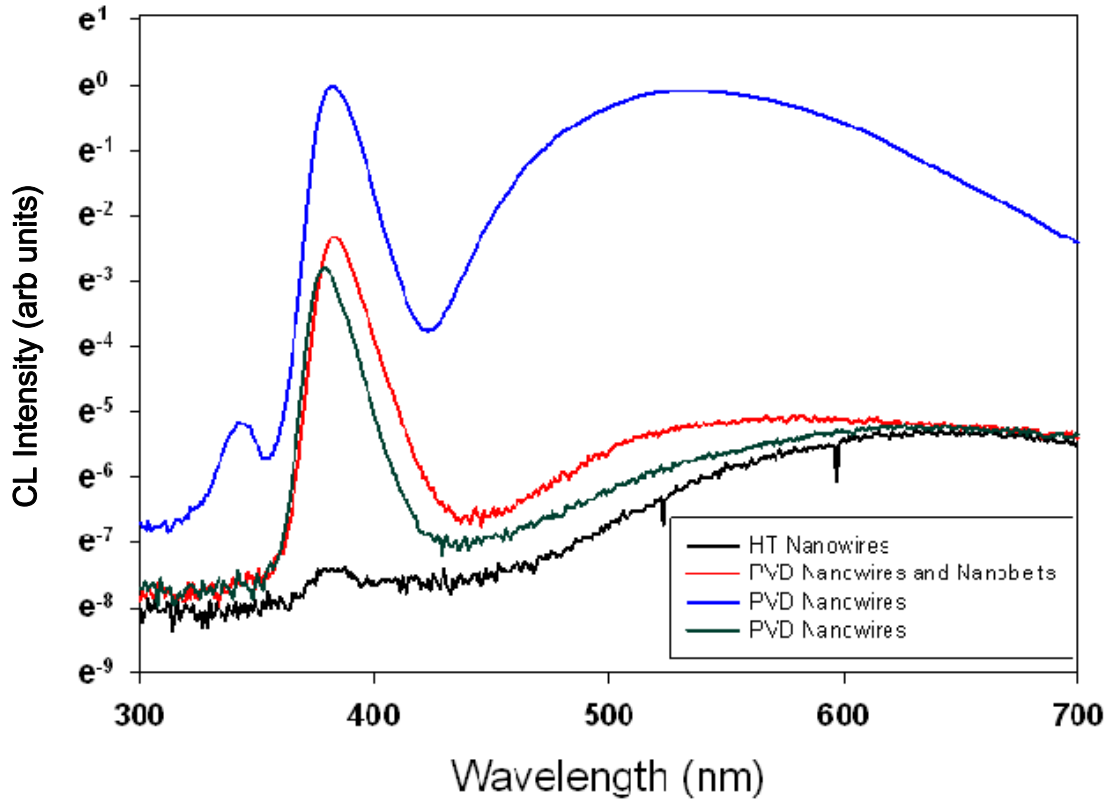


Figure 37. Semi Logarithmic Plot (Y-Axis Scale is the Natural Logarithm of Intensity) of the Normalized CL Spectra of ZnO Nanostructures at 300 K

B. NSOM IMAGING OF NANOWIRES

In the following series of images, the NSOM results are presented, followed by composite AFM/NSOM images and the slope analysis to extract L_d , the minority carrier diffusion length, as described in Chapter 3. In all cases, excitation was performed with the SEM in spot mode with an acceleration voltage of 20 keV. Figures 38 to 40 present results for n-type GaN nanowires, Figures 41 to 43 for unintentionally doped n-type GaN nanowires, and Figures 44 to 46 for p-type GaN nanowires. Results for HT ZnO nanowires are presented in Figures 47 to 49, and results for PVD ZnO nanowires are shown in Figures 50-52.

1. GaN Nanowires

a. *N-Type GaN Nanowires*

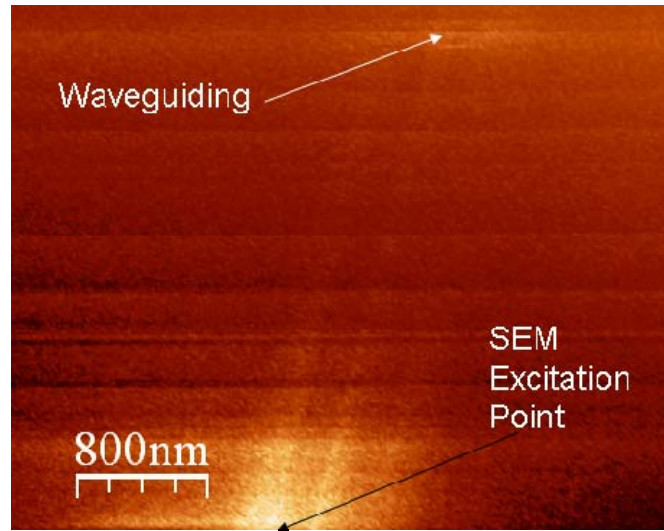


Figure 38. NSOM Image of a 0.6 μm Diameter N-Type GaN Nanowire

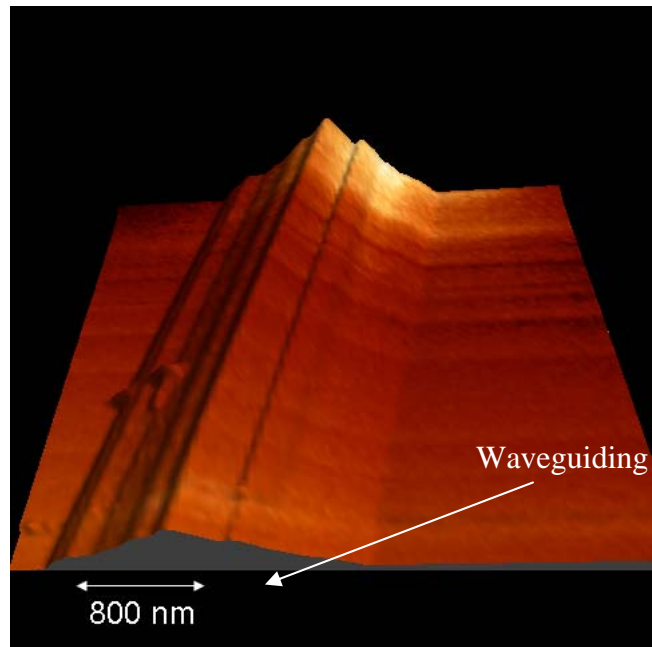


Figure 39. Combined AFM and NSOM of the GaN nanowire in Figure 38. Image has been rotated from Figure 38 for better viewing.

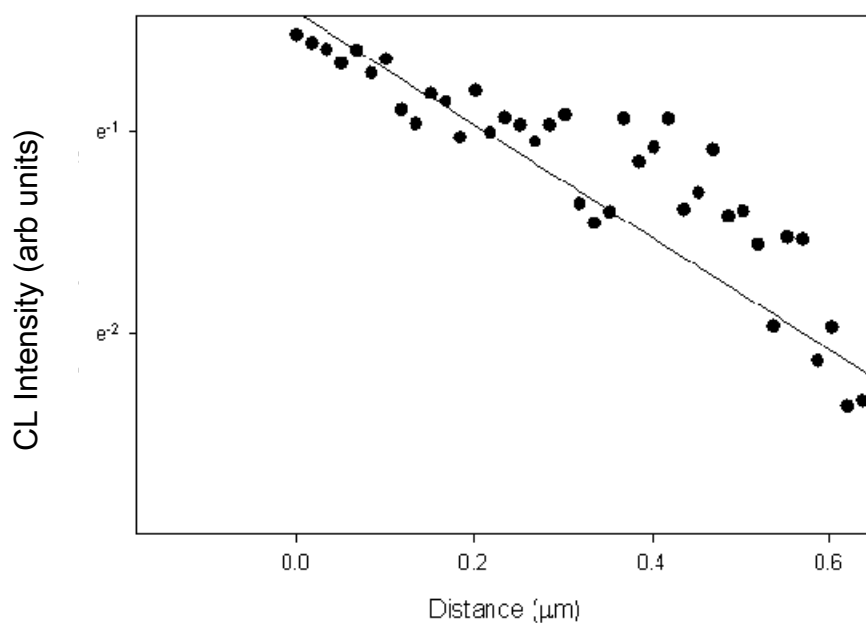


Figure 40. Semi Logarithmic Plot (Y-Axis Scale is the Natural Logarithm of Intensity) With Linear Best Fit of NSOM Intensity as a Function of Distance of a N-Type GaN Nanowire

b. Unintentionally Doped N-Type GaN Nanowires

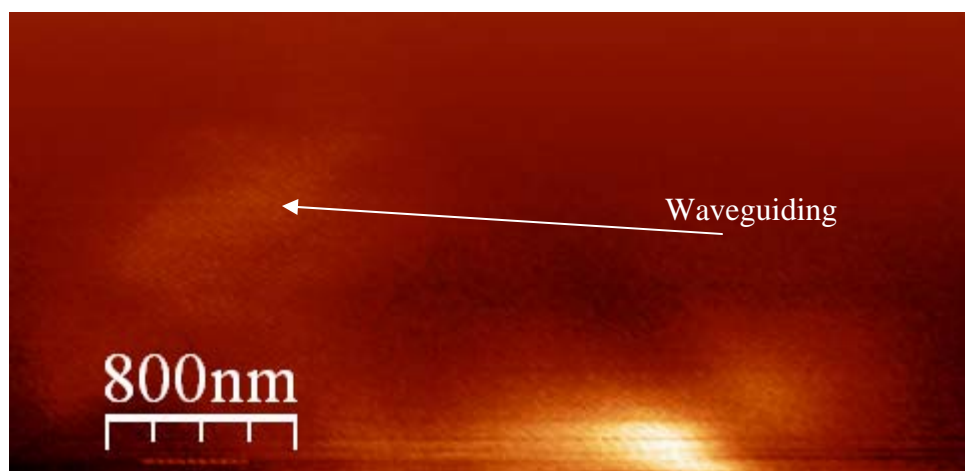


Figure 41. NSOM Image of a 0.5 μm Diameter GaN Unintentionally Doped N-Type Nanowire

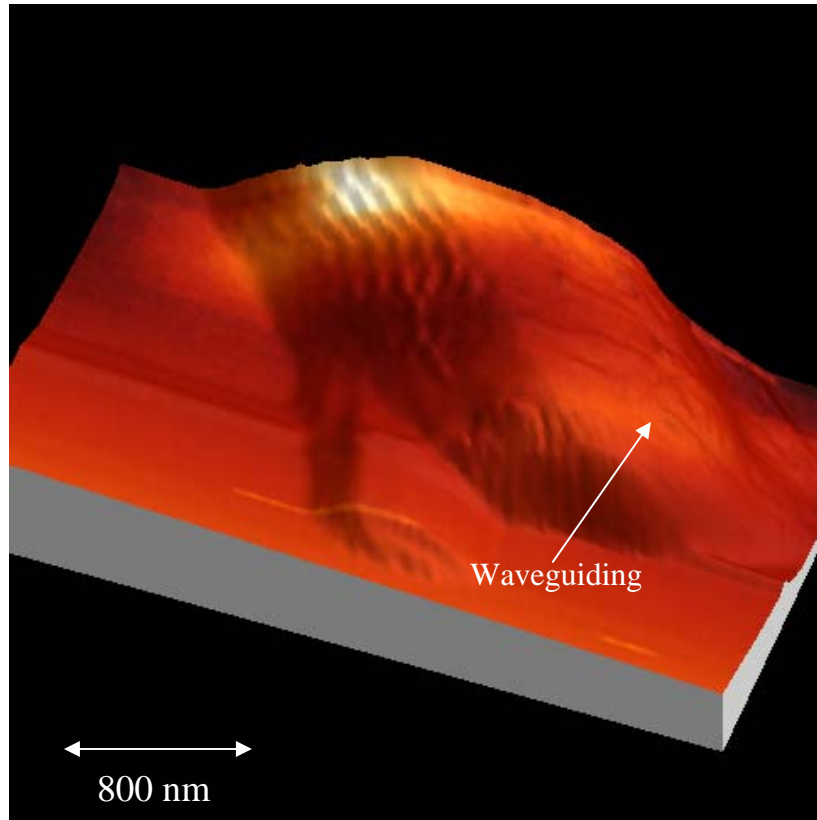


Figure 42. Combined AFM and NSOM of the GaN nanowire in Figure 41. Image has been rotated from Figure 41 for better viewing.

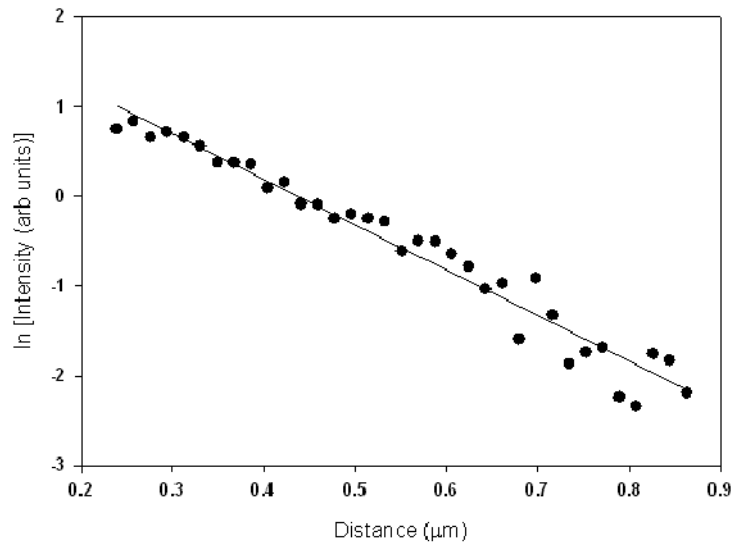


Figure 43. Semi Logarithmic Plot With Linear Best Fit of NSOM Intensity as a Function of Distance of an Unintentionally Doped N-Type GaN Nanowire

c. P-Type GaN Nanowires

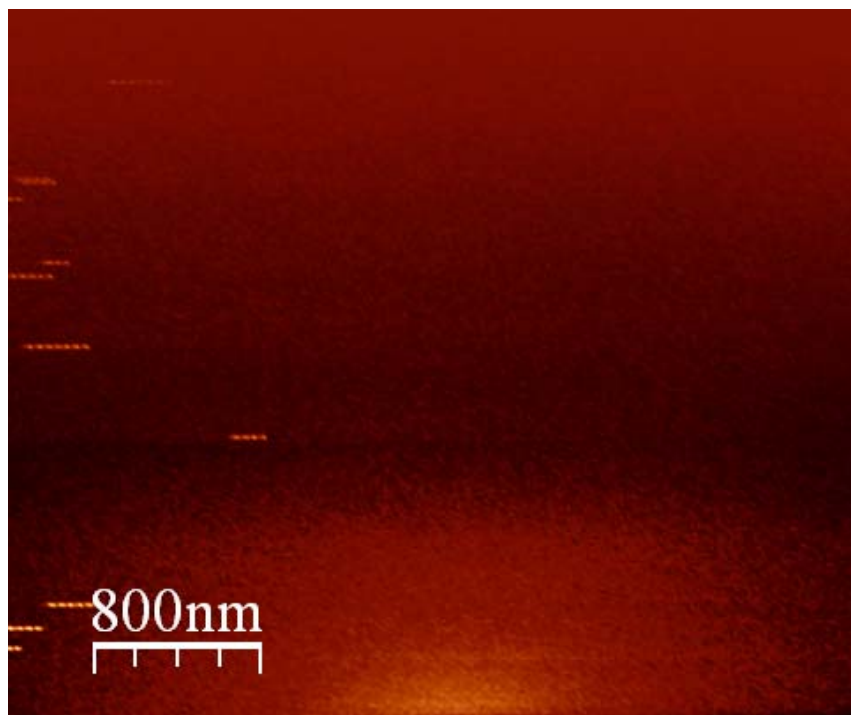


Figure 44. NSOM Image of a 0.5 μm Diameter GaN P-Type Nanowire

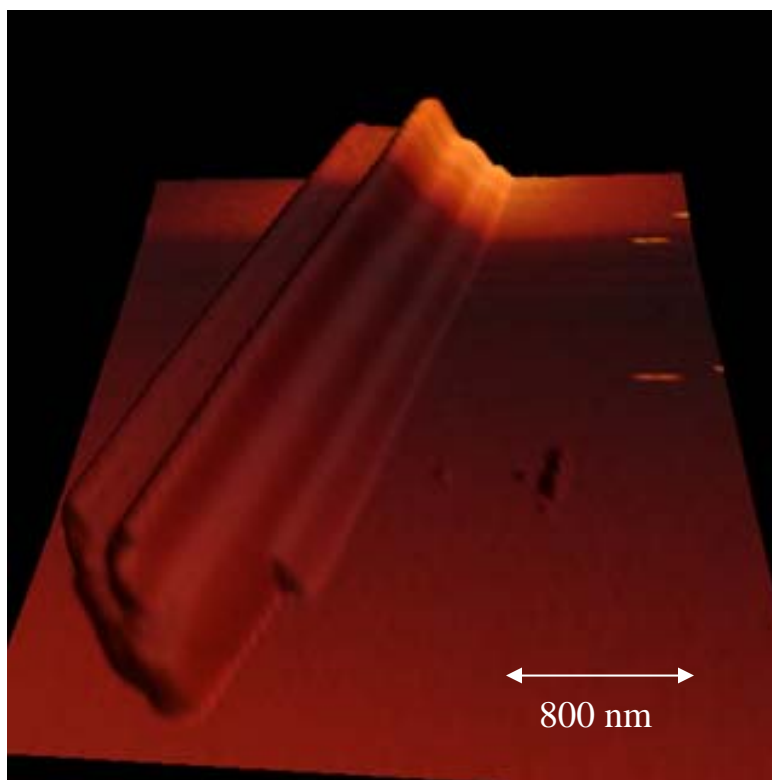


Figure 45. Combined AFM and NSOM of the GaN nanowire in Figure 44. Image has been rotated from Figure 44 for better viewing.

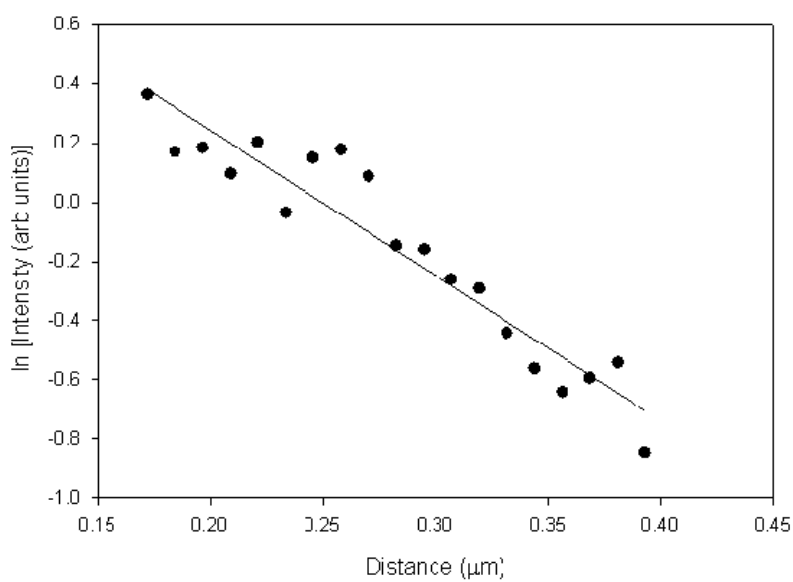


Figure 46. Semi Logarithmic Plot With Linear Best Fit of NSOM Intensity as a Function of Distance of a P-Type GaN Nanowire

2. ZnO Nanowires

a. *Hydrothermal ZnO Nanowires*

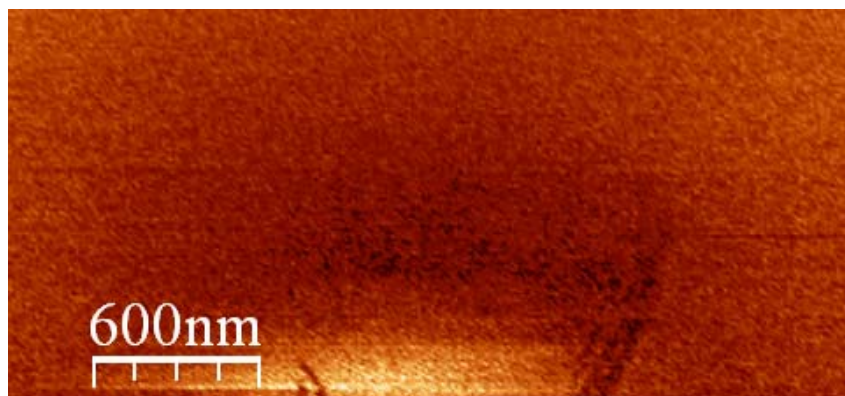


Figure 47. NSOM Image of a 0.6 μm Diameter ZnO HT Nanowire

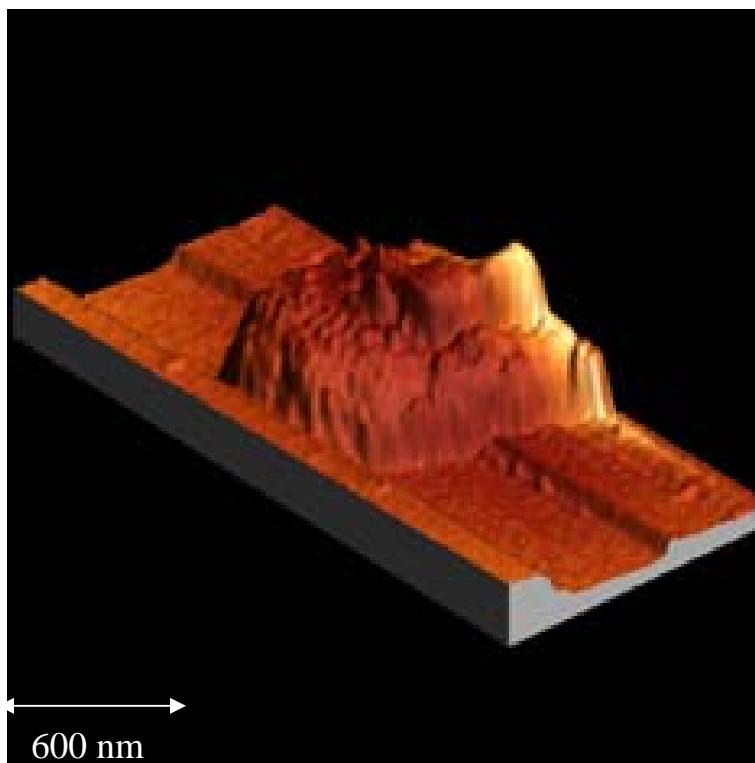


Figure 48. Combined AFM and NSOM of the HT ZnO nanowire in Figure 47. Image has been rotated from Figure 47 for better viewing.

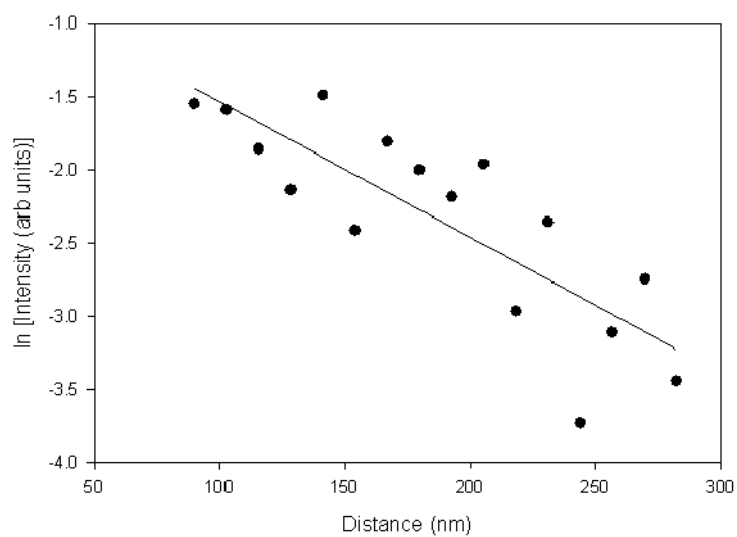


Figure 49. Semi Logarithmic Plot With Linear Best Fit of NSOM Intensity as a Function of Distance of a HT ZnO Nanowire

b. Physical Vapor Deposition ZnO Nanowires

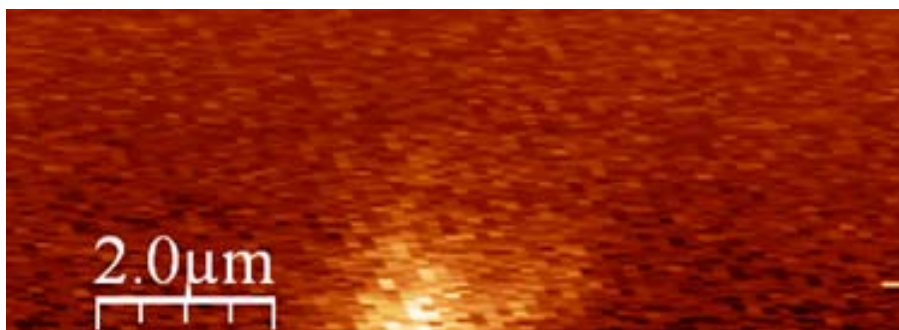


Figure 50. NSOM Image of a 0.8 μm Diameter ZnO PVD Nanowire

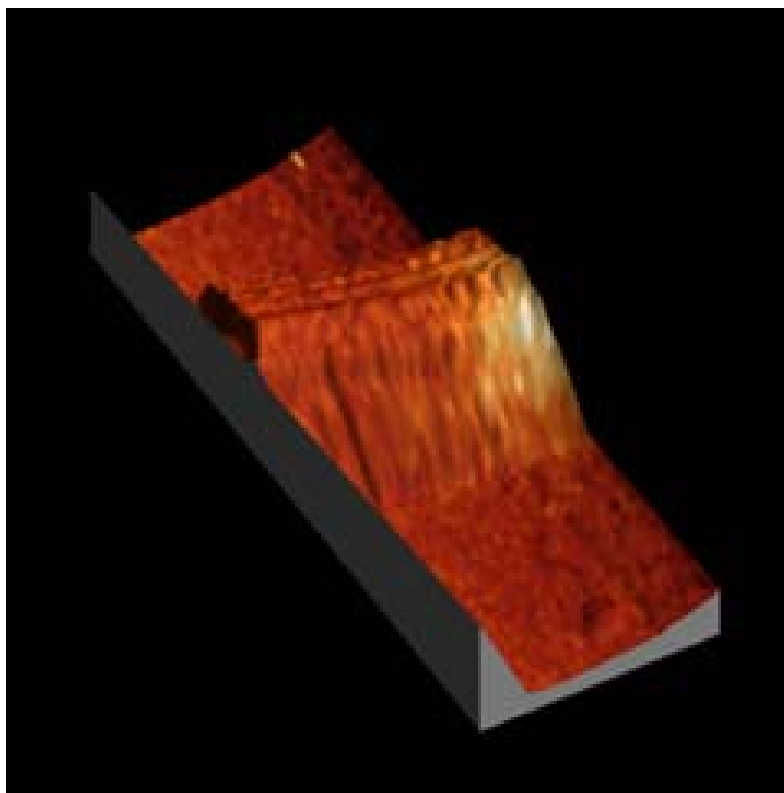


Figure 51. Combined AFM and NSOM of the nanowire in Figure 50. Image has been rotated from Figure 50 for better viewing.

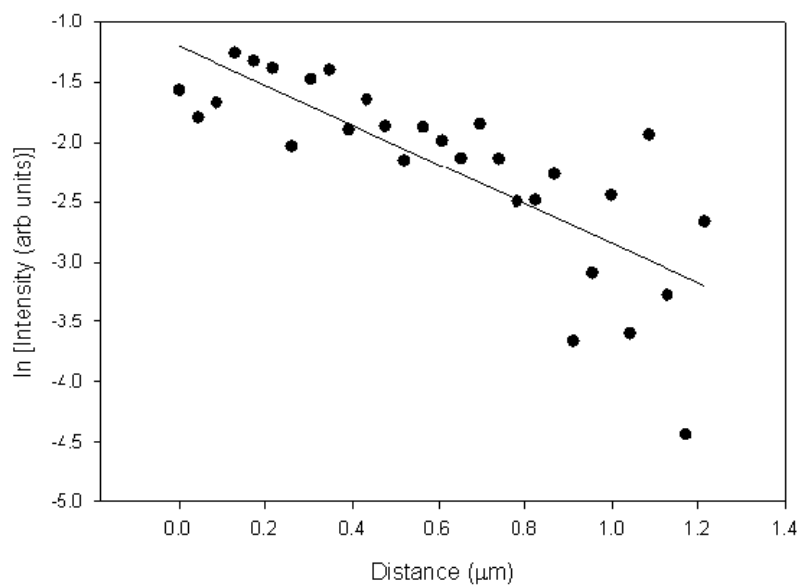


Figure 52. Semi Logarithmic Plot With Linear Best Fit of NSOM Intensity as a Function of Distance of a PVD ZnO Nanowire

C. NANOBELTS

The nanobelts examined in this thesis were long, hundreds of micrometers, and between 60 and 80 μm wide. As a result, as shown in Figures 53 to 56, diffusion in nanobelts, unlike in nanowires, is no longer constrained to one dimension. It is now a two dimensional phenomenon. As shown in Chapter III, at distances greater than five times the minority carrier diffusion length from the point of excitation, intensity is still a decreasing exponential:

$$I \sim e^{\frac{-x}{L_d}}$$

where I is intensity, x is the distance from the point of excitation, and L_d is the minority carrier diffusion length. However, the diffusion length is not known in these structures, so it is also not known how close to the point of excitation one can go and still extract valid data. As a result, the data must be fitted to the zeroth order Bessel function of the second kind described in Chapter III, which was not done in this thesis. However, data were taken from the point of excitation, and a diffusion length was extracted from them as if intensity did go like the decreasing exponential shown above. This length is the lower limit of the actual value extracted from the data fitted to the Bessel function.

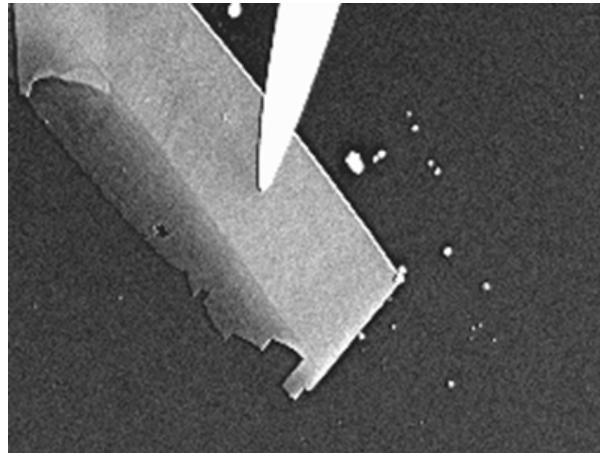


Figure 53. 80 μm Diameter ZnO PVD Nanobelt and NSOM Tip

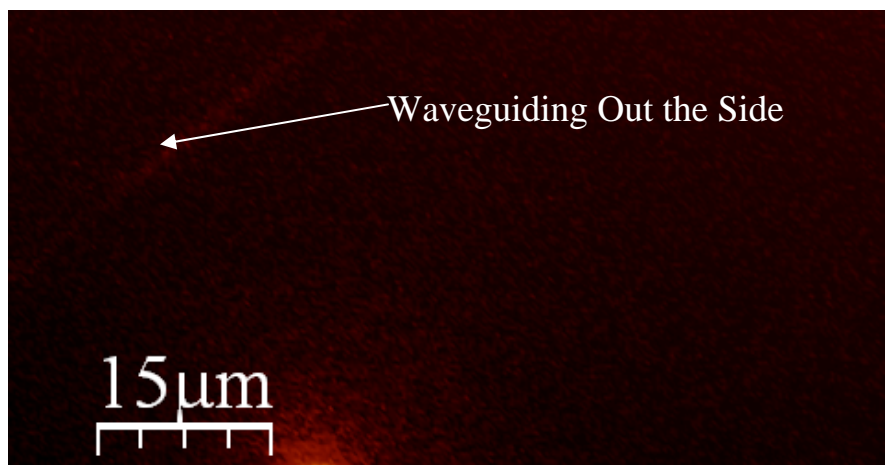


Figure 54. NSOM of a 60 μm Wide ZnO PVD Nanobelt

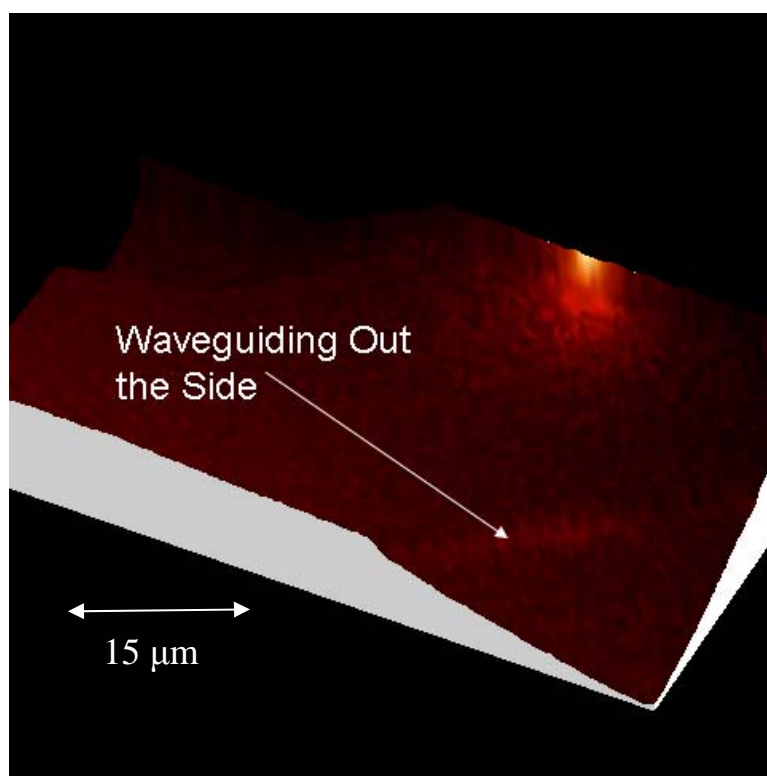


Figure 55. Combined AFM and NSOM of the Nanobelt in Figure 54

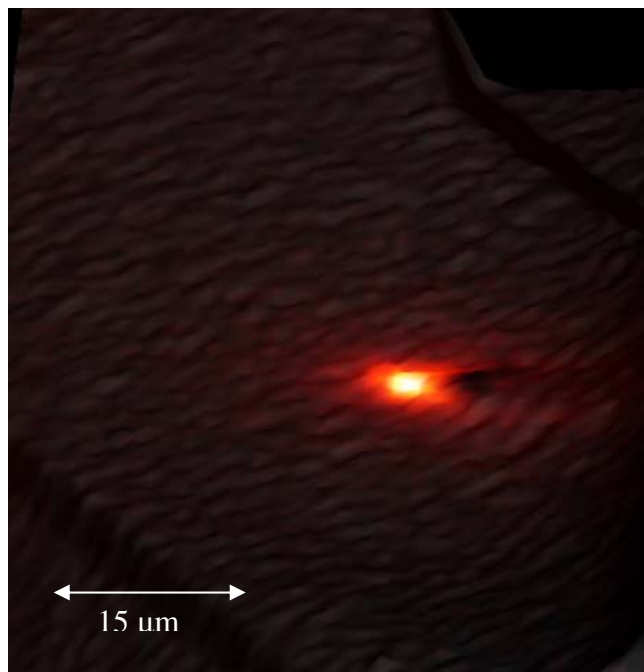


Figure 56. Combined AFM and NSOM of a 60 μm Wide ZnO PVD nanobelt. The excitation point is at the center of the scan, so diffusion is seen in all directions.

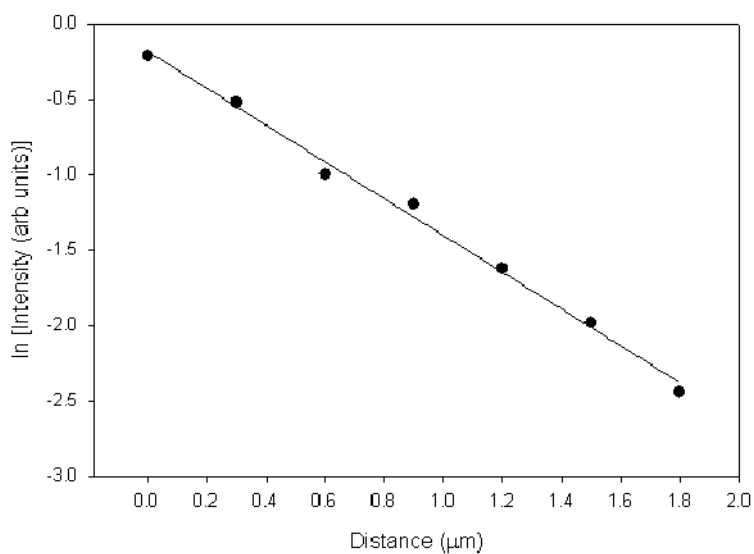


Figure 57. Semi Logarithmic Plot With Linear Best Fit of NSOM Intensity as a Function of Distance of a PVD ZnO Nanobelt. This was used to establish the lower limit of the actual minority carrier diffusion length.

D. OTHER NANOSTRUCTURES

The results shown in Figure 58 are typical of some unique structures that were studied which show the topographic features seen in Figures 32 and 33. As shown in Figure 58, light collected in these structures exhibit “banding,” a term we use when light appears as discrete bright and dim bands. Also, as shown in the bottom right corner of Figure 58, this effect is observed at two excitation currents, so it is a repeatable phenomenon and not due to one-time instabilities in the system. Further evidence of this effect is shown in Figure 59 and also in Figure 60, which is a standard, not NSOM, CL map of light bands in two nanostructures of this category. Also, as shown in the bottom left corner of Figure 58 and in Figure 61, these types of structures transmit, “leak,” light from their sides. Finally, as detailed in the top row of Figure 58 and more clearly in Figure 62, these structures often waveguide light in a way that forms a doughnut hole-type shape at the end of the structure while also always exhibiting banding.

Due to these effects, it is not possible to obtain minority carrier diffusion lengths of structures in this category using NSOM. Recall from Chapter III that the minority carrier diffusion length, L_d , is extracted from

$$I = \frac{g}{2L_d} e^{-x/L_d}$$

where I is intensity, g is the generation rate, and x is distance away from the source. Therefore, to measure L_d , light generated from minority carrier recombination must decrease exponentially due solely to recombination along the axis of the structure. As shown in Figures 58 to 62, this does not happen. Collected light appears to be along the waveguide axis, which is leakage, rather than from carrier recombination. The resultant profile contains many intensity peaks, due to banding, which create an artificially long exponential profile that results in a minority carrier diffusion length that is longer than the actual length.

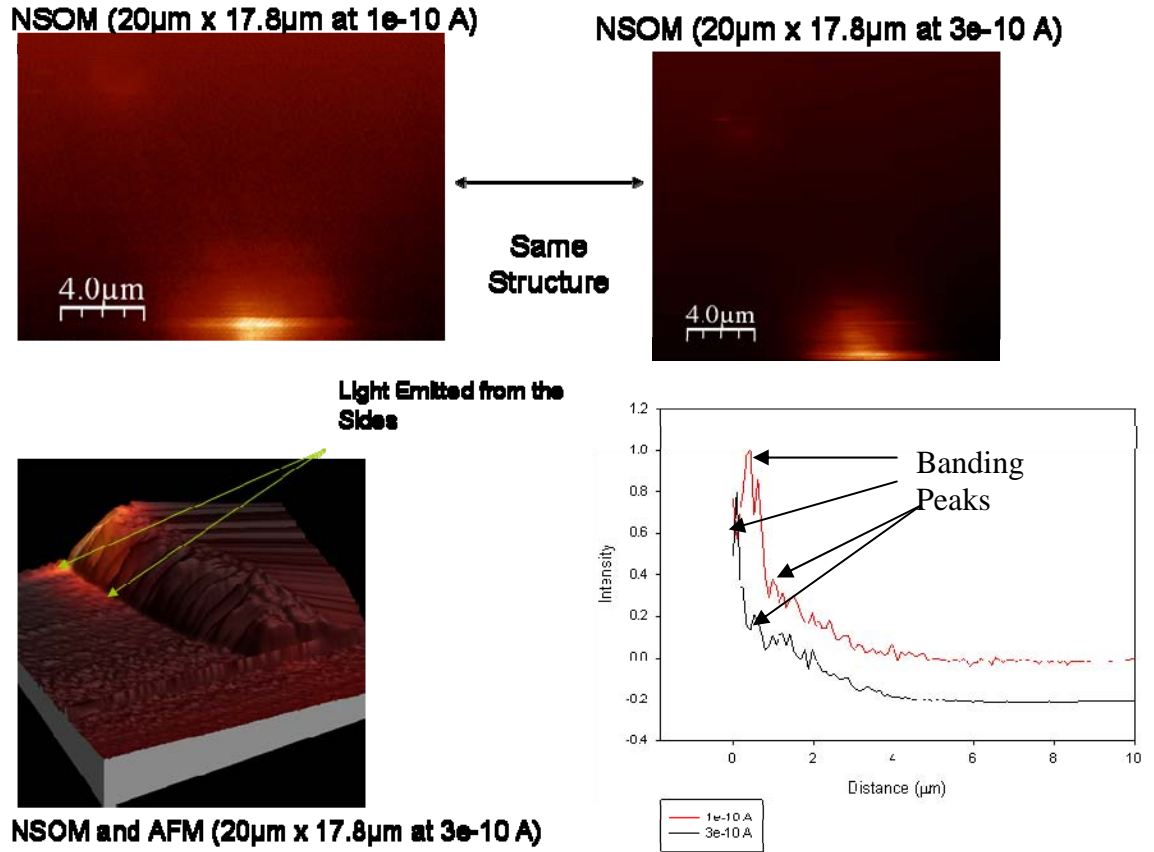


Figure 58. Example of "Leaking" and "Banding." Clockwise from top left corner: NSOM Image of a nanostructure similar to the one shown in Figure 33 with an excitation current of 10^{-10} A, NSOM of the same structure at 3×10^{-10} A, plot of NSOM intensity as a function of distance at both 10^{-10} A and 3×10^{-10} A, and the combined NSOM and AFM of the nanostructure at 3×10^{-10} A.

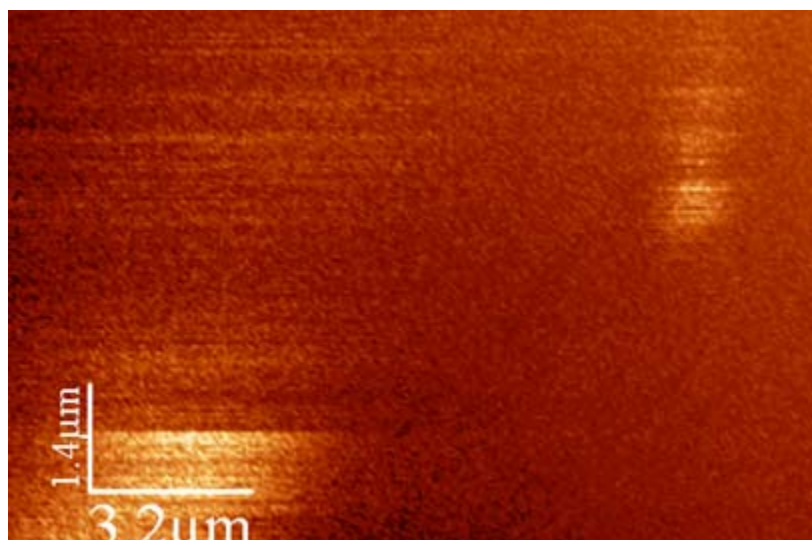


Figure 59. NSOM of a Structure that Exhibits Banding

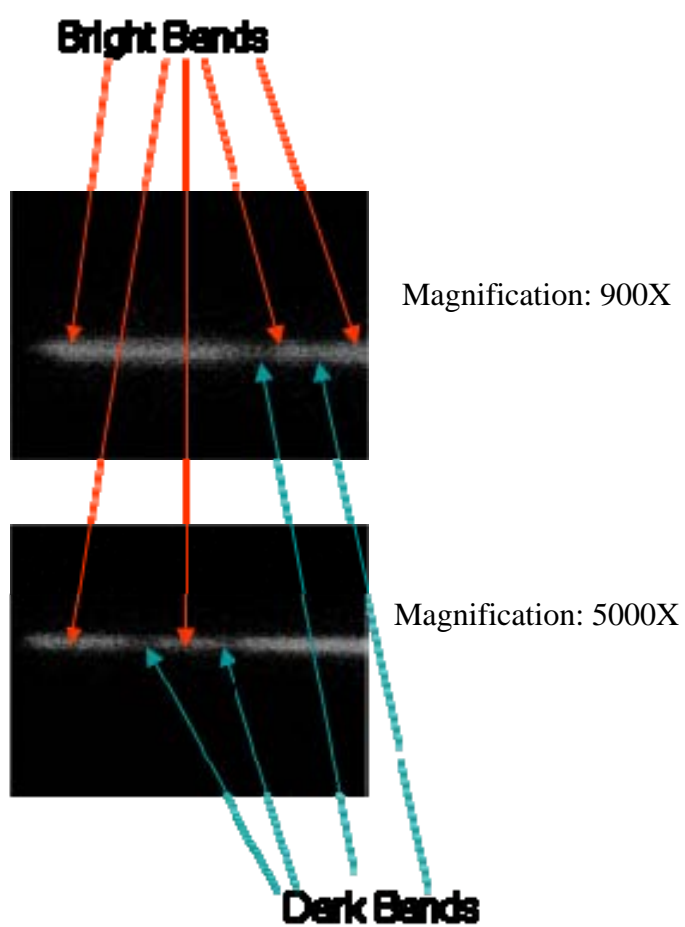


Figure 60. Standard CL Map of Light Bands in Other Nanostructure Samples

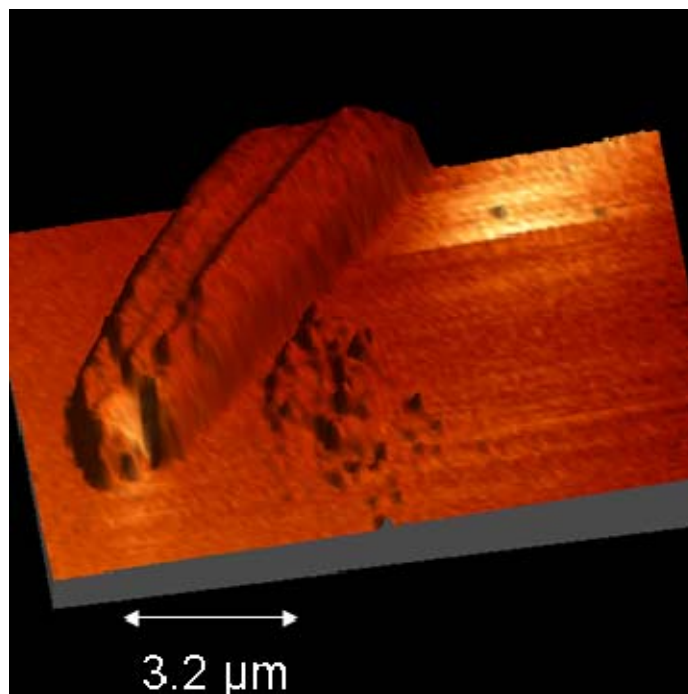


Figure 61. Combined NSOM and AFM of a nanostructure “leaking,” transmitting light out of its side.

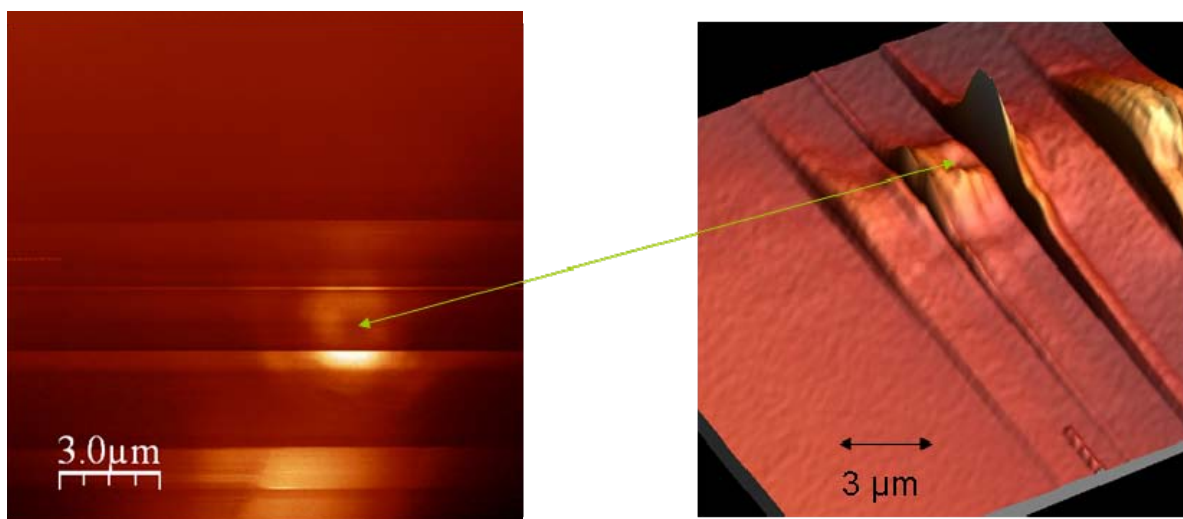


Figure 62. 2D and 3D plot of waveguided light. The 3D plot is CL intensity only, no topography data is present. Notice the distinct bands of light and the doughnut hole-like shape in the center.

E. SUMMARY OF RESULTS

Material	Structure	Type	Growth Technique	Minority Carrier Diffusion Length
GaN	Nanowire	N-Type	MBE	450 nm +/- 64 nm
GaN	Nanowire	Unintentionally Doped N-Type	MBE	180 nm +/- 14 nm
GaN	Nanowire	P-Type	MBE	200 nm
ZnO	Nanowire	Unintentionally Doped N-Type	HT	150 nm +/- 58 nm
ZnO	Nanowire	Unintentionally Doped N-Type	PVD	640 nm +/- 190 nm
ZnO	Nanobelt	Unintentionally Doped N-type	PVD	Greater Than 1.0 μm +/- 330 nm
ZnO	Other Nanostructure*	Unintentionally Doped N-Type	PVD	1.1 μm – 2 μm

Table 2. Summary of measured NSOM minority carrier diffusion lengths. *Note that, as shown in this chapter, the measured diffusion lengths of ZnO Other Nanostructures are not the actual diffusion lengths.

THIS PAGE INTENTIONALLY LEFT BLANK

VII. CONCLUSIONS AND SUGGESTIONS FOR FURTHER RESEARCH

A. CONCLUSIONS

The goals of this thesis were to measure the diffusion lengths of p-type, n-type, and unintentionally doped n-type GaN nanowires; ZnO PVD nanowires and nanobelts; and ZnO HT nanowires. While gathering these measurements, the author also observed that some nanostructures, those classified as Other Nanostructures in Chapter VI, had unique surface topographies that caused leakage of waveguided light along the structure and therefore increased the exponential decay profile associated with minority carrier recombination. Thus, it is not possible to use NSOM to measure the minority carrier diffusion length in these structures.

In his December 2009 thesis, Commander Lee Baird measured the minority carrier diffusion lengths of GaN nanowires grown by metal-organic chemical vapor deposition (MOCVD) [28]. Table 3 summarizes his results. Note that the first row of the table describes a GaN nanowire with an aluminum gallium nitride (AlGa_N) shell. This shell serves as a high bandgap barrier to reduce surface recombination. When compared to the standard (no shell) MBE GaN nanowires of Table 2, it is evident that wires grown by different processes have different minority carrier diffusion lengths with the MOCVD material showing a longer minority carrier diffusion length. This is often true in thin films as well because MBE grown material often has a larger point defect density. Further evidence of this is also found in Table 2 by comparing the short diffusion lengths of ZnO HT nanowires with the longer lengths of PVD ZnO nanowires. Also, as shown in both Tables 2 and 3, it is clear that doping also affects minority carrier diffusion lengths in nanostructures.

Nanowire	Minority Carrier Diffusion Length
GaN/AlGaN Core-Shell	1.3 μm +/- 0.20 μm
Unintentionally Doped	0.96 μm +/- 0.25 μm
P-Type	0.65 μm +/- 0.35 μm

Table 3. Summary of NSOM Minority Carrier Diffusion Lengths in MOVCD GaN Nanowires (from [28])

B. SUGGESTIONS FOR FURTHER RESEARCH

It is interesting that PVD ZnO nanobelts have diffusion lengths that are at least approximately twice the length of PVD ZnO nanowires, and 8.7 times the length of HT ZnO nanowires. It is not yet understood if this increase in diffusion length is caused by the topography (wide, flat, and thin) of the nanobelt, the specific PVD conditions needed to grow them, or a combination of the two. Thus, further research that determines nanobelt diffusion lengths as a function of size and as a function of growth conditions should be conducted.

As previously shown in Tables 2 and 3, both a nanostructure's doping type and growth process affect the minority carrier diffusion length. Again, consider the equation defining this length:

$$L_d = \sqrt{\frac{kT}{e} \mu \tau}$$

where L_d is the minority carrier diffusion length, k is Boltzmann's constant, T is temperature, μ is the charge carrier mobility, and τ is the minority carrier lifetime. Since the temperature was held constant at approximately 300 K for all experiments, it is clear that the only variable in the equation is the product of the charge mobility, which is affected by dopant type, with the minority carrier lifetime. Furthermore, since the only difference between nanowires of the same type, as in MBE n-type GaN nanowires compared to MOCVD n-type GaN nanowires, is the growth process, it is clear that different processes also have different effects on the $\mu\tau$ product. Thus, since an

understanding of how doping and growth of nanostructures interact to affect the $\mu\tau$ product will, therefore, lead to an understanding of how the minority carrier diffusion length is also affected by them, more research is needed in this area. Similar size nanostructures should be compared as a function of doping concentration and also for different growth conditions.

The optical properties of structures in the Other Nanostructures category should also be further investigated. Although it is not possible to measure the minority carrier diffusion length of these structures optically, the effects associated with surface topography, optical waveguiding, and interference are interesting and may be of some future use. For instance, it has been shown that ZnO nanowires have lased at room temperature [9], and the waveguiding effect shown in Figure 62 looks similar to the laser mode called transverse electromagnetic mode (TEM) 01*, as shown in Figure 63. Further research and experimentation should be conducted to confirm or disprove this.

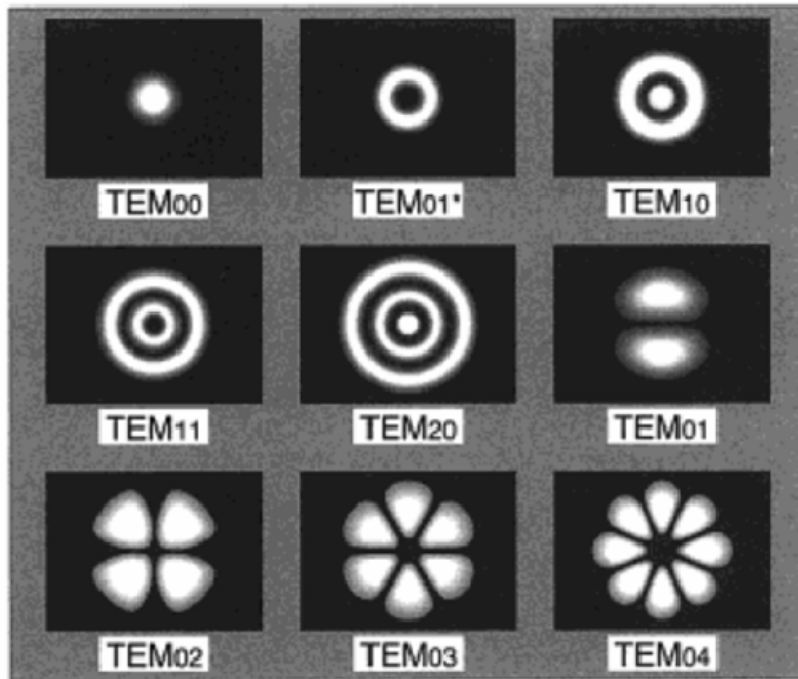


Figure 63. Transverse Electromagnetic Modes of Lasers (from [41])

The JEOL 840A has limited resolution. Due to the space requirements of the Multiview 2000 inside the SEM's chamber, the working distance, at approximately 45 mm, is large. As a result, it is sometimes difficult to resolve surface features on nanostructures. Furthermore, if separate nanostructures are near one another, it also may not be possible to resolve them as distinct structures. For instance, the author has made NSOM diffusion length measurements on what appeared to be a single nanowire only to find, when examined at a closer working distance, that wire was really several wires in close proximity. Next year, a new field emission SEM will be installed that will have nanometer resolution with the Multiview 2000 in its chamber. This will enable significant improvement in the ability to simultaneously image the nanostructures and to hold the SEM beam stable on these structures.

Finally, improved image processing tools and procedures should be developed to better display CL information collected by NSOM. In some images it is difficult to see all the CL information contained in the data, such as the waveguiding behavior in Figure 54. Tools and procedures that subtract or reduce background noise while increasing the visibility of emitted and waveguided CL will result in more accurate minority carrier diffusion length measurements, and will also yield a better understanding of how light propagates in nanostructures.

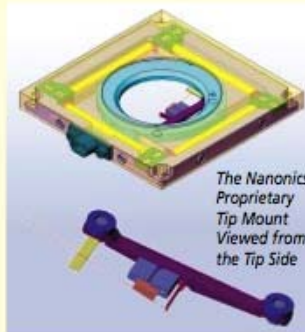
APPENDIX A. NANONICS MULTIVIEW 2000 [30]



MultiView 2000™ Tip Mount

Mechanical Design & Scanning

- Double the z scanning breakthrough achieved with one 3D Flat Scanner™ in the MultiView 1000™
- Up to 0.120 mm z scanning for ease of approach
- Samples with surface roughness from nanometers to more than one hundred microns
- Hundreds of microns deep imaging with Nanonics Deep Trench™ probes and 3D Flat Scanners™
- Complete integration with confocal microscopic 3D optical sectioning
- Laser tweezers applications
- Roughly scan samples in x-y over millimeters
- Double the conventional x-y fine motion with two scanning stages - one for tip and one for sample
- Extreme compactness and closed loop mechanical design for sample stability
- Noise floor < 1nm
- Flexible mounting geometries for all near-field optical elements

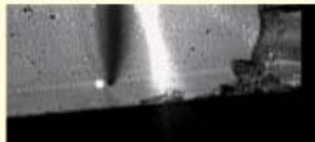


The Nanonics Proprietary Tip Mount Viewed from the Tip Side

Breakthrough in Tuning Fork Feedback

- High resonance frequencies
- High Q factors

Tuning forks were pioneered in scanned probe microscopy by K. Karrai and M. Haines US Patent Number 5,641,896. The work of Karrai and coworkers was patented for straight near-field optical/AFM elements with highly restricted geometries of tip attachment and movement. Nanonics extends this technology in two directions: First, the use of proprietary, simple, mounting techniques that maintain resonance frequencies and Q factors and resolve problems with tuning fork feedback, as noted previously [D. N. Davydov, K. B. Shelimov, T. L. Haslett and M. Moskovits, Appl. Phys. Lett. 75, 1796 (1999)]; and second, applying these mounting techniques to cantilevered near-field optical and AFM elements to provide performance at the limits attainable with scanned probe techniques.



Tip Scanning

Waveguide characterization highlights the utility of having tip and sample scanning available in a single system. The distribution of light emanating from the edge of a waveguide can be best imaged by collection mode tip scanning. In this case, the light is injected into the bottom of the waveguide through an inverted microscope objective or an input fiber. The geometry of the light source and waveguide must be kept stationary throughout the measurement, and sample scanning would disturb the injection of light into the waveguide. Thus, tip scanning collection mode is preferred in this case and in similar experiments.

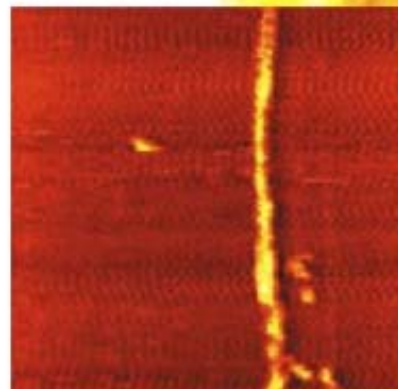
Using an on-line optical microscope allows simultaneous viewing of the edge of a hanging planar waveguide and the NSOM/AFM cantilevered tip as it is positioned to inject light into the waveguide (top left image). The waveguide is hung on the bottom plate of the sample scanner while the tip is mounted on the top plate, the tip scanner (bottom left image).

Sample Scanning

Many experiments are performed best using sample scanning. For example, one might want to monitor, with ultra high resolution, index of refraction variations along the edge of the waveguide together with AFM topography. Light emitted from the NSOM tip and reflected off the edge of a waveguide is collected by a high numerical aperture (NA) microscope objective. In such an optical measurement, tip scanning relative to a high NA objective destroys the axial symmetry of the optical system and can result in image artifacts. Tip artifacts have to be avoided to reach the ultimate in these super resolution reflection measurements of index of refraction that can monitor alterations of $<1/1000$.

The MultiView 2000™ Series also includes the LT Low Temperature systems that Nanonics provides.

The MultiView 2000™ Series builds on the standards of modularity, flexibility, and full system performance that were established by the MultiView 1000™. Present owners of a Nanonics MultiView 1000™ can upgrade to the Nanonics MultiView 2000™ Series.



Soft Sample Imaging of a Fibril of Associated Protein Molecules

The MultiView 2000™ L (Large Samples)

- Integrate Alpha Step, AFM, and optical information
- Tip scanning
- Large sample stage
- Customer specified stage sizes and accuracy

The MultiView 2000™ C (Confocal Imaging)

- Tip scanning
- Add to any existing optical microscope, including UV confocal microscopes
- On-line viewing with lens and tip for imaging and calibration
- Resolve optical image and AFM registration in semiconductor applications
- Ultra-high resolution thin film measurements



Accessories for liquid and electrochemical cells, odd-shaped sample mounts, and environmental control systems

With the MultiView 2000™ Series, Nanonics Imaging has reaffirmed its position as the complete supplier in this unique interface between scanned probe and optical microscopy. At Nanonics Imaging, both the optical microscope and the scanned probe imaging system are given equal importance. No other manufacturer of scanned probe or optical microscopes can provide for such effective solutions in both these growing areas of imaging. The result is the ultimate degree of integration in imaging methodologies.

MultiView 2000™ Technical Specifications

Modes of Operation

Near-field Optical Microscopy	Transmission, reflection, collection, fluorescence
Atomic Force Microscopy	Tuning fork
Feedback Mechanism	Tuning fork (resonance frequency approximately 32 kHz)
Confocal Microscopy	Transmission, reflection, fluorescence

Sample or Tip Scanning

Scanner	Two piezoelectric flat scanners (both 7 mm thick) Sample scanning or tip scanning Scan Range: 120 μ Z-range, 70 μ XY-range (30 and 10 μ on request) Maximum Load: 75 g
Resolution	< 5 nm in XY, < 1 nm in Z
Sample Positioning	Inertial piezo motion (6 mm range, accuracy 1 μ)
Maximum Sample Size	16 mm diameter, custom mounts for larger samples available upon request

Probes

NSOM Probes	Cantilevered or straight, pulled optical fiber probes
AFM Probes	Cantilevered, pulled glass probes or any commercially available AFM probes
Specialized Probes	Cantilevered probes for electrical or thermal measurements
Custom Probes	Available upon request

Optics

Viewing/Detection Optics	Free optical access to the sample from top and bottom for optical observation of the sample (all conventional far-field modes of operation are available) and for detection of the NSOM signals with any optical microscope (upright, inverted, dual) or other optics
Detectors	Photomultiplier Tube (PMT), Avalanche Photodiode Detector (APD), InGaAs Detector for IR, CCD
Lasers	A large variety of laser systems can be used (UV, VIS, IR)
Video System	Optional CCD camera

Optical Resolution

Confocal Microscopy	Diffraction limited
Near-field Microscopy	From 50 nm upwards, depending on the aperture size of the NSOM probe used
Controller	Nanonics/Topaz (Digital Instruments, RHK, Park Scientific and Topometrix controllers can also be used to control the MultiView 2000™ microscope)
Software	Quartz software for Nanonics/Topaz controller (Win 95/98 and NT) Real time image display, image acquisition (up to 8 channels) and analysis, 3D rendering

Options

Environmental Chamber	Control the measurement environment (humidity, gas composition, vacuum)
Electrical Measurements	Options for resistance, thermal measurements
Nanochemical/Gas Delivery	Deliver a chemical via the nanopipette/AFM tip to the sample surface



NANONICS IMAGING Ltd.

Manhat Technology Park, Malcha
Jerusalem 91487, Israel
Tel: +972-2-6789573
Fax: +972-2-6480827
US Toll-free: 1-866-220-6828
www.nanonics.co.il
email: info@nanonics.co.il

THIS PAGE INTENTIONALLY LEFT BLANK


APPENDIX B. SPCM-AQR-14 PHOTON DETECTOR [31]

DATASHEET

Optoelectronics

Single Photon Counting Module

SPCM-AQR Series



Description

The SPCM-AQR is a self-contained module which detects single photons of light over the wavelength range from 400 nm to 1060 nm, a range and sensitivity which often outperforms photomultiplier tubes.

The SPCM-AQR-IX utilizes a unique silicon avalanche photodiode which has a circular active area whose peak photon detection efficiency over a 180 μm diameter exceeds 65% at 650 nm. The photodiode is both thermoelectrically cooled and temperature controlled, ensuring stabilized performance despite changes in the ambient temperature. The SPCM-AQR module can count to speeds exceeding 10 million counts per second (Mc/s) for the SPCM-AQR-1X. There is a "dead time" of 50 ns between pulses.

The SPCM-AQR requires a +5 Volt power supply. A TTL pulse of 2.5 Volts (minimum) high in a 50 Ω load and 35 ns wide, is output at the rear BNC

connector as each photon is detected. To avoid a degradation of the module linearity and stability, the case temperature should be kept between 5° C and 40° C during operation.

Saturation

The count decreases at higher incoming light levels. The count at which the output rate starts to decrease is called the saturation point. As an extreme example, if the module is exposed to intense light the count rate will fall to zero. Consequently, in certain applications, some tests should be performed by the operator to ensure that a low count rate is not caused by detector saturation.


Precautions should be taken to avoid any excessive light level that will damage the SPCM module.

Applications

- LIDAR
- Photon Correlation Spectroscopy
- Astronomical Observation
- Optical Range Finding
- Adaptive Optics
- Ultra Sensitive Fluorescence
- Particle Sizing

Features

- Peak Photon Detection Efficiency @ 650nm: 65% Typical
- Active Area: SPCM-AQR-IX: 175 μm
- User Friendly
- Gated Input
- Single +5V Supply


PerkinElmer
CORPORATION

optoelectronics.perkinelmer.com

Single Photon Counting Module - SPCM-AQR Series

Fiber Connection Option

Ordering Guide 1

The SPCM-AQR-WX-FC has an "FC" fiber-optic receptacle pre-aligned to the optical detector. Optical fibers with an FC connector on one end are available separately, see Ordering Guide 2. Due to the wavelength dependence of the graded index coupling lens, the operating wavelength range must be specified; see Ordering Guide 2. The photon detection efficiency of connectorized modules is about 95% of that quoted for standard modules.

Fiber Shielding

When used with optical fibers, both the fiber itself and the connector shrouds must be completely opaque; if not stray light will increase the count rate. The SPCM-QCX pigtailed conform to this requirement; see Ordering Guide 2.

Gating Function

A gating function is provided with each module. It is useful when you are looking for a signal that occurs only in a small time frame window. Also, in some applications the background light flux is higher than the signal. In this case, the gating option could be used to improve the S/N ratio by opening a window only when the light signal is present. *The output of the module is disabled when a TTL low level is applied to the module gate input.*

Light Emission During Photon Detection

One peculiarity of silicon avalanche photodiodes is that as an incoming photon is detected a small amount of light is emitted from the avalanche region. The light emitted has a broad spectral distribution. In most cases this is not a problem. However, it can cause some confusion if another detector is monitoring light, or if the optical system is such that light emitted from the SPCM-AQR is reflected back on itself. If these photons return 35 ns after the initial event, they will be detected.

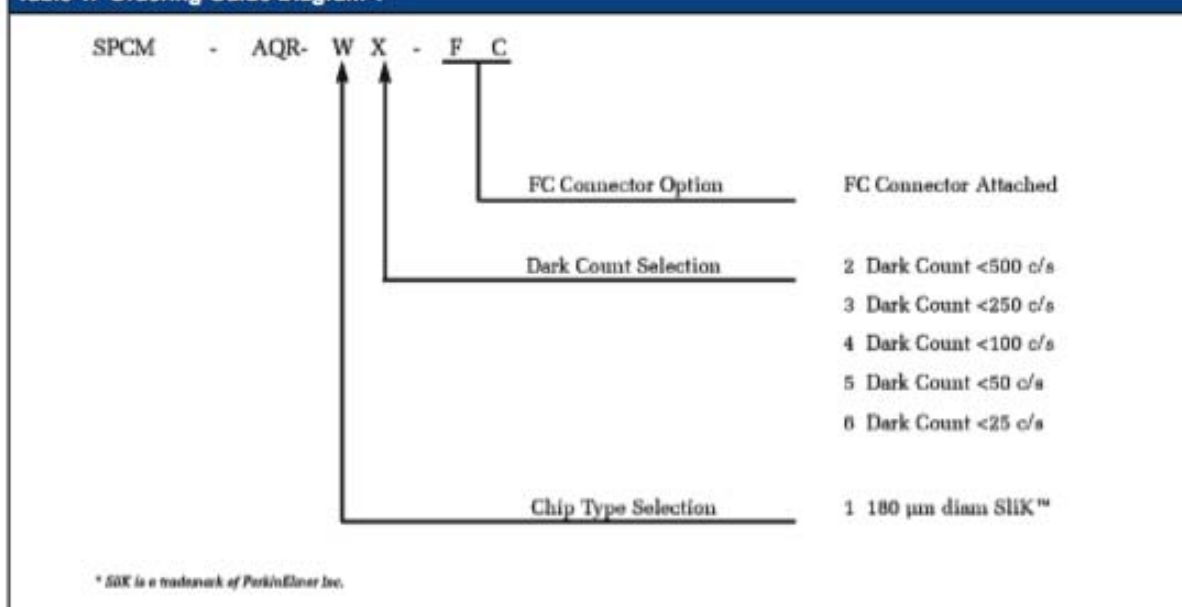
Safety

The SPCM-AQR contains a high voltage power supply. All internal settings are pre-set; *there are no user adjustments*. Units which appear defective or have suffered mechanical damage should not be used because of possible electrical shorting of the high voltage power supply.

Warranty

A standard twelve month warranty following shipment applies. Any warranty is null and void if the module case has been opened.

Table 1. Ordering Guide Diagram 1



Single Photon Counting Module - SPCM-AQR Series

Table 2. Ordering Guide Diagram 2

Part Number	Fiber Type	Connector Type	Diameter			Numerical Aperature
			Core	Cladding	Outer	
SPCM-QC4	Multimode	FC / Bare	62.5 μm	125 μm	2.5 mm	0.27
SPCM-QC6	Multimode	FC / Bare	100 μm	140 μm	2.5 mm	0.29
SPCM-QC8	As SPCM-QC6 but 905 SMA on free end, 100 microns core fiber					
SPCM-QC9	As SPCM-QC6 but FC connector on free end, 100 microns core fiber					

Table 3. Specifications SPCM-AQR-WX @ 22° C, all models, unless otherwise indicated

Parameter	Minimum	Typical	Maximum	Units
Supply current		0.5	1.9	Amps
Supply voltage: (1)	4.75	5.0	5.25	V
PerkinElmer power cable total resistance		0.2		Ω
Case operating temperature (1.3)	5		40	°C
Active area (diameter) @ minimum Pd	170	175		μm
Photon detection efficiency (Pd) @				
400 nm	2	5		%
650 nm	50	65		%
830 nm	35	45		%
1060 nm	1	2		%

Single Photon Counting Module - SPCM-AQR Series

Table 4. Specifications SPCM-AQR-WX @ 22° C, all models, unless otherwise indicated				
Parameter	Minimum	Typical	Maximum	Units
Pd variation at constant case temperature (2h @ 25° C)		± 1	± 3	%
Pd variation 5° C to 40° C case temperature		± 4	± 10	%
Dark Count (4,5,6) =				
SPCM-AQR-12		—	500	Counts/Second
SPCM-AQR-13		—	250	Counts/Second
SPCM-AQR-14		—	100	Counts/Second
SPCM-AQR-15		—	50	Counts/Second
SPCM-AQR-16		—	25	Counts/Second
Average dark count variation at constant case temperature (6 hrs @ 25° C) for (4,5,6);				
SPCM-AQR-12 & 13			± 10	%
SPCM-AQR-14 & 15 & 16			± 1	σ
Average dark count variation at 5° C to 40° C case temperature for (4,5,6);				
SPCM-AQR-12 & 13			± 20	%
SPCM-AQR-14 & 15 & 16			± 2	σ
Single Photon Timing Resolution		Contact factory for availability		
Dead Time (Count rates below 5 Mc/s)		50	60	ns

Single Photon Counting Module - SPCM-AQR Series

Table 5. Specifications SPCM-AQR-WX @ 22° C, all models, unless otherwise indicated - continued

Parameter	Minimum	Typical	Maximum	Units
Output count rate before saturation	10	15		Mc/s
Linearity correction factor: (7)				
@ 200 kc/s		1.01		
@ 1 Mc/s		1.08	1.15	
@ 5 Mc/s		1.40	1.67	
Afterpulsing probability		0.5		%
Settling time following power up (1% stability) @ 1 meg counts/sec and 25° C		15	30	s
Threshold setting required on counter for digital output pulse (terminate in 50 Ohms)	0.75	1.0	2.0	V
Output pulse width		35		ns
Gating turn on/off: (50Ω output)				
Disable = TTL Low		2	4	ns
Enable = TTL High		45	55	ns
Gating Threshold Voltage: (@ V _{supply} = 5V)				
Low level (sink current >90mA)		0	0.4	V
High level (sink current >30mA)		3.5	5.25	V

Table 6. Absolute Maximum Ratings

Supply Voltage (1)	5.5V
Mean Count Rate	5 Mc/s (Above this point, dead time will increase due to diode self-heating)
Peak Light Intensity	10 ⁴ photons per pulse and pulse width less than 1 ns.
Case Temperature (3)	50° C Storage, 40° C operating

Single Photon Counting Module - SPCM-AQR Series

1. Connection to incorrect voltage or reverse voltage may destroy the module. The warranty is invalid where such damage occurs.
2. These modules are not qualified for shock or vibration other than normal instrumentation environments.
3. The module dissipates a mean power of 2.5W, and a maximum power of 6.5W at high count rate and 40° C. Adequate heat sinking must be provided by clamping the module to a suitable heat sink via the holes in the module base. For the specification performance, the module case temperature must not exceed 40° C.
4. Bi-stability of the dark count: On a small percentage of delivered modules, bi-stability of the dark count has been observed. Research indicates that this bi-stability is probably due to transitions at a single impurity site between a low energy and a high energy state. The phenomenon is seen as an abrupt change in the dark count rate, e.g. 350 to 390 c/s and the dark count switches between the two states at a rate which depends on the detector temperature. Multilevel switching has also been observed, where more than one impurity site is switching.
5. Long-term bi-stability is related to fundamental semiconductor physics and is outside PerkinElmer's control. Warranty claims will not be entertained against bi-stability alone. Warranty claims will only be considered if the high level of the dark count exceeds the maximum level in the specification.
6. In the dark, the module generates random counts that follow a Poisson distribution. In a Poissonian process the standard deviation is equal to the square root of the average counts. In this specification the "dark count variation" refers to the stability of the average count of the module.
7. The actual photon rate could be calculated using the following equation, as indicated below:

Table 7. Equation

$$ACTUALCOUNTRATE_{Photons} = \frac{(OUTPUT_{ModuleCountRate} \times CORRECTIONFACTOR @ the Module CountRate) - DARK COUNT Module}{PHOTON DETECTION EFFICIENCY Module}$$

The theoretical value, at low count rate, of the Correction Factor follows this equation:

$$Correction Factor = \frac{1}{1 - (t_d \times C_R)}$$

Where: t_d = Module Dead Time
 C_R = Output Count Rate

The deviation from an ideal linear system is another way of looking at the saturation effect. The following equations show how to calculate this departure from the linearity:

$$LINEARITY = \frac{OUTPUT_{ModuleCountRate}}{(PHOTONS Actual Count Rate \times PHOTON DETECTION EFFICIENCY Module) + DARK COUNT Module} - 1$$

$$= \frac{1}{Correction Factor} - 1$$

Single Photon Counting Module - SPCM-AQR Series

Figure 1. Block Diagram of Module

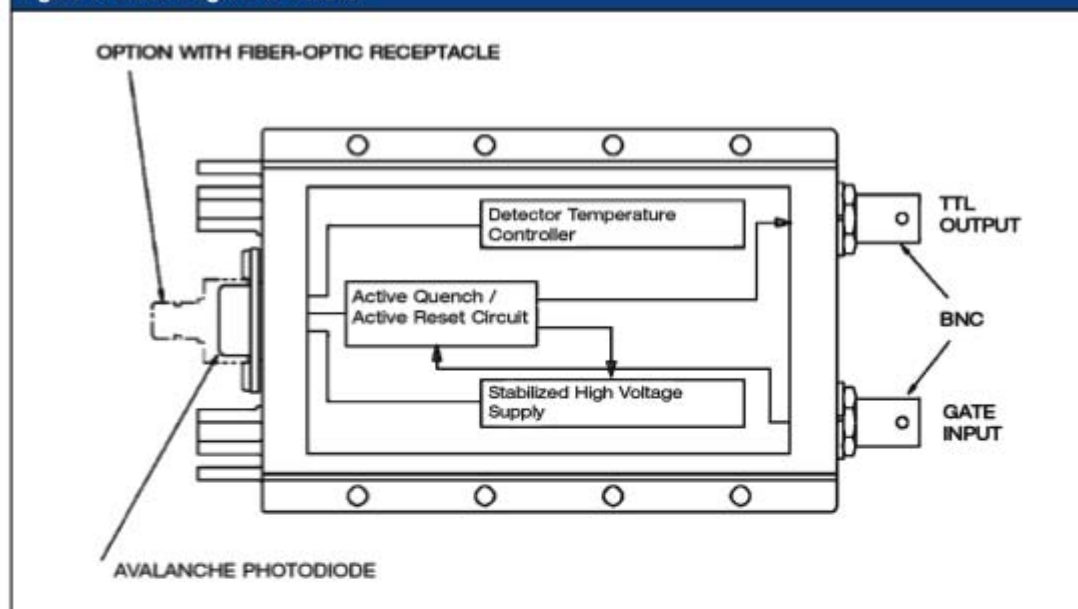
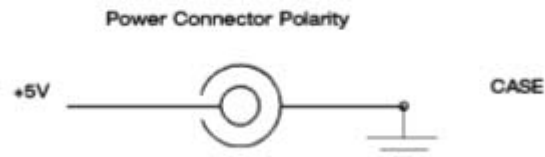


Figure 2. Electrical Connections

The digital output pulse, $\geq 2.5\text{V}$, should be terminated with a $50\ \Omega$ load to avoid distortion and ringing. A 1.0V triggering level is recommended. The gate input impedance is $50\ \Omega$ and is connected through an internal pull-up resistor to the $+5\text{V}$ supply.



CONNECTOR: BARREL TYPE
 I.D. = 2.5 mm (0.10")
 O.D. = 5.5 mm (0.22")
 LENGTH = 12.0 mm (0.47")

CABLE: CENTER WHITE STRIPED LEAD
 WIRE GAUGE = 22 AWG
 LENGTH = 1.8 M (72")

Figure 3. Dectector Scan

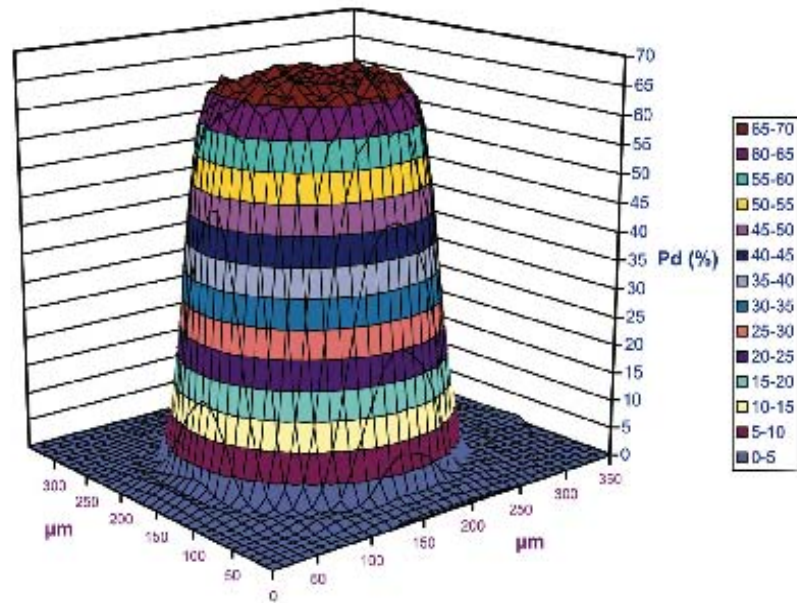


Figure 4. Photon Detection Efficiency (pd) vs. Wavelength

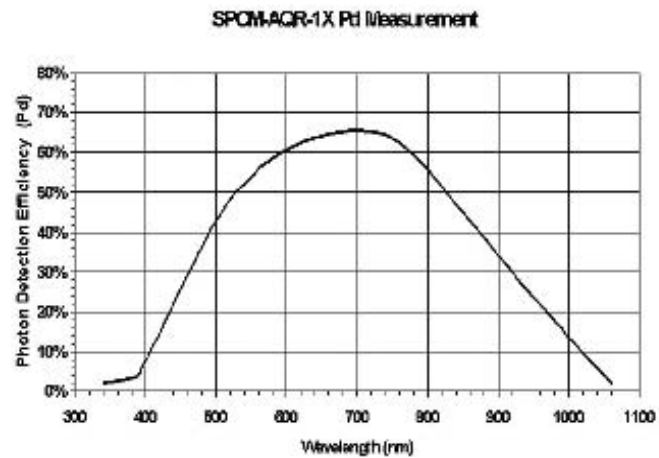


Figure 5. Typical Afterpulse Probability

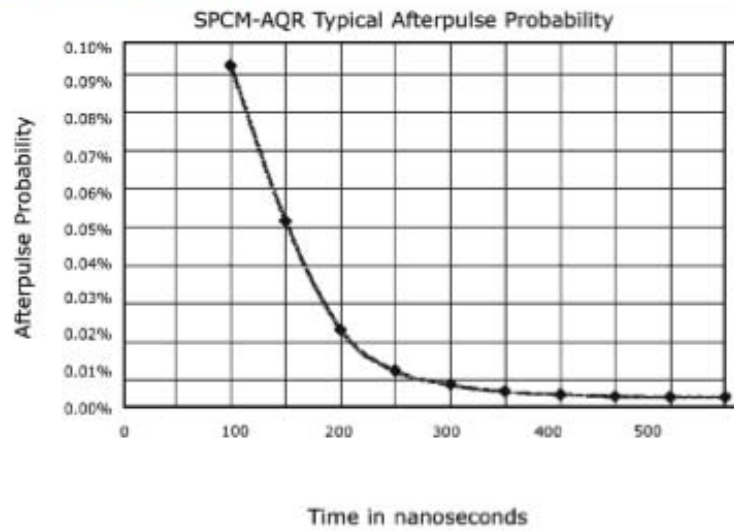
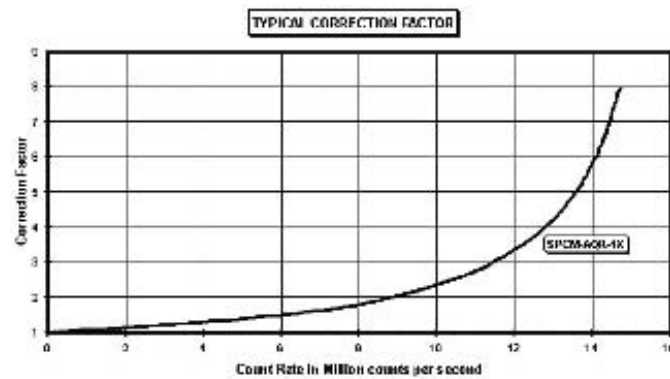


Figure 6. Typical Correction Factor



Single Photon Counting Module - SPCM-AQR Series

Figure 7. Dimensional Outline

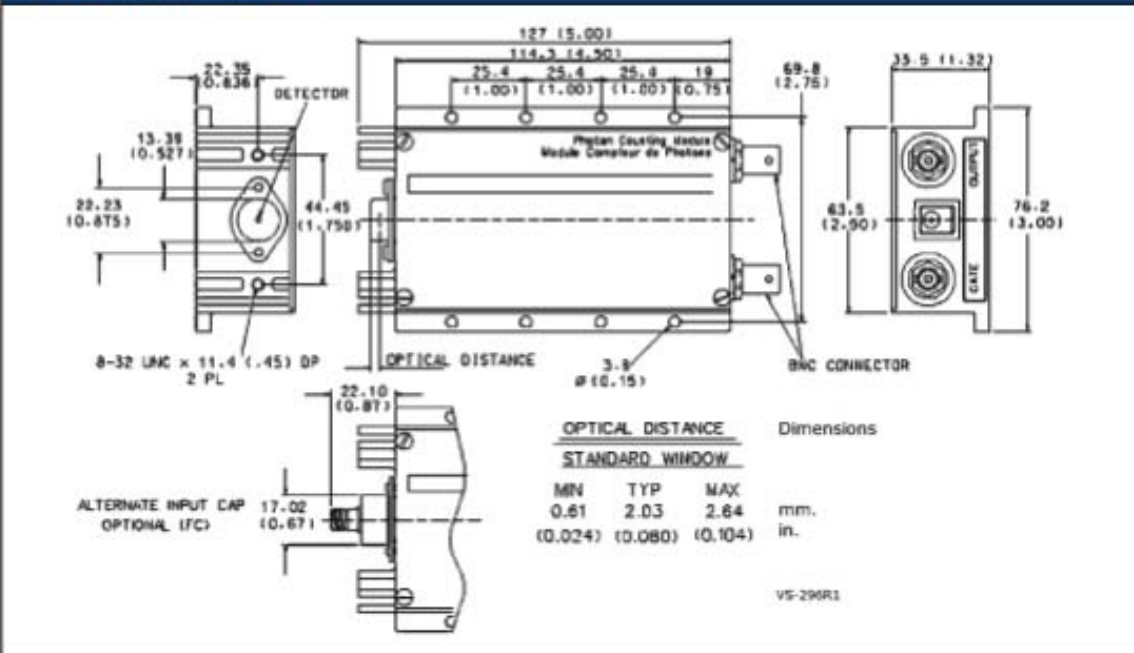
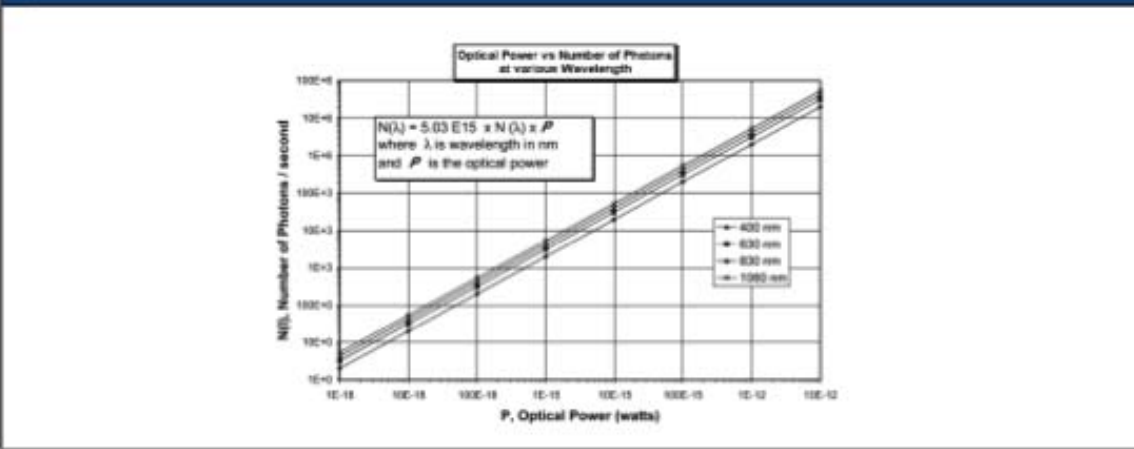
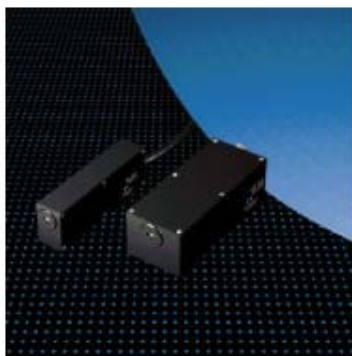


Figure 8. Optical Power vs. Number of Photons



APPENDIX C. MP-983 PHOTON DETECTOR [32]



MP 900 - 1/3" Photoncounting Module

Ultra High Sensitivity Gateable
Photon Counting Module

Description

The Photon Counting Head MP 900 series is designed for applications in all fields of single photon detection, e.g. chemoluminescence, bioluminescence, fluorescence, in-vitro assay, environmental measurements or pure research. It is an easy to use module, containing the Channel Photomultiplier, a high voltage power supply, a discrimination amplifier and a pulse shaper for fast output pulses. An installed active quenching system avoids over-illumination to the detector.

It is also possible to apply an external gate function for time correlated photon counting. Strong variations in light levels are possible due to the high dynamic range of the installed CPM. The exceptional low noise and high sensitivity facilitates detection of extremely low light levels.

Features

- high dynamic range
- no cooling required
- very high stability in noise level
- active quenching circuit for high light protection
- gateable CPM input
- Optical fiber read-out possible
- 5 volts operating voltage
- monitor voltage output

Technical Specification

Model *) (also order no.)	Detector type	Installed CPM type	Photocathode diameter	Photocathode material	Window material	Spectral response / nm	Quantum efficiency	Dark counts per second (cps)
MP 942	CPM-Channel Photomultiplier	C942	min. 5 mm	Bialkali	Quartz	165-650	20% typical (ext. red MA: 10% typ.)	10
MP 943		C943		Bialkali	UV glass	185-650		10
MP 952		C952		Low noise Multialk.	Quartz	165-750		40
MP 953		C953		Low noise Multialk.	UV glass	185-750		40
MP 962		C962		Multialk.	Quartz	165-850		100
MP 963		C963		Multialk.	UV glass	185-850		100
MP 972		C972		Extended red Multialk.	Quartz	165-900		500
MP 973		C973		Extended red Multialk.	UV glass	185-900		500
MP 982		C982		Low noise Bialkali	Quartz	165-650		3
MP 983		C983		Low noise Bialkali	UV glass	185-650		3

*) Additional models on request

Operating conditions

Supply voltage	5 V dc
Input current at max. count rate	< 280 mA
Settling time	< 1s (time to stabilize HV after supply voltage applied)
Over-illumination protection:	active quenching control (internal)
Linear count rate:	5 MHz
Output pulse:	TTL, positive
Active Quenching Control	TTL-Pulse, active high, RESET: internal via timer, typ. 2,5 s, external via 5 V-pulse
Output pulse width	15 ns, (opt. 130 ns)
GATE voltage V_{gate}	5 V: h to l set time V_{on} to V_{ohent} * 100 V : = 150 μ s 5 V: l to h set time V_{on} to V_{ohent} * 100 V : = 150 μ s
Maximum ratings	
Input voltage	+5.5 V
Operating temperature	5 to 40 °C
Storage temperature	-20 to 50 °C
Weight	~ 350 g

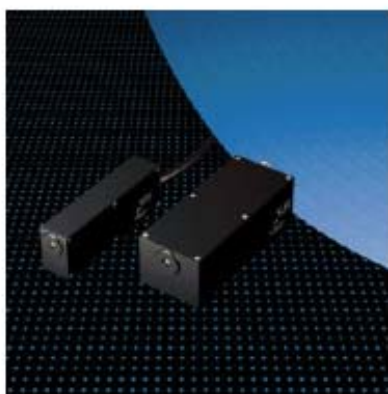
EU Perkin Elmer Optoelectronics GmbH
65020 Wiesbaden, Germany
PO-Box 3007
Tel. ++49 (0) 611-492 - 0
Fax. ++49 (0) 611-492 - 159

USA Perkin Elmer Optoelectronics
2175 Mission College Blvd.
Santa Clara, CA 95054
Tel. ++1 (408) 565-0830
Tel. ++1 (408) 565-0703

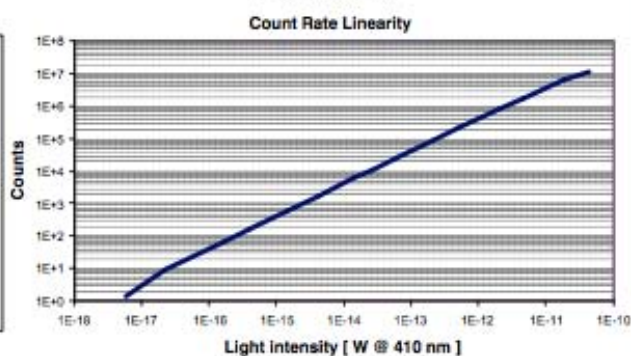
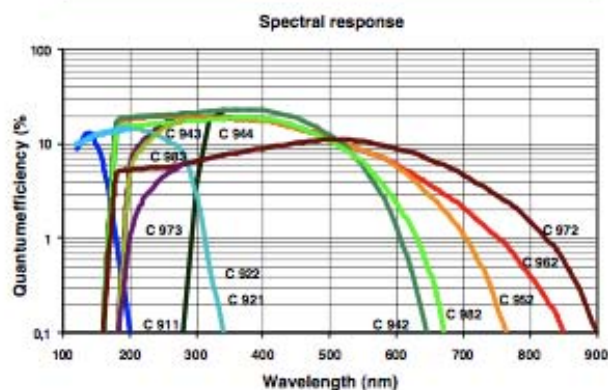
ASIA Perkin Elmer Optoelectronics
47 Ayer Rajah Crescent, #06-12
Singapore 139947
Tel. (65) 775 2022
Tel. (65) 775 1008

www.perkinelmer.com / opto

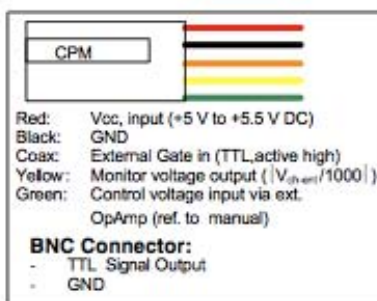
PerkinElmer®
optoelectronics.



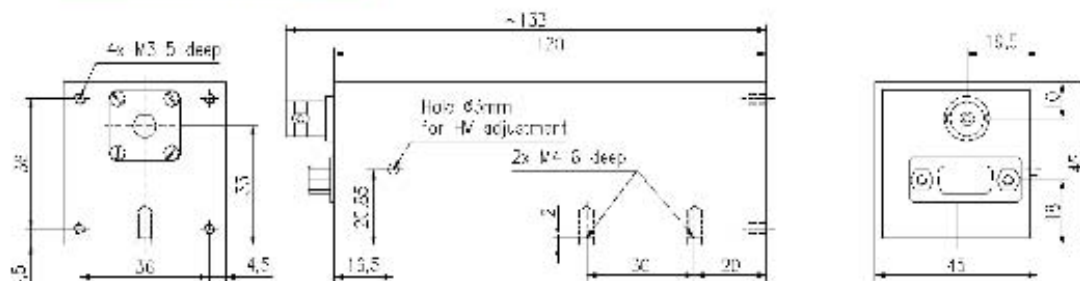
MP 900 – Performance Characteristics



Connections



Dimensions (mm)



- CAUTION: HIGH VOLTAGE WARNING**
 This product operates at high voltage. Extreme care must be taken to ensure operator safety and to avoid damage to other instruments. Avoid direct contact with the entrance window of the built in CPM when high voltage is applied. Avoid placing conductive material close to the cathode.
 Ensure that no light levels are applied, generating higher anode currents than specified.
 All given values are nominal/typical @ 20 °C ambient temperature; specification subject to change without notice

© PKJ 09/2001

LIST OF REFERENCES

- [1] M. Weik. (1961). *The ENIAC Story*. [Online]. Available: <http://ftp.arl.mil/~mike/comphist/eniac-story.htm>
- [2] D. Haviland. (2002, Dec. 19). *The Transistor in a Century of Electronics*. [Online]. Available: <http://nobelprize.org/educational/physics/transistor/history/>
- [3] R. G. Dreslinski *et al.*, “Near Threshold Computing: Reclaiming Moore’s Law Through Energy Efficient Integrated Circuits,” *Proceedings of the IEEE*, vol.98, no. 2, pp. 253–266, Feb. 2010.
- [4] R. Chaue *et al.*, “Benchmarking Nanotechnology for High Performance and Low-Power Logic Transistor Operations,” *IEEE Transactions on Nanotechnology*, vol. 4, no. 2, pp. 153–158, Mar. 2005.
- [5] Advanced Micro Devices, Inc. (2009). *ATI Radeon HD 5870 Graphics*. [Online]. Available: <http://www.amd.com/us/products/desktop/graphics/ati-radeon-hd-5000/hd-5870/Pages/ati-radeon-hd-5870-overview.aspx#2>
- [6] N. Gupta *et al.*, “Prospects of Nanostructure-Based Solar Cells for Manufacturing Future Generations of Photovoltaic Modules,” *International Journal of Photoenergy*, vol. 2009, Article ID 154059, 13 pages, 2009. doi: 10.1155/2009/154059
- [7] M. L. Kuo *et al.*, “Realization of Near-Perfect Antireflection Coating for Silicon Solar Energy Utilization,” *Optics Letters*, vol. 33, no. 21, pp. 2527–2529, Nov. 2008.
- [8] A. S. Arico *et al.*, “Nanostructured Materials for Advanced Energy Conversion and Storage Devices,” *Nature Materials*, vol. 4, pp. 366–377, May 2005. doi: 10.1038/nmat1368
- [9] B. S. Zou *et al.*, “Lasing Mechanism of ZnO Nanowires/Nanobelts at Room Temperature,” *J. Phys. Chem. B*, vol. 110, no. 26, pp. 12865–12873, Jun. 2006.
- [10] M. Zimmler *et al.*, “Optically Pumped Nanowire Lasers: Invited Review,” *Semiconductor Science and Technology*, vol. 25, no. 2, 12 pages, Jan. 2010.
- [11] Massachusetts Institute of Technology. (2010). *About the Institute for Soldier Nanotechnologies*. [Online]. Available: <http://web.mit.edu/ISN/aboutisn/index.html>

- [12] F. Allhoff, "Nanotechnology and the Military," in *Nanoethics*. Hoboken, New Jersey: John Wiley and Sons, 2007, pp. 267–276.
- [13] A. K. Viswanath *et al.*, "Photoluminescence Studies of Excitonic Transitions in GaN Epitaxial Layers," *Journal of Applied Physics*, vol. 84, no. 7, pp. 3848–3859, Oct. 1998.
- [14] L. H. Robins *et al.*, "Optical and Structural Study of GaN Nanowires Grown by Catalyst-Free Molecular Beam Epitaxy. I. Near-Band-Edge Luminescence and Strain Effects," *Journal of Applied Physics*, vol. 101, no. 11, 8 pages, DOI:10.1063/1.2736264.
- [15] X. Bai *et al.*, "Measuring the Work Function at a Nanobelt Tip and at a Nanoparticle Surface," *Nanoletters*, vol. 3, no. 8, pp. 1147–1150, Jun. 2003.
- [16] J. Elias *et al.*, "Hollow Urchin-Like ZnO Thin Films by Electrochemical Deposition," *Advanced Materias*, vol. 22, no. 14, pp. 1607–1612, Apr. 2010.
- [17] G. Rieke, "Photodiodes and Other Junction-Based Detectors," in *Detection of Light*. New York, New York: Cambridge University Press, 2003, pp. 78-115.
- [18] Rensselaer Polytechnic Institute (2003). *Semiconductors Defined – 35*. [Online]. http://www.rpi.edu/dept/phys/ScIT/InformationProcessing/semicond/sc_content/semi_35.html#
- [19] C.P. Ong, "Measurement of Minority Carrier Diffusion Length in Gallium Nitride Nanowires using Electron Beam Induced Current (EBIC)," M.S. Thesis, Physics Department, Naval Postgraduate School, Monterey, CA, 2009.
- [20] B. Yacobi and D. Holt, "Introduction," in *Cathodoluminescence Microscopy of Inorganic Solids*. New York, New York: Plenum Publishing Corporation, 1990, p. 1.
- [21] D. Luber *et al.*, "Imaging Transport for the Determination of Minority Carrier Diffusion Length," *Applied Physics Letters*, vol. 88, no. 16, 3 pages, Apr. 2006.
- [22] F. Pedrotti, L. S. Pedrotti, L. M. Pedrotti, "Fraunhofer Diffraction," in *Introduction Optics*. Upper Saddle River, New Jersey: Pearson, 2007, p. 267.
- [23] E. Betzig and J. Trautman, "Near-Field Optics: Microscopy, Spectroscopy, and Surface Modification Beyond the Diffraction Limit," *Science*, vol. 257, Issue 5067, pp. 189-195, Jul. 1992.
- [24] M. Davison. (2010). *Resolution*. [Online] Available: <http://www.microscopyu.com/articles/formulas/formulasresolution.html>

- [25] Nanonics Imaging Ltd. (2010). *A Brief History and Simple Description on NSOM/SNOM Technology*. [Online] Available: http://www.nanonics.co.il/index.php?page_id=149
- [26] F. Giessibl and C. Quate. "Exploring the Nanoworld with Atomic Force Microscopy," *Physics Today*, vol. 59, no. 12, pp. 44–50, Jan. 2006.
- [27] S. D. Winchell, "Transport Imaging for the Study of Nanowires and Related Nanostructures," M.S. Thesis, Physics Department, Naval Postgraduate School, Monterey, CA, 2006.
- [28] L. G. Baird., "Near Field Imaging of Gallium Nitride Nanowires for Characterization of Minority Carrier Diffusion," M.S. Thesis, Physics Department, Naval Postgraduate School, Monterey, CA, 2009.
- [29] C. H. Low, "Near Field Scanning Optical Microscopy (NSOM) of Nano Devices," M.S. Thesis, Physics Department, Naval Postgraduate School, Monterey, CA, 2008.
- [30] Nanonics LTD, "The MultiView 2000," MultiView 2000 datasheet.
- [31] Perkin Elmer Optoelectronics, "Single Photon Counting Module SPCM-AQR Series," SPCM-AQR-14 datasheet, Jul. 2004.
- [32] Perkin Elmer Optoelectronics, "MP 900 -1/3 Photoncounting Module," Mp-983 datasheet, Sep. 2001.
- [33] P. Capper, "Bulk Crystal Growth of Wide-Bandgap II-VI Materials," in *Bulk Crystal Growth of Electronic, Optical and Optoelectronic Materials*. San Francisco, CA: John Wiley and Sons, 2005, pp. 277–283.
- [34] Z. Wang, "ZnO Nanowire and Nanobelt Platform for Nanotechnology," *Materials Science and Engineering*, vol. 64, issues 3-4, pp. 33–71, Apr. 2009.
- [35] University of Minnesota School of Physics and Astronomy (2006). *Epitaxial Growth of Graphene*. [Online]. Available: http://mxp.physics.umn.edu/s07/Projects/S07_Graphene/intro.htm
- [36] R. Farrow, "The Technology and Design of Molecular Beam Epitaxy Systems," in *Molecular Beam Epitaxy: Applications to Key Materials*. Park Ridge, NJ: Noyes Publications, 1995, pp. 1–5.

- [37] K. Bertness *et al.*, “Mechanism for Spontaneous Growth of GaN Nanowires with Molecular Beam Epitaxy,” *Journal of Crystal Growth*, vol. 310, pp. 3154–3158, Mar. 2008.
- [38] X. Wang. (2010). *Physical Vapor Deposition Technique for Growing Nanostructures*. [Online]. Available:
<http://www.nanoscience.gatech.edu/zwang/research/pvd.html>
- [39] Z. Pane *et al.*, “Nanobelts of Semiconducting Oxides,” *Science*, vol. 291, no. 5510, pp. 1947-1949, Mar. 2001.
- [40] I. Shalish *et al.*, “Sized-Dependent Surface Luminescence in ZnO Nanowires,” *Physical Review B*, vol. 69, no. 24, 4 pages, Mar. 2004.
- [41] W. Silvast, “Laser Fundamentals,” in *Laser Cavity Modes*. New York: Cambridge University Press, 2004, p. 394.

INITIAL DISTRIBUTION LIST

1. Defense Technical Information Center
Ft. Belvoir, Virginia
2. Dudley Knox Library
Naval Postgraduate School
Monterey, California
3. Professor Andres Larraza
Chairman, Department of Physics
Naval Postgraduate School
Monterey, California
4. Professor Nancy M. Haegel
Naval Postgraduate School
Monterey, California
5. R. Adam Cole
Naval Postgraduate School
Monterey, California